Julius-Maximilians-
UNIVERSITÄT
WÜRZBURG

New Materials for Lithium-Ion Batteries

Dissertation zur Erlangung des naturwissenschaftlichen
Doktorgrades der Julius-Maximilians-Universität Würzburg

Hanne Flåten Andersen

Fraunhofer-Institut für Silicatforschung ISC

Fraunhofer
ISC

Würzburg, 2013

Eingereicht bei der Fakultät für Chemie und Pharmazie am 07. August 2013

Gutachter der schriftlichen Arbeit

1. Gutachter: Prof. Dr. Gerhard Sextl
2. Gutachter: Prof. Dr. Sanjay Mathur

Prüfer des öffentlichen Promotionskolloquiums

1. Prüfer: Prof. Dr. Gerhard Sextl
2. Prüfer: Prof. Dr. Sanjay Mathur
3. Prüfer: Prof. Dr. Peer Löbmann

Datum des öffentlichen Promotionskolloquiums
31. Juli 2014

Doktorurkunde ausgehändigt am

Abstract

Over the last decades, lithium-ion batteries have grown more important and substituted other energy storage systems. Due to advantages such as high energy density and low self-discharge, the lithium-ion battery has taken its part in the rechargeable energy storage market, and it is now found in most laptops, cameras and mobile phones. With the increasing demands for electrical vehicles and stationary energy storage systems, there is a necessity for improved lithium-ion battery materials.

In this thesis several alternative electrode materials have been examined with a main focus on the electrochemical characterisation. As an alternative to the commercial cathode $LiCoO_2$, the $LiMn_2O_4$ cathode has been suggested due to its reduced toxicity, material abundance, reduced costs and increased specific capacity. On the anode side, several Sn-containing anodes have been investigated and steps to overcome the main challenge, the great volume expansion upon cycling, has been taken. In addition, a novel anode material group was synthesised at the University of Marburg and two substances of the lithium chalcogenidometalate networks were successfully characterised.

The cathode material, $LiMn_2O_4$, was synthesised via the sol-gel technique and several coating methods such as dip-coating, electrophoretics and infiltration were investigated. The $LiMn_2O_4$ material was initially coated on a porous metal foam as a current collector, thus providing new possibilities as the porosity of the substrate increased, mechanical stability and adhesion improved and a 3-dimensional network was obtained. In order to compare the results of the $LiMn_2O_4$ cathode material on the novel current collector, the material was also coated on a standard metallic foil and characterised. The analysis followed via X-ray diffraction, electron microscopy, thermogravimetrical analysis and several electrochemical techniques.

Tin containing anode materials were chosen due to the doubling of the theoretical capacity compared with the commercially used graphite. However, a great challenge lies with using tin or tin-containing anode materials. Upon lithiation of Sn, the material can expand up to 300 %, therefore a stabilising effect is necessary to avoid a collapse of the material. This work shows several new concepts and attempts to overcome this challenge, including SnO_2 nanowires deposited via chemical vapour deposition on both metallic foam and standard current collectors. A new improvement consisted of the tin - carbon nanofibers where the nanofibers form a stabilising matrix that can partially buffer the volume change of the Sn particles. The synthesis of the Sn-containing anodes took place at the University of Cologne, while characterisation, cell preparation and optimising the electrode system were features of this thesis.

In addition, a lithium chalcogenidometalate network proved to be an interesting, new anode material group. Both $Li_4MnSn_2Se_7$ and $Li_4MnGe_2S_7$ (synthesised at Philipps-Universität Marburg) were electrochemically examined to better understand the lithiation processes. Both materials obtained very high specific capacities and were found to be possible alternatives to the state-of-the art anodes.

All the examined electrode materials were found to have some advantage over the commercially used $LiCoO_2$ and graphite electrodes, and a thorough characterisation of the materials was performed to understand the processes that took place.

Zusammenfassung

Lithium-Ionen Batterien sind in den letzen Jahrzehnten immer wichtiger geworden und haben mittlerweile andere Energiespeichersysteme in weiten Bereichen ersetzt. Ihre hohe Energiedichte und niedrige Selbstentladung sind Gründe dafür, dass die Lithium-Ionen Batterie einen großen Teil des Marktes für wiederaufladbare Energiespeicher einnimmt und ist in Laptops, Kameras und Handys zu finden. Mit dem zunehmenden Interesse an Elektrofahrzeugen und stationären Energiespeichersystemen entstand der Bedarf an verbesserten Lithium-Ionen Batteriematerialien.

Verschiedene alternative Elektrodenmaterialien mit einem Hauptfokus auf ihrer elektrochemischen Charakterisierung wurden in dieser Dissertation untersucht. Als eine Alternative zum kommerziellen $LiCoO_2$ wurde $LiMn_2O_4$ als Kathode vorgeschlagen, hauptsächlich aufgrund der niedrigeren Toxizität, der Materialverfügbarkeit und der erhöhten spezifischen Ladung. Auf der Anodenseite wurden verschiedene Sn-haltige Anoden untersucht um das vorangige Problem der Volumenausdehnung beim Laden/Entladen zu lösen. Außerdem wurde mit den Lithium-Chalkogenidometallaten ein neuartiges Anodenmaterial synthetisiert und erfolgreich charakterisiert.

Das $LiMn_2O_4$-Kathodenmaterial wurde mittels einer Sol-Gel-Methode hergestellt und verschiedene Beschichtungsmethoden wie, Tauchbeschichtung, Elektrophorese und Infiltration, untersucht. Zunächst wurde ein hochporöser metallischer Stromableiter mit dem $LiMn_2O_4$-Material beschichtet, was neue Elektrodenbauformen ermöglicht. Die Porosität des Substrats kann erhöht und die mechanische Stabilität und Haftung verbessert werden. Außerdem ist ein 3-D Netzwerk vorhanden. Ein Vergleich mit $LiMn_2O_4$ auf einer metallischen Standardfolie wurde durchgeführt und eine allgemeine Charakterisierung mittels Röntgenbeugungsanalyse, Elektronenmikroskopie, Thermogravimetrie und elektrochemischen Methoden folgte.

Aufgrund ihrer im Vergleich zu kommerziellem Graphit verdoppelten theorethisch speicherbaren Ladung wurden zinnhaltige Anodenmaterialien gewählt. Es besteht jedoch eine große Herausforderung bei Sn-haltigen Anoden, da sich das Material bei Lithierung des Sn um bis zu 300 % ausdehnt. Ein stabilisierender Effekt ist nötig, um einen Zusammenbruch des Materials zu vermeiden. In dieser Arbeit werden neue Konzepte und Bestrebungen zur Lösung aufgezeigt. Dies umfasst die Abscheidung von SnO_2-Nanodrähten auf metallische Schäume und auf glatte Stromableiter. Eine weitere Verbesserung besteht aus Sn-Kohlenstoffnanofasern, bei denen die Nanofasern ein stabilisierendes Gerüst darstellen, so dass die Volumenausdehnung der Sn-Partikel teilweise aufgenommen wird. Die Synthese der Sn-Anoden wurde an der Universität zu Köln durchgeführt, die weitere Charakteriserung, Zellpräperation und Optimierung des Elektrodensystems waren Schwerpunkte dieser Dissertation.

Weiterhin hat sich das Lithium-Chalkogenidometallat Netzwerk als ein interessantes Anodenmaterial erwiesen. Beide Materialien, $Li_4MnSn_2Se_7$ und $Li_4MnGe_2S_7$ (hergestellt an der Philipps-Universität Marburg), wurden elektrochemisch analysiert, um die Lithierungsprozesse im Detail zu verstehen. Beide Materialien erreichen sehr hohe spezifische Ladungen und können als denkbare Alternativen zum Stand der Technik betrachten werden.

Alle untersuchten neuen Elektrodenmaterialien zeigen Vorteile gegenüber der kommerziellen $LiCoO_2$- und Graphit-Elektroden. Zum besseren Verständnis der grundlegenden Prozesse wurde eine umfassende Charakterisierung der Materialien durchgeführt.

Danksagung

Hiermit möchte ich allen danken, die am Zustandekommen dieser Arbeit beteiligt waren.

Mein ganz besonderer Dank geht an meinen Betreuer, Dr. Kai-Christian Möller, der mir jederzeit mit Rat und Tat geholfen hat. Vor 4 Jahren ließ er sich nicht von meinen fehlenden Deutschkentnisse abschrecken und nahm mich mit in seinem Team aufs. Vielen Dank für deine unerschöpfliches unerschöpfte Fachwissen, viel Geduld und Zeit!

Ein weiterer Dank gilt meinem Doktorvater Prof. Dr. Gerhard Sextl, insbesondere für die Möglichkeit, dieses spannende Thema am Institut zu bearbeiten und für die Korrektur der Arbeit.

Ich möchte mich auch bei allen Kollegen im Zentrum für Angewandte Elektrochemie herzlich bedanken, ohne dsie wäre es nie möglich gewesen wäre, diese Arbeit überhaupt durchzuführen. Ich habe eure Zusammenarbeit, Hilfsbereitschaft und Freundschaft sehr geschätzt. Vor allem schulde ich Herrn Henning Lorrmann ein großen Dank, da ohne seine Unterstützung, Zusammenarbeit und Kreativität unsere Projektarbeit nicht gelungen wäre. Ein weiterer Dank geht auch an allen KoLiWIn-Projektpartner, besonders die Kollegen aus der Universität zu Köln und Philipps-Universität Marburg.

Auch möchte ich mich bei meinen Freunden bedanken, die mich nicht nur tatkräftig unterstützt haben, sondern mich stets aufbauten und für die erforderliche Abwechslung sorgten.

An meinen Eltern: Jeg er veldig takknemlig for hjelpen og støtten deres. Dere har gjort den lange veien hjem kortere og alltid akseptert mine valg, tusen takk!
Und schließlich möchte ich ganz herzlich meinen Freund Christian danken. Ohne dich hätte ich diesen Schritt nicht gemacht, vielen lieben Dank für deine Geduld und Verständnis. ♡

Herzlichen Dank!

Contents

Chapter 1

Introduction

Due to advantages such as high energy density and low self-discharge, lithium-ion batteries have gained a large part of the rechargeable energy storage marked. With the increasing interest in electrical or hybrid vehicles as well as stationary energy storage systems, there is a great need for improved materials for lithium-ion batteries. This thesis deals with the state-of-the-art technique of lithium-ion batteries, and new electrode materials on both anode and cathode side are synthesised and characterised.

The background of this work is the BMBF founded project KoLiWIn (Konzeptstudien für neuartige Lithium-Ionen Zellen auf Basis von Werkstoff-Innovationen). KoLiWIn is a part of the LIB2015 innovation alliance to sponsor consortiums that are engaged in lithium-ion battery research. Industry, research institutes, universities and the federal ministry of education and research came together and committed to research and development on this topic.
The KoLiWIn project consists of five universities, three Fraunhofer institutes and one industrial partner, with the main goals to develop new anode material systems in addition to multi-scale simulation. The entire lithium-ion battery cell has been investigated, including cathode, anode, electrolyte as well as casing and cell assembly.[1] The main electrochemical characterisation was performed at Fraunhofer ISC and in scope of this project the thesis had some guidelines.

The $LiMn_2O_4$ cathode material has been synthesised via the sol-gel route and coated on both a porous current collector and a metallic foil. Several coating methods have been examined to understand and to vary the loading properties, the homogeneity of

the cathode layer and the electrochemical properties. $LiMn_2O_4$ was chosen as the cathode material due to it's low toxicity compared to the commonly used $LiCoO_2$ cathode, as well as abundance and high theoretical capacity. The focus on the porous current collector was to examine the benefits of the increased surface area, together with a 3D-structure of the substrate. The synthesis of the cathode material was examined and the resulting product was characterised with the means of inductively coupled plasma, thermogravimetric analysis, X-ray diffraction and electron microscopy. The next step involved the treatment of the porous current collector and the adhesion of the cathode material as well as the effects between the two components. This step was further characterised with the methods above, as well as extensive electrochemical characterisation. Lastly, the $LiMn_2O_4$ coated on a porous current collector was compared with $LiMn_2O_4$ coated on a standard metallic foil.

Several anode materials were fabricated and characterised in the KoLiWIn project. In this thesis high capacity tin-containing anodes were examined in close cooperation with the University of Cologne. With their expert knowledge of the synthesis of metal oxide compounds and nanostructured concepts, the Sn-containing anodes were fabricated by the colleagues at the University of Cologne, as well as some initial structural characterisation. This thesis focuses on the electrochemical characterisation of these anode materials, as well as the further development and new concepts of architecture and composition. Initial tests consisted of the improvement of SnO_2 nanowires, which lead to the fabrication of tin-carbon nanofibers where the carbon acted as a matrix to buffer the large expansion of the Sn particles during electrochemical cycling. The last improvement combined the benefits of the porous current collector used for the cathode material with the high capacity of Sn-containing anodes.

Another possible anode group was developed and characterised in cooperation with the Philipps-Universität Marburg. A brand new Li^+-intercalating quaternary chalcogenidometalate network was synthesised in Marburg resulting in two possible anode materials where the lithium-ions are situated in the holes of the network, giving a stable material with a high capacity compared with the commercially used graphite anode. Initial electrochemical characterisation was performed at Fraunhofer ISC, a necessity as the lithium chalcogenidometalate networks were not previously synthesised to be used as a lithium-ion battery anode, and the lithium insertion in the

open channels had to be confirmed. The anode material itself was synthesised by the colleagues at the Philipps-Universität Marburg, whereas the following preparation and characterisation found in this thesis were performed at Fraunhofer ISC.

This PhD-thesis gives a literary review of the state-of-the-art electrode materials and describes the synthesis of the improved electrode materials with an emphasis on the electrochemical characterisation thereof.

Chapter 2

Theoretical Background

2.1 Li-ion batteries

The lithium-ion battery (LIB) was developed in Japan by Asahi Kasei Company and later commercialised by Sony in 1991. The benefits of the lithium-ion battery, such as high-energy density, good performance and no memory effect, gave the battery a rapid acceptance in the market. The fact that lithium is the lightest metal element, giving it a high gravimetric density, and lithium being the most electropositive metal, with -3.04 V versus standard hydrogen electrode, facilitates an electrochemical storage system with high energy density.[2, 3] The first generation of lithium-ion batteries consisted of $LiCoO_2$ and graphite and made a major break-through for power source applications and portable electronic devices like wireless telephones and laptop computers.[4]

Lately the need for clean energy sources has increased, and with that comes new energy storage systems. To significantly reduce the CO_2 emissions, zero emission vehicles must replace the internal combustion engines in the automotive industry. Lithium-ion batteries have become an important part in the realisation of electric vehicles, as well as in hybrid electric vehicles and plug-in electric vehicles. As renewable energy sources are increasing worldwide, high efficiency energy storage systems such as stand-alone power plant will play a greater role in the future.[5]

A battery's amount of electrical energy can be expressed either per unit of weight (Wh kg^{-1}) or per unit of volume (Wh l^{-1}), and is a function of the cell potential (V)

and capacity (Ah kg^{-1}). Table 2.1 summarises the benefits of the lithium-ion battery in comparison with other known battery types.

Table 2.1: Comparison of different battery types and their properties.[6, 7]

Battery type	Operating voltage (V)	Energy density ($Whkg^{-1}$)	Comments
Lead-acid	1.9	30	Commonly known as car battery, low energy density
Alkaline	1.5	50-80	Not rechargeable, high capacity for low-power devices
Ni-Cadmium	1.2	50	Memory effect, environmental pollution, low energy density
Ni-metal hydride	1.2	60	Memory effect, low energy density
Lithium-ion	4.0	150	Light, high voltage, no memory effect, high capacity, good charge retention, expensive

The maximum energy that can be derived from a battery cell is mainly based on the types of active materials that are used and the amount of active materials. However, in practice only a fraction of the theoretical energy of the battery is achieved. This is due to the need for electrolyte, separators, current collectors and other nonreactive components, such as containers and casings. This relation is illustrated in figure 2.1. In order for lithium-ion batteries to complete the passage into electric vehicles and larger stationary storage systems, the technology of lithium-ion battery has to be improved. For a commercialisation, the costs have to be reduced and safety is an increasingly important issue. Other important factors are cyclability, increased energy and power density, as well as improving the temperature range of operating cells.[3, 8]

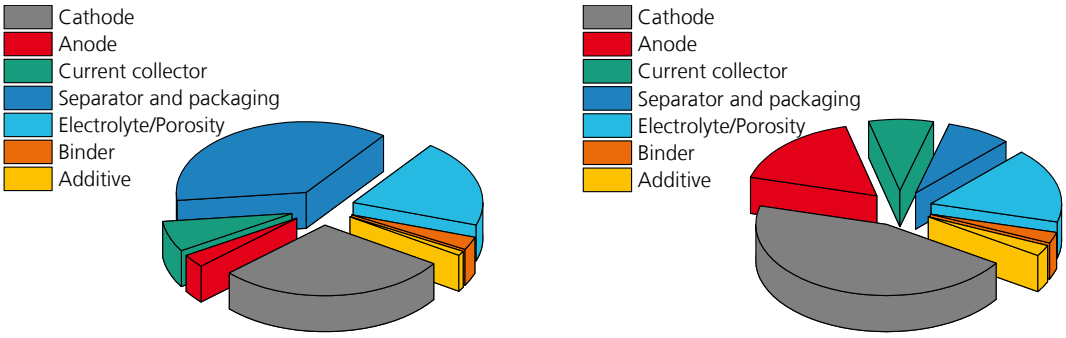

Figure 2.1: Components of a battery cell, left pie chart is cost based and right pie chart is mass-% based. Adapted from Dillon et al.[9].

2.2 Electrochemical principles of a lithium-ion battery

Lithium-ion batteries consist of two lithium insertion materials, in its most conventional form, a graphite anode, and a lithium metal oxide cathode, commonly $LiCoO_2$. With the use of an electrolyte containing a lithium salt, the lithium-ions shuttle between the positive and negative electrode. More specifically, Li-ions are inserted into/extracted from a solid matrix without the destruction of the bulk material, while simultaneously, electrons are extracted from one electrode and inserted into the other, thus storing and delivering electrical energy. This shuttle of lithium-ions has given the name rocking-chair cell to the system.[3–5]

Figure 2.2 displays the schematics of a typical lithium-ion battery, consisting of graphite as anode and a lithium metal oxide as cathode. Upon charging the lithium-ions intercalate into the negative electrode, the positive material is oxidised, while the negative material is reduced. On discharge, the reverse happens.[8] The electrode reactions and overall reaction can be seen below.

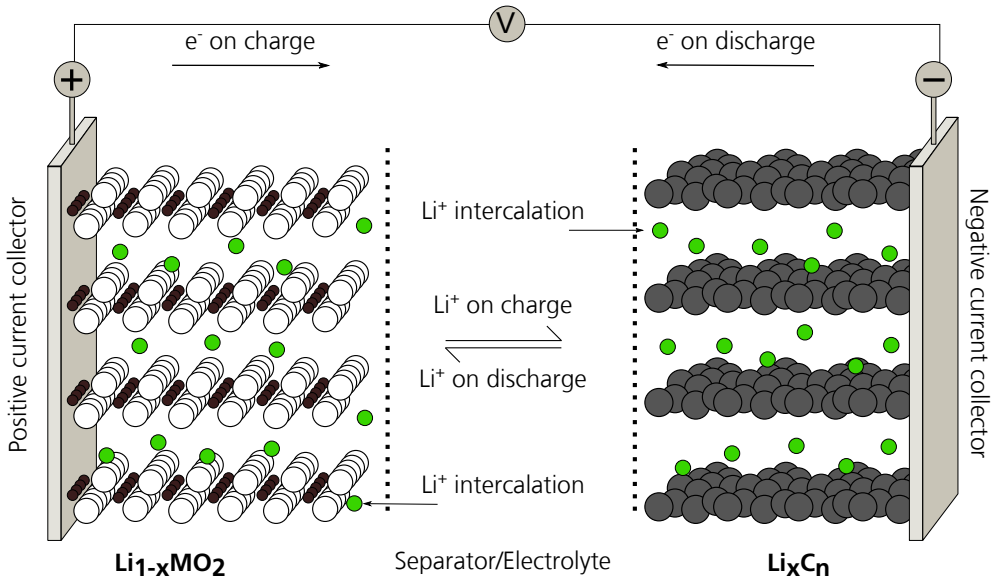

Figure 2.2: Schematic of the charge/discharge process in a lithium-ion battery, adapted from Linden et al.[8].

$$\text{Positive :} \qquad LiMO_2 \underset{\text{discharge}}{\overset{\text{charge}}{\rightleftharpoons}} Li_{1-x}MO_2 + xLi^+ + xe^- \tag{2.1}$$

$$\text{Negative :} \qquad C + xLi^+ + xe^- \underset{\text{discharge}}{\overset{\text{charge}}{\rightleftharpoons}} Li_xC \tag{2.2}$$

$$\text{Total :} \qquad LiMO_2 + C \underset{\text{discharge}}{\overset{\text{charge}}{\rightleftharpoons}} Li_xC + Li_{1-x}MO_2 \tag{2.3}$$

The available energy of a battery will mostly depend on the basic electrochemical reactions at both electrodes, although there are several other factors affecting the performance or rate capability of a cell. Electrode design, electrolyte conductivity and separator characteristics are among the factors that would influence the charge-transfer reaction, diffusion rates and magnitude of energy loss.[8]

Three different kinetics play a major role for the overall polarisation, which can be seen in figure 2.3. Firstly, the activation polarisation is related to the kinetics if the charge-transfer reactions taking place at the electrode/electrolyte interface. The ohmic polarisation can be attributed to the resistance of the individual cell components and to the resistance due to contact problems between the cell components.

Lastly, the concentration polarisation is due to mass transport limitations during cell operations.[7] Figure 2.3 also illustrates the current-voltage characteristics on discharge, a common electrochemical technique to determine the cell capacity, the effect of the discharge-charge rate and general information on the state of the battery.

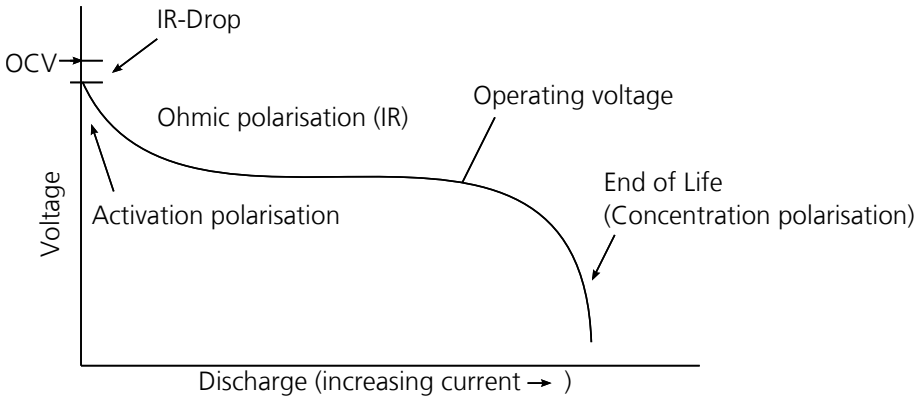

Figure 2.3: A typical discharge curve of a battery, showing the influence of different types of polarisation, adapted from Winter and Linden et al.[7, 8].

The losses that can be seen in figure 2.3 are to be avoided when possible, and to minimise the polarisation losses certain guidelines (seen below) are important for all batteries.[8]

- An electrolyte with a lower conductivity will give a higher ohmic polarisation.
- The electrolyte, including both salts and solvents, should be chemically stable within the cell range to avoid unwanted reactions with the electrode materials.
- The activation polarisation can be reduced by increasing the rate of electrode reaction at both anode and cathode. A porous electrode design will give a high electrode surface and thus minimise the charge-transfer polarisation.
- The cell should have adequate electrolyte transport to facilitate the mass transfer, and thus avoid building up excessive concentration polarisation. In most battery systems, the reactants must diffuse or be transported away from the electrode surface. Porosity, pore size, separator properties and concentration of the reactants influence the mass transfer.
- The current collectors should be compatible with the electrode material and the electrolyte and not cause corrosion problems.

- The reaction products should facilitate the reversible reactions during charge and discharge, as well as being mechanically and chemically stable with the electrolyte.

2.3 Anode materials

For the rechargeable lithium-ion battery, metallic lithium as anode was quickly replaced by carbonaceous material due to safety issues. In the first phase of lithium-ion battery commercialisation coke was used as the anode material[10], however, the Mesocarbon Microbeads (MCMB) soon became more popular as a result of the higher specific capacity (300 mAh/g) and better safety properties[8]. The current choice of anode materials is graphite due to its long cycle life, low and flat working potential, abundant material supply and relatively low cost. Compared to MCMB the specific capacity can be increased to 372 mAh/g.[11]

Many types of carbon materials are industrially available, and the structure of the carbon greatly influences its electrochemical properties, including lithium intercalation capacity and potential. In figure 2.4 the basic building block can be seen on to the left, a planar sheet of carbon arranged in a hexagonal array. When these planar sheets are stacked, the different graphite structures occurs. The ABAB stacking results in the more common hexagonal graphite, whereas a stacking order of ABCABC gives the rhombohedral graphite.[8]

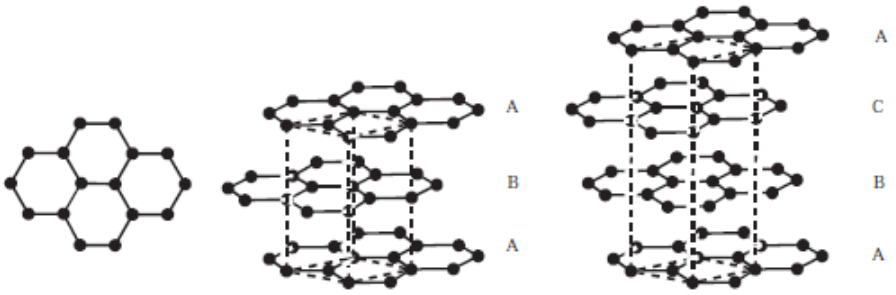

Figure 2.4: The structure of a carbon layer, hexagonal and rhombohedral graphite.[8]

The most Li-enriched intercalation of graphite has a stoichiometry of LiC_6, meaning one lithium-ion per 6 carbon atoms intercalate, resulting in the theoretical specific capacity of 372 mAh/g. However, compared to other intercalation materials (such

as Si/C composites), this capacity is still less than desired, and the practical energy density is too low.[11, 12] Two major types of carbon are often mentioned; soft and hard carbons. Materials that can be graphitised by treatment at high temperature are termed soft carbons, hard carbons cannot be readily graphitised.[8] Hard and soft carbons have a wide range of capacities depending on starting materials and processing conditions, although hard carbons tend to have a higher capacity than graphite as well as a faster rate capability.[13, 14]
To increase the energy and power density of lithium-ion batteries, nanostructured carbonaceous anode materials have been developed to create more active spaces and sites for lithium storage. 1D nanostructured carbon materials include nanotubes, nanowires and nanofibers, giving excellent surface activities and high surface-to-volume ratios. A promising candidate is electrospun carbon nanofiber (CNF). It is shown to promote fast lithium insertion as well as an improved reversible capacity of about 450 mAh/g.[12] Two dimensional carbon includes graphene, a monolayer structure of honeycomb carbon lattice. As lithium can be bound on both sides of the graphene sheet as well as on edges, defects and disorders, graphene is considered to have a high Li-storage ability and achieving discharge capacities over 500 mAh/g[15]. However, increased irreversible capacity is often observed due to SEI-formation and loss of electrolyte. Lastly, the porous carbons have been shown as promising anode materials for LIBs due to their high surface areas and open pore structures. Interconnected nanopores lead to effective diffusion pathways for Li-ions and would increase the volumetric capacity of the material. In summary, the electrochemical performance of nanocarbons (1D, 2D, and porous carbons) is largely determined by their structures and morphologies.[12]

Lately, there has been an increased interest in finding new anode materials for lithium-ion batteries. Materials with enhanced safety, low cost, higher energy density and long cycle life are necessary for the further development of LIBs.[10–12, 16] Figure 2.5 displays the specific capacities of certain anode materials and illustrating the possible improvement in theoretical capacity compared to the state-of-the-art graphite anode material.

In particular group IV elements have proven to possess the wanted lithium insertion properties needed for the anode material. Group IV is commonly called the carbon

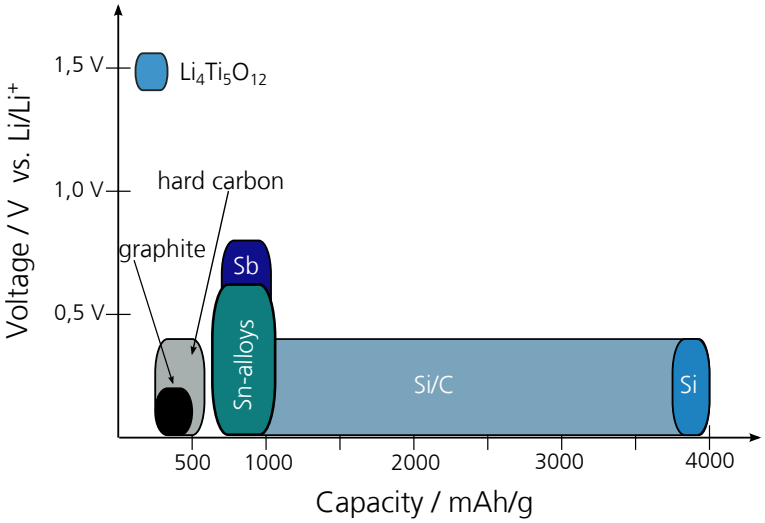

Figure 2.5: Specific capacity of anode materials, adapted from Möller[17].

group since carbon is one of the important elements in this group, however also silicon, germanium and tin can form alloys with Li.[12] As can be seen in figure 2.5 and in table 2.2 the capacities of alloy anodes are 2-10 times higher than that of graphite.

Table 2.2: Comparison of the theoretical capacity, charge density, volume change and onset potential of various anode materials.[11]

Materials	Li*	C	$Li_4Ti_5O_{12}$	Si	Sn	Sb
Density / g/cm^3	0,53	2,25	3,5	2,33	7,29	6,7
Lithiated phase	Li	LiC_6	$Li_7Ti_5O_{12}$	$Li_{4,4}Si$**	$Li_{4,4}Sn$**	Li_3Sb
Theoretical specific capacity / mAh/g	3862	372	175	4200	994	660
Theoretical charge density / mAh/cm^3	2047	837	613	9786	7246	4422
Volume change / %	100	12	1	320	260	200
Potential vs. Li / V	0	0.05	1.6	0.4	0.6	0.9

* In comparison to the other materials Li is used to assembly cells in the charged state, therefore the capacity for reduction is given. Comparing with the high-capacity Si, the reduction potential would only be around 2000 mAh/g.

** The correct compounds are $Li_{22}Si_5$ and $Li_{22}Sn_5$, however, the abbreviated versions $Li_{4,4}Si$/$Li_{4,4}Sn$ are often used in the battery research community.

The main challenge for the implementation of alloy anodes is the large volume

change during lithium insertion and extraction. This volume expansion (often up to 300 %) leads to pulverisation of the active particles and poor cycle stability. In addition, the irreversible capacity loss in the first cycle of the alloy anodes is too high.[11, 16, 18] Details of theoretical capacity, charge density and volume change can be found in table 2.2.

The theoretical specific capacities vary between 175 mAh/g for $Li_4Ti_5O_{12}$ (LTO) and 4200 mAh/g for silicon, while the volume expansion upon lithiation show a reverse behaviour with 1 % for LTO and over 300 % for the lithiated phase of Si. These enormous volume changes cause irreversible capacities and capacity fade during cycling. The irreversible capacity is measured as the difference between the first charge and discharge capacity, also known as the coulombic efficiency. For many alloy anode materials the coulombic efficiency can be as low as 25 %.[11] The causes of these irreversible capacity losses for alloy anodes are considered to be the following:

1. Loss of active material. During cycling the volume changes dramatically, thus introducing a mechanical stress on the system. The electrode suffers from pulverisation as well as loss of electronic interparticle contact.[18]

2. Formation of solid-electrolyte interphase (SEI) films. When the SEI is formed, lithium is incorporated into the passivation film. This process is irreversible, thus giving a loss in capacity, primarily in the cell's first cycle.[8] A more detailed description of the SEI layer is given in chapter 2.5.1. The composition of the SEI films formed on alloy anodes are different from that on graphite. In graphite, a stable SEI film is normally developed during the first cycle, in contrast, the SEI formation on alloy anodes appears to be a more dynamic process with continuous losses over several cycles due to the ongoing volume expansion.[11]

3. Aggregation of alloy particles. Electrochemical aggregation in nanosized alloy anodes has been observed, it leads to an increased Li diffusion length and is one of the key factors to capacity fading.[19]

4. Trapping in the host alloy. Li insertion is generally reversible, but some Li-ions may be permanently trapped in the alloys due to slow lithium kinetics, formation of highly stable lithitated compounds or a strong bonding at defect

sites. A presence of impurities such as S, O and C could lead to the formation of stable lithium compounds, leading to irreversible capacity loss.[11]

Extensive research has been carried out to address the issues above, and significant progress has been achieved. The following chapter lists some of the new improvements, the ideas and the theoretical background related to the results in this thesis.

2.3.1 Metal oxide anode materials

Various metal oxides have been investigated as potential anode materials for rechargeable LIBs because these materials have diverse chemical and physical properties, they can deliver high reversible capacities [12] and they can be easily synthesised [20]. SnO_2 is one of the most important metal oxides in this category. During the first charging cycle, Li will bond to the oxygen in SnO_2 and form Li_2O and pure tin, as can be seen in the alloying mechanism below.

$$SnO_2 + 4Li^+ + 4e^- \rightarrow Sn + 2Li_2O \tag{2.4}$$

$$Sn + xLi^+ + xe^- \rightarrow Li_xSn \qquad (0 \leq x \leq 4.4) \tag{2.5}$$

As can be seen from mechanism 2.5, a total of 4.4 lithium-ions could theoretically be inserted into the Sn-compound, thus leading to a far greater theoretical capacity as in graphite. The theoretical capacity of SnO_2 is 781 mAh/g[21], twice that of graphite. It has been reported that Sn phases produced from the delithiation of the Li-Sn alloy have a tendency to aggregate and form clusters.[12] H. Li et al.[10] have described how the formation of $Li_{4.4}Sn$ from stand-alone tin leads to a significant volume expansion and thus a poor cyclic performance. Therefore it is proposed that the Li_2O matrix that is being formed in mechanism 2.4 acts as a glue to reduce the aggregation of tin atoms.[10, 12, 20]

However, SnO_2 electrodes face many of the same challenges with volume change upon lithiation/delithiation. To overcome the resulting irreversible capacity losses certain approaches are significant. Porous SnO_2 nanostructures, SnO_2-based nanocomposites, nanostructured SnO_2 thin films and hollow core-shell mesospheres are

different material structures developed in this direction. In a porous structure, the volume changes can be suppressed since the pores act as a structure buffer for the large volume change, and the reversible capacity can be significantly increased.[12] The same principle goes for nanostructures like nanowires, nanotubes etc. The volume changes can be partly buffered by the increased surface area.
D. Deng et al.[16] reports composite compounds using the beneficial properties of carbon together with SnO_2. A nanoscale SnO_2 compound with a carbon coating or core-shell structures can employ both the high capacity of SnO_2 as well as the good cyclability of carbon. For these SnO_2/carbon nanocomposites, carbon acts as a barrier to prevent the aggregation between SnO_2 particles by providing a buffering space where SnO_2 and Sn particles can experience the volume change without collapsing.[12] The synthesis of such SnO_2 anodes can be seen in chapter 3.1.3 and the characterisation thereof in chapter 5.1.

2.3.2 Sn-based alloy anode materials

An equilibrium phase diagram of Li-Sn can be seen in figure 2.6. The different compositions include $Li_{22}Sn_5$, Li_7Sn_2, Li_3Sn, Li_5Sn, LiSn and Li_2Sn_5, and these intermetallics can be produced by the electrochemical lithiation of a tin electrode immersed in a Li-ion containing electrolyte.[22] As described in equation 2.5 the most lithiated phase $Li_{22}Sn_5$/$Li_{4.4}Sn$ corresponds to a theoretical capacity of 994 mAh/g (Table 2.2). The higher theoretical capacity of Sn compared to that of SnO_2, relates to equation 2.4, and the lost energy in the transfer from SnO_2 to pure Sn.

As previously mentioned, the alloy anode materials also suffer from great volume changes during cycling of the electrode material, and this is the major challenge in the commercialisation of the tin-based anode. (Although the Sn-based Nexelion battery from Sony has been on the market since 1995.[22]) Several strategies have been investigated to overcome the large volume expansion and preserve the structural integrity of the Sn-anode system. The first approach involves the preparation of unique nanostructures. Depending on the morphology, the resulting anodes could better accommodate the large stress and strain without cracking.[12] M. Winter et al.[18] documented the effects of tin-morphology by comparing coarse and fine

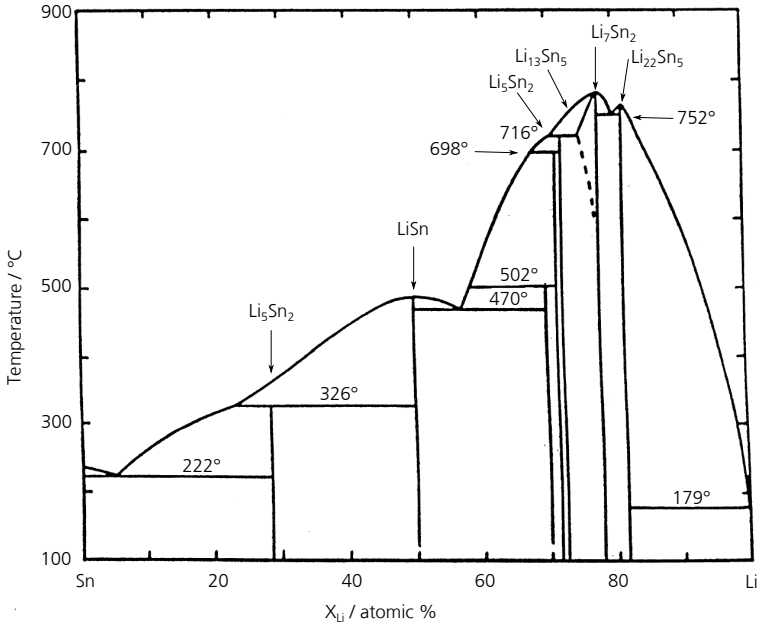

Figure 2.6: A Li-Sn phase diagram, adapted from Sangster[23].

tin particles, investigation the charge recovery and the degradation through SEM images after cycling. It was shown that coarse tin particles gave rise to the formation of larger cracks and the delimination of active material from the substrate. Some of the same effects were seen with the fine tin electrode, but at a much later stage.

The second approach to improve the properties of Sn-based anodes is to introduce a second component to form composites. An inactive-matrix composite can be used, where the matrix basically absorbs the volume change during cycling, and possibly improving the electronic conductivity of the electrode. In active-matrix composite anodes, both the active phase and the host matrix are reactive towards lithiation. The idea of the active composite is to have one component lithiathed while the other acts as the buffer as they react with Li at different onset potentials. For example in a SnSb alloy, Sb would begin Li insertion at 0.9 V vs. Li/Li^+, while Sn would remain unreacted until a potential of 0,6 V vs. Li/Li^+ is reached.[11, 12]

The third approach uses also the active-matrix composite, but specifically with carbon. An improved cycle performance when using carbon as a matrix has been reported [11, 12, 16] and can be attributed to the improved electronic conductivity and the buffering effect of carbon. A well designed Sn/C composite could combine

the high specific capacity of Sn with the cyclability of carbon, the importance lies in finding the right balance between the two components. A description of the synthesis of such Sn/C composite is seen in chapter 3.1.3 and the following electrochemical characterisation can be seen in chapter 5.2.

Another method used to overcome the problem of the large volume expansion is to design a three-dimensional porous electrode structure with sufficient porosity to accommodate the volume changes. The active material can be deposited onto a porous current collector resulting in an improved cycle life.[11] M. Yoshio et al.[24] reported of the deposition of a silicon anode on a nickel foam current collector and how it showed an improved stability for over 400 cycles. The benefits of using a porous current collector are listed in chapter 2.5.3 and electrochemical results of a Sn anode on nickel foam can be found in chapter 5.1.2.

2.4 Cathode materials

For lithium-ion batteries there are two categories of cathode materials. One comprises layered compounds with an anion close-packed lattice, transition metal cations occupy alternative layers between the anion sheets, and lithium-ions are inserted into the remaining empty layers. The spinels with transition metal cations ordered in all the layers are included in this group as well. Hence, cathodes like $LiCoO_2$, $LiNiO_2$, $LiNi_{1-x}Co_xO_2$ and $LiMn_2O_4$ belong in this group. This class of materials has the advantage of higher energy density owning to their more compact lattices, and their topology offers highly accessible ion-diffusion pathways[25, 26].
Where the first cathode material group has a rather compact lattice, the second group of cathode materials has more open structures, such as vanadium oxides and the transition metal phosphates like $LiFePO_4$ and $LiMnPO_4$.[27] A summary of the available cathode materials and their specific capacities can be seen in figure 2.7.

As previously mentioned, the first generation of lithium-ion batteries consists of $LiCoO_2$ and graphite. $LiCoO_2$ has long been a popular cathode material due to convenience, simplicity of preparation and high operating voltage.[27] Li_xCoO_2 exhibits excellent cyclability at room temperature for $1 > x > 0.5$. The theoretical capacity

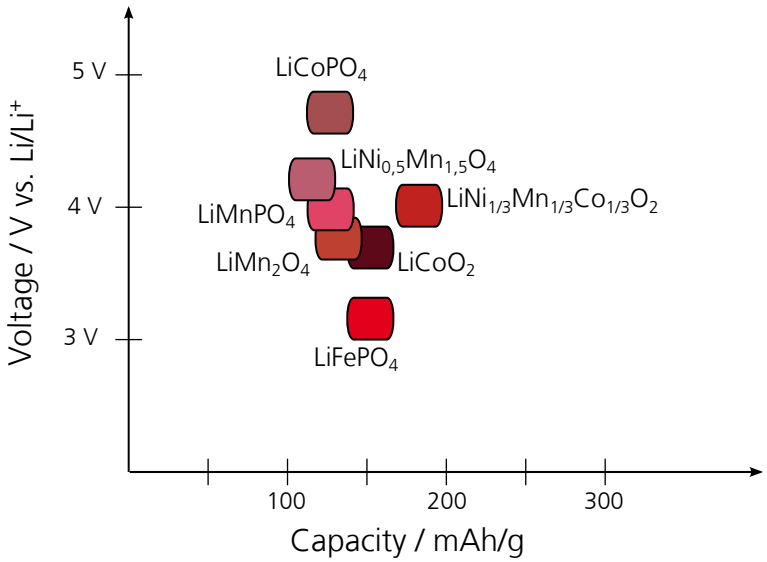

Figure 2.7: Specific capacity of cathode materials, adapted from Möller[17].

of $LiCoO_2$ is 274 mAh/g (calculated from complete delithiation), however, due to large anisotropic structure changes upon deep charging only half the lithium can be extracted resulting in about 50 % of its theoretical capacity.[6, 28] The $LiCoO_2$-system has been extensively studied since the time of commercialisation and the material is superior in cycling and shows a high structural stability.[29] On the other hand, $LiCoO_2$ is very expensive due to a limited availability of cobalt,[26] and $LiCoO_2$ is also highly toxic, which makes the need for other cathode materials a necessity.

As figure 2.7 shows, there are many possible cathode materials, some having benefits of higher specific capacities, improved cyclability and energy density, others having improved safety features or reduced cost. This thesis focuses on the use of $LiMn_2O_4$ as a cathode material, mainly because $LiMn_2O_4$ possesses advantages of less toxicity and an abundant materials source[27], but also because the spinel-framework structure gives a flat operating voltage of 3.95 - 4.1 V vs. Li/Li^+ with a theoretical capacity of 148 mAh/g[4].

The crystal structure of spinel $LiMn_2O_4$ can be seen in figure 2.8. The manganese occupies the octahedral sites and lithium predominantly dominates the tetrahedral sites in the cubic-closed packed O^{2-} lattice[25], giving way for lithiation and delithiation in a 3-dimensional network of channels, rather than planes as for the $LiCoO_2$ structure.[30] The discharge process of $LiMn_2O_4$ proceeds in three steps, two around

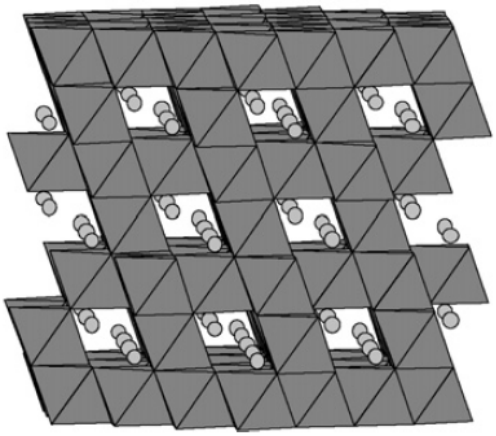

Figure 2.8: Illustration of the spinel crystal structure of $LiMn_2O_4$.[4]

4 V and the other around 3 V, although usually only the 4 V plateau is used.[26, 31] The discharge/charge process of $LiMn_2O_4$ at 4 V is a two-step redox reaction, which can be written as the following reaction[32]:

$$LiMn_2O_4 \rightleftharpoons Li_{0.5}Mn_2O_4 + 0.5e^- + 0.5Li^+ \tag{2.6}$$

$$Li_{0.5}Mn_2O_4 \rightleftharpoons Mn_2O_4 + 0.5e^- + 0.5Li^+ \tag{2.7}$$

A general problem for spinel $LiMn_2O_4$ is the capacity fading, especially at elevated temperatures. The following factors are considered to be the main reasons for this capacity fade:[6, 25, 27, 29]

1. Dissolution of manganese. At the end of each discharge, the concentration of Mn^{3+} arrives at its highest level. The Mn^{3+} at the surface may disproportionate according to equation 2.8.[29]

   $$2Mn^{3+} \rightarrow Mn^{4+} + Mn^{2+} \tag{2.8}$$

   The Mn^{4+} will remain in the solid and the Mn^{2+} leaches into the solution. This dissolution is triggered by elevated temperatures (50-70 °C)[27], as well as certain acidic electrolytes (for example HF released from $LiPF_6$ will etch a $LiMn_2O_4$ electrode, see chapter 2.5.1).[25]

2. The Jahn-Teller effect. At the end of discharge, the Jahn-Teller effect, happening at first on the surface of several particles, may expand into the overall composition of $Li_{1+x}Mn_{2-x}O_4$.[29] The Jahn-Teller distortion is associated with the Mn^{3+} ion. With insertion of lithium-ions, the average valence of manganese ions decreases (the average manganese oxidation state is 3.58[26]) and this leads to a pronounced Jahn-Teller distortion.[27] As an effect from the Jahn-Teller effect the cubic spinel crystal becomes distorted tetragonal, resulting in a thermodynamically unstable system, as well as unit cell volume increase of 6.5 % associated with the cubic-to-tetragonal transition.[6]

3. Loss of crystallinity, development of microstrains due to lattice mismatch between two cubic phases formed on cycling, and an increase in oxygen deficiencies or oxygen loss upon cycling have also been suggested to be the source of capacity fade.[25]

As Mn^{3+} is often the cause of the capacity fading, many attempts have been done to increase the average oxidation state of $LiMn_2O_4$ and reduce the Mn^{3+} dissolution. One solution is doping with heteroatoms, and several elements have been introduced into $LiMn_2O_4$ to investigate these effects[25, 27]. Extensive research on doping with cations has been performed, and cations like Mg, Al, Ti, Cr, Fe, Co, Ni and Cu have been investigated as possible dopants. Anode doping includes oxygen, fluorine, iodine and sulfur used as dopants. Doping generally produces two kinds of effects; the favorable and the unwanted. The doping can increase Mn-valence and hence suppress the Jahn-Teller effect, improve the stability of the spinel frame, lower structural change during charge/discharge, increase conductivity and decrease the surface area resulting in decrease in contact area where active material can react and dissolute into the electrolyte. The unwanted effects include a decrease in Mn valence, a decrease in volume of the crystal unit of $LiMn_2O_4$ thus inhibiting movement of lithium and a reduced capacity compared to undoped $LiMn_2O_4$. Doping with heteroatoms is generally considered to be a trade-off between cycle life and capacity.[33]

Another approach to reduce capacity fading of $LiMn_2O_4$ is the controlling of particle morphology, where surface area can be reduced and particle size homogeneously distributed to enhance electrochemical properties.[6, 25, 29] Surface treatment of $LiMn_2O_4$ has also been proved to reduce the manganese dissolution. Oxide coating

such as nano-SiO_2, ZnO and CeO_2 can effectively enhance the electrochemical performance. Metal coatings and surface treatment with other electrode materials can also have a positive effect on the capacity fading as they mainly prevent the direct contact with the electrolyte and improve the structural stability.[34]

As figure 2.7 illustrates, there are also several other cathode materials that can be used in lithium-ion batteries, and some deserve to be mentioned even if they are not the focus of attention in this thesis. Olivine materials have recently become of interest, such as $LiFePO_4$, $LiMnPO_4$ and $LiCoPO_4$. In particular $LiFePO_4$ has shown to have relatively high specific capacity (170 mAh/g), a flat 3.5 V vs. Li voltage, reduced costs and a high intrinsic safety. The disadvantage of these olivine materials is the low conductivity, resulting in the need for carbon coating to assure a high rate capability.[5] The manganese family also offers other cathode possibilities, and the advantages of manganese, such as non-toxic and abundant, have been mentioned above. One example is $LiNi_xMn_yCo_zO_2$, where especially $LiNi_{1/3}Mn_{1/3}Co_{1/3}O_2$ has attracted much attention. These cathodes can operate in a large voltage range, possess sufficient structural and thermal stability, good cycle life,energy density and obtain capacities up to 180 mAh/g. [35, 36] The different properties of cobalt, nickel and magnesium allows for a certain tailoring of the cathode material. Figure 2.9 illustrates the chemical composition of such cathodes and the properties of the elements. The role of Mn is to order the lithium ions, Ni is the electrochemically active element whereas Co often stabilises the structure.[37, 38] Manganese compounds like $LiNi_{0.5}Mn_{1.5}O_2$ belong to the 5 V spinel oxides. Mn-substitution with large amounts of Ni leads to a 5 V plateau in addition to the 4 V plateau with a specific capacity of 145 mAh/g. However, the 5 V materials all suffer from the same challenge. With an operating voltage above 4.7 V, the chemical stability in contact with electrolytes is not warranted. Most commercial electrolytes are not compatible with this high voltage.[6]

2.5 Electrolytes, separators and current collectors

2.5.1 Electrolytes

The electrolyte is defined as a solution containing a salt and solvents, and constitutes the third key component of a battery, with the two first components being anode and

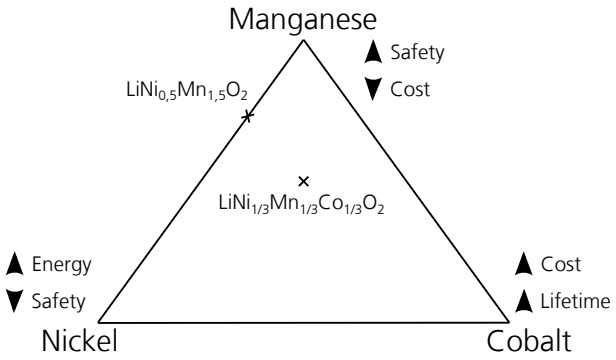

Figure 2.9: The properties and composition of $LiNi_xMn_yCo_zO_2$, adapted from Fischer[39].

cathode.[3] The role of liquid electrolytes in lithium-ion cells is to act as an ionic conductor to transport lithium-ions back and forth between positive and negative electrodes as the cells are charged and discharged.[2]

In general, every electrolyte is designed for a particular battery application, hence, several types of electrolytes have been used in lithium-ion batteries. Optimising an electrode material is only the first step in the process leading to its implementation in a practical cell. The capacity of a cell is dependent of the structural or electronic behaviour of its electrode, but poor cell lifetimes are often rooted in the side reactions occurring at the electrode-electrolyte interface, thus making the choice of electrolyte crucial.[3]

An ideal electrolyte would possess the following properties[6, 40]:

- Large electrochemical window, at least 4.5 V for lithium-ion cells with high voltage cathodes.
- High Li^+ conductivity over a wide temperature range.
- Retention of the electrode/electrolyte interface during cycling when the electrode particles are changing their volume.
- Good chemical and thermal stability.
- Low toxicity and low price.
- Safe materials, preferably nonflammable and nonexplosive.

Meeting all these requirements proves to be a considerable challenge, and several requirements are contradicting. Several types of electrolytes have been used in

lithium-ion batteries. Organic liquid electrolytes, ionic liquids, polymer electrolytes, inorganic solid electrolytes and hybrid electrolytes.[8] The organic liquid electrolytes are the most commonly used and longest commercially available. They consist of a solution of a lithium salt in organic solvents, typically carbonates, which are good solvents for Li salts, and have an oxidation potential at ca. 4.7 V. Ionic liquids have been recently considered as alternative electrolytes because they offer several advantages over the carbonate-based electrolytes, a high oxidation potential, non-flammability and better thermal stability. In spite of extensive research, no ionic liquids have yet been introduced onto larger power batteries.[40] Polymer electrolytes offer other advantages over their liquid counterparts, mostly in safety issues. A solid electrolyte can also act as the separator of the electrodes.

2.5.1.1 Formation of the SEI-layer

The most common electrolyte contains the lithium salt $LiPF_6$ in a mixed organic solvent (e.g ethylene carbonate-dimethyl carbonate, EC/DMC). For a commercial lithium-ion cell, the redox process of the graphite anode evolves at around 0.05 V vs. Li/Li^+, and that of the $LiCoO_2$ cathode at about 4 V. However, a commercially available electrolyte like $LiPF_6$ in EC/DMC is only stable in the domain from 4.5 V to about 0.8 V. As can be seen in figure 2.10, the redox process of graphite takes place in a region where the electrolyte itself would decompose. Normally it would be concluded that the $C/LiCoO_2$ battery is unstable in this electrolyte. However, the battery operates under a kinetic stability.[5] Many carbonate solvents undergo a limited reaction to form a passivation film on the electrode surface. This film spatially separates the solvent from the electrolyte, yet it is ionically conductive, and thus allows passage of lithium-ions. The passivation film, termed the solid electrolyte interphase (SEI), leads to an increased stability of the system.[8]

Extensive research have been carried out on the SEI formation on the anode side, and it has been proven that the different solvents contribute differently to the SEI formation.[2] As the SEI-layer is formed, lithium is incorporated into the passivation film. This process is irreversible, and thus followed by a noticeable loss of capacity, primarily in the first cycle.[8] On the cathode side, the formation of films through extensive cycling is known, but considerably less researched. Further investigations

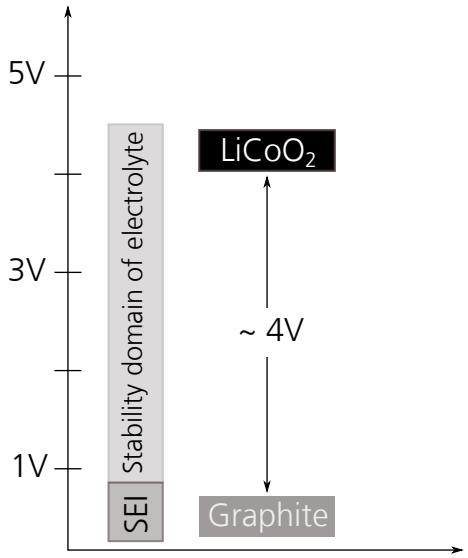

Figure 2.10: Voltage operation ranges of the C/$LiCoO_2$ electrode combination in comparison with the stability domain of most common liquid electrolytes, adapted from Scrosati et al.[5].

are needed to find electrolyte additives to improve SEI-layer, cathode protection and lithium salt stabilisation.[41, 42]

2.5.2 Separators

A separator is a porous membrane placed between electrodes of opposite polarity, it is permeable to ionic flow, but prevents electric contact of the electrodes.[2, 43] Essentially, the separator must be chemically and electrochemically stable towards the electrolyte and electrode materials. Structurally, the separator should have sufficient porosity to absorb liquid electrolyte for the high ionic conductivity. However, the presence of the separator adds electrical resistance and takes up limited space inside the battery, which in turn affects battery performance.[44] As a passive element of the battery system, the separator has attracted little scientific interest, and not much research is directed toward characterisation and development of new separators.[6]

A wide variety of properties are required of separators used in lithium-ion batteries:

- Electronic insulator. The electronic insulation has to be durable, effective over many years over a wide range of temperature, and in highly aggressive mediums.[6, 43]
- Mechanical strength. The separator must be mechanically strong to withstand

the tension of the winding operation during battery assembly.[8, 44]

- Chemical stability. The separator should be compatible and stable towards both electrolyte and electrode materials.[2]
- Porosity and pore size. An appropriate porosity is necessary to hold sufficient liquid electrolyte for the ionic conductivity between the electrodes, however the pore size must be smaller than the particle size of the electrode components.[44]
- Wettability. The separator should wet easily in the electrolyte and retain the electrolyte permanently.[8, 44]
- Shutdown. For battery safety, the separator should be able to shut the battery down when overheating occurs, so that thermal runaway can be avoided. The shutdown function can be obtained through a multilayer design of the separator, where at least one layer melts to close the pores, while the other layer provides mechanical strength to prevent physical contact of the electrodes.[44]
- Uniformity in thickness and pore distribution.[2, 43]

Battery separators can be divided into three types; microporous polymer membranes, non-woven fabric mats and inorganic composite membranes. Among them, the microporous polyolefin membranes have been most widely used in liquid electrolyte batteries due to their comprehensive advantages of performance, cost and safety. As can be seen in figure 2.11, there are many commercial battery configurations, all of which require special consideration when it comes to the choice of separators, electrolytes and also current collectors.

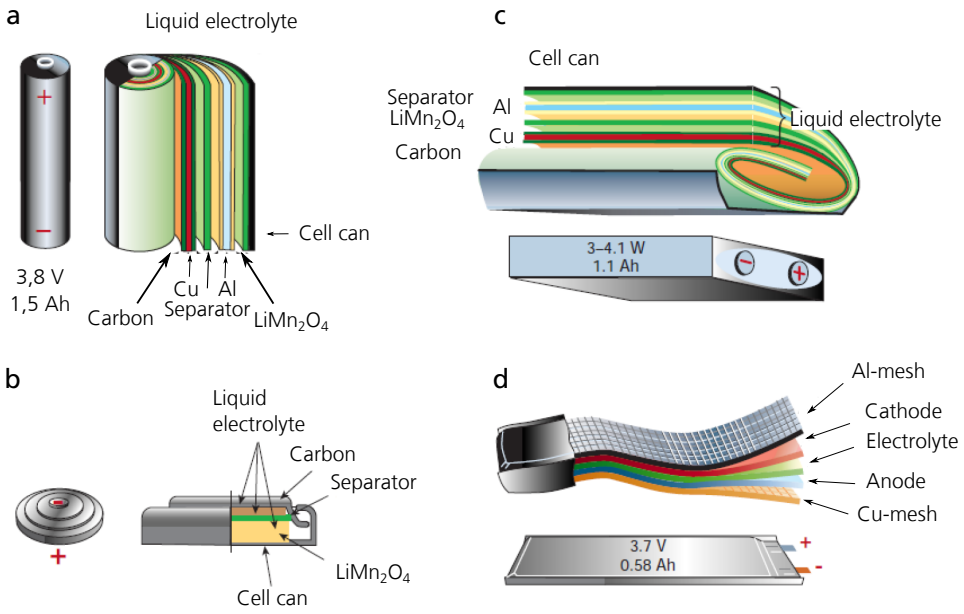

Figure 2.11: Schematic drawing showing the shape and the components of various Li-ion battery configurations. a) Cylindrical, b) coin, c) prismatic, d) thin and flat.[3]

2.5.3 Current collectors

The electrode materials are applied or coated onto current collectors. For most commercial cells, an aluminum foil is used for the positive electrode and copper for the negative electrode. Al is chemically stable for higher voltages and is extensively used between 3 - 5 V vs. Li/Li^+. However, for the lower voltages, Cu is the material of choice, being electrochemically stable in the range below 3 V vs. Li/Li^+.[45]

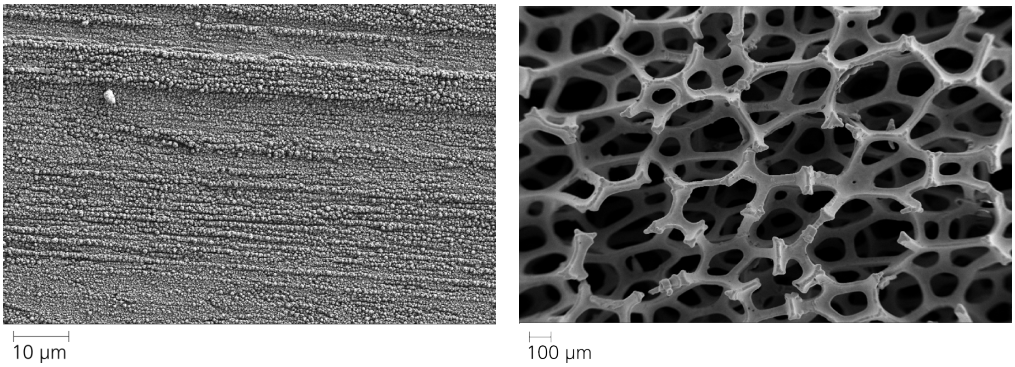

(a) (b)

Figure 2.12: SEM images of different current collectors. a) Surface of a copper foil, with dendrite coating to improve electrode adhesion, b) a nickel foam type current collector.

The thin foil current collectors have many beneficial properties like ease of preparation and coating as well as a certain flexibility of the electrode-foil system. However, with extensive cycling, the adhesion to the current collector is often reduced, and other configurations could accommodate the structure changes of the active material upon cycling.[46, 47] Recent research has focused on the use of a three-dimensional micro-porous current collector to improve the power performance of the electrodes. Such current collectors offers a high porosity, a specific surface area as well as uniform and enhanced mechanical strength.[48] Recently the use of Cu- and Ni-foams as current collectors has been reported, showing superior high-rate discharge capability due to its high surface area, increased electrical conductivity and buffering of the drastic volume expansion for some anode materials.[48, 49] Scanning electron microscope images of two types of current collectors can be seen in figure 2.12. Examples with the use of a porous foam current collectors can be seen both in chapter 4.1 with the $LiMn_2O_4$ cathode and with SnO_2 nanowires in chapter 5.1.2.

2.6 Electrochemical methods of characterisation

Many electroanalytical techniques are available to evaluate material candidates for new batteries, as well as improving existing battery systems. The most used electrochemical methods in this thesis are described in the following chapters.

2.6.1 Cyclic voltammetry

Cyclic voltammetry involves the imposition of a triangular waveform as the potential on the working electrode, with the simultaneous measurement of the current. This triangular waveform, typical of cyclic voltammetry, can be seen in figure 2.13.[50] Cyclic voltammetry, or linear sweep voltammetry as it is often called, is probably one of the more versatile techniques available to the electrochemist. The potential sweep rate, υ, is the rate of change of the potential with time (dV/dt), and changes sign at each reversal point.

As the applied voltage approaches that of the reversible potential for the electrode process, a small current flows, the magnitude of which increases rapidly, but later becomes limited at a potential slightly beyond the standard potential by the sub-

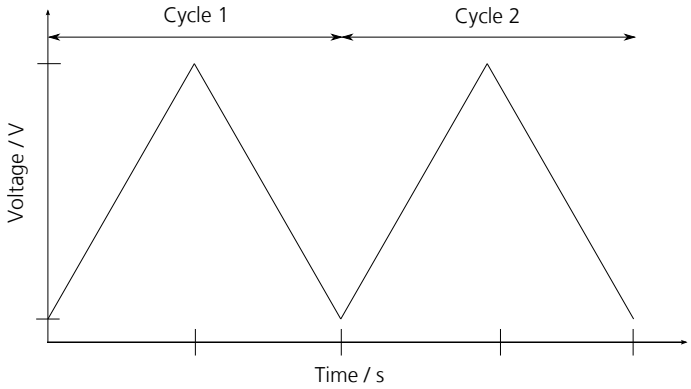

Figure 2.13: Cyclic voltammetry potential waveform with a potential sweep rate $|dV/dt|$.

sequent depletion of reactants. This depletion of reactants establishes concentration profiles (figure 2.14(a)) which spread out into the solution. As the concentration profiles extend into the solution, the rate of diffusion transport at the electrode surface decreases and with it the observed current. The current is thus seen to pass through a well-defined maximum (figure 2.14(b)).[8]

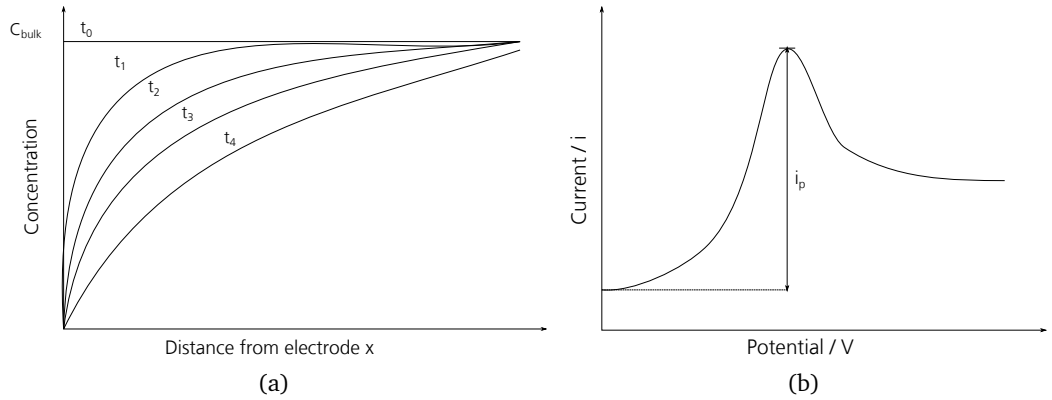

Figure 2.14: Schematics of cyclic voltammetry, (a) concentration profiles for the reduction of reactants in cyclic voltammetry and (b) cyclic voltammetry peak current for reversible reduction.

Cyclic voltammetry provides both qualitative and quantitative information of the electrode processes. A reversible, diffusion controlled reaction would give an approximately symmetrical pair of current peaks. However, a completely irreversible electrode process would produce only a single peak.[51] It is important to notice that the voltage and shape of the peak is sweep-rate dependent and need to be taken into consideration. In complex systems the correlation of peak to the related species or process can be somewhat complicated. However, cyclic voltammetry is considered to be a versatile, relative sensitive identification tool to help unravel the

electrochemical systems.[8]

2.6.2 Galvanostatic characterisation

Galvanostatic characterisation is often called rate capability determination, chronopotentiometry or the constant current method, and it is considered to be a very useful method to characterise the electrochemical performance of an electrode and its active material. It measures the amount of charge stored within an electrode under various experimental conditions over increasing cycle numbers. From this method the specific capacity, the voltage profiles, stability, life expectancy and load capability can be determined. A typical charge process is schematically described in figure 2.15.

The charge behaviour for a real battery cell starts with a constant current step. The current is being held at a certain value (blue curve). The specific charge current is often expressed as mA/g, with the mass being relative to the amount of active material. Alternatively, the specific current is defined in terms of the C-rate, where 1 C is defined as the theoretical amount of charge which can be extracted from a given material within one hour. As the current is being held constant, the voltage (green curve) increases.

The voltage rises until a cut-off potential is reached. The cut-off potentials are defined from the materials redox peak range to avoid side reactions like electrolyte decomposition. However, the battery is after the constant current step not completely charged. Usually the battery is only to 75-80 % charged (yellow curve), and the lithium-ions are only to be found on the surface on the material. The ions need a certain time to diffuse into the bulk of the material, hence there is a second charge step, where the voltage is being held constant (a potentiostatic step). The cut-off point with constant voltage is either reached after a certain time or after the current has reached a certain fraction of its charging value. At this point the battery is considered to be fully charged.

The ratio between the charge obtained during the intercalation and during the deintercalation processes is defined as the cycling coulombic efficiency and indicates the reversibility of the electrochemical process. Several experiments are possible with

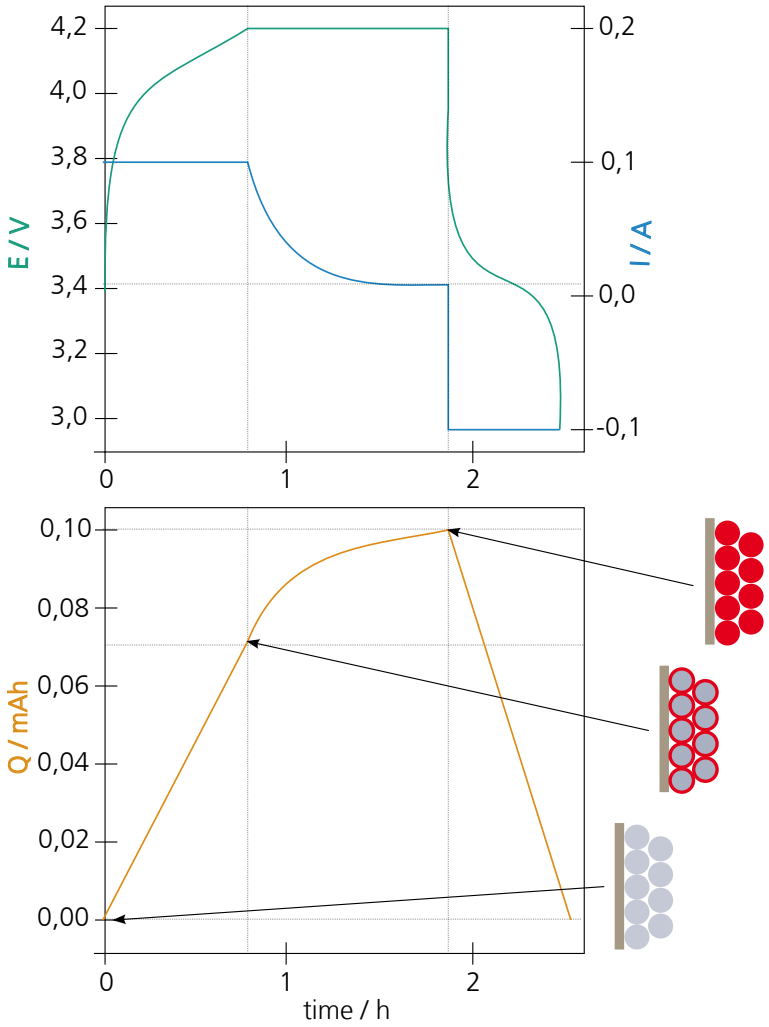

Figure 2.15: Charge behaviour with constant current measurement for a real battery, voltage, current and capacity as a function of time. Adapted from Möller[17].

constant current method. Either the current is held at a constant C-rate over several cycles and the battery's life time and stability is to be determined, or the C-rates can be varied, ranging from 0.1 C to 10 C for example. This method would give information about the cell's load capability and the kinetics of the active materials. The performance of the material will typically decrease as the C-rate increases.[52] At higher C-rates (10 C means charging/discharging in 6 minutes) the time needed for Li-ion diffusion is often not sufficient, and most battery materials do not show an adequate electrochemical performance.

Further details on the electrochemical methods used in this thesis can be found in *Electrochemical Methods* by A. Bard and L. Faulkner.[53]

Chapter 3

Experimental Setup

3.1 Preparation of materials

Depending on the type of material, the quality of it and the manufacturer, the materials used in this thesis have different routes to be chemically and electrochemically characterised. The anode materials are provided from project partners, leaving different preparation methods to turn the materials into electrodes. The Sn-based anode materials from the university of Cologne were either deposited on a copper foil or produced as self-supporting fibres, meaning the further preparation to electrode and to cell assembly was standard procedure. The quaternary chalcogenidometalate networks from Philipps-Universität Marburg were synthesised as crystals or fine powders and had to be further prepared. More details to the production of anode materials are given in chapter 3.1.3.

Most electrode materials are found in powder form before being advanced to electrodes. In a standard procedure this active material will be mixed with certain amounts of a conductive agent. Here conductive carbon black was used (Super P from TIMCAL), as well as a binder material (polyvinylidene fluoride (PVDF) from Kynar) and a solvent (*N*-Methyl-2-pyrrolidone (NMP) from Sigma Aldrich). The components are ground and mixed in a planetary micro mill from Fritsch, at a mixing speed of 300 rpm for 1 hour. The resulting slurry can either be doctor bladed onto a metallic foil (chapter 3.1.2.2) or infiltrated into a metallic foam (chapter 3.1.2.4). A typical composition of this electrode slurry can be found in table 3.1, although the specific composition varies from anode to cathode material.

Table 3.1: A typical composition of electrode slurries.

Component	Material	Content
Active material	e.g. $LiMn_2O_4$	70 %
Conductive agent	Super P	24 %
Binder	PVDF	6 %
Solvent	NMP	300 %

Part of the preparation of the $LiMn_2O_4$-cathode follows the above description, and the rest of the synthesis and following coating steps are described in chapter 3.1.1.

3.1.1 Synthesis of the cathode material

The cathode $LiMn_2O_4$-material was synthesised through a sol-gel process, which is advantageous due to its low cost, ease of preparation and it is a low temperature technique which give high control over the product's resulting morphology. The needed precursors were mixed and heated using an oil-bath until the boiling point was reached. A reflux condenser was used for 30 minutes, subsequently the solution was attached to a Büchi rotating evaporator with vacuum system. The sol-gel would boil in reduced pressure for about 60 minutes, then the pressure was further reduced to 30-40 mbar, where the refluxing continued for another hour. From the resulting concentrated solution, a solids content was to be determined before the solids content was diluted to 5 % with ethanol and 1,5-pentanediol as solvents. Table 3.2 shows the used precursors and the corresponding ratios.

Table 3.2: Precursors used for a standard $LiMn_2O_4$-sol.

Precursors	Chemical formula	Amount / mol
Lithium acetylacetonate	$C_5H_7LiO_2$	0,044
Manganese(II) acetate tetrahydrate	$C_4H_6MnO_4{\cdot}4H_2O$	0,092
2-(2-Methoxyethoxy)acetic acid	$C_5H_{10}O_4$	0,491
Ethanol	C_2H_6O	1,228

By the means of inductively coupled plasma optical emission spectroscopy (ICP-OES), the stoichiometric composition of the sol-gel could be determined. ICP-OES is further described in chapter 3.2.4. Thermogravimetrical analysis (TG/DTA) was used to determine the different processes upon thermal treatment. The spinel formation as well as the loss of organic compounds could be confirmed at certain temperatures.

Chapter 3.2.3 contains more information about the thermogravimetrical analysis. The pyrolysis behaviour of the precursor sol was also characterised using the X-ray diffraction method (XRD) (chapter 3.2.2), however, not as a solution, but after a thermal treatment to achieve the needed powder for XRD. (The exact thermal procedure is described in section 3.1.2.1) The phase purity and crystal structure of the cathode material could be determined from XRD-analysis.

3.1.2 Coating methods

Depending on the aim of the electrode (homogenous, ease of preparation or amount of active material) as well as the choice of current collector, several different coating methods have been examined. For the sol-gel solutions coated onto metallic foams as current collector, a dip coating method (chapter 3.1.2.1) was chosen due to good morphology and thickness control of the layers. However, in later stages more active material per sample was preferred to increase the volumetric capacity, and other coating methods like electrophoretic deposition and infiltration of a viscous slurry were investigated (chapter 3.1.2.3) and chapter 3.1.2.4 respectively). For cathode materials to be coated onto a flexible metallic foil, the standard doctor blading method was chosen, where first a slurry as described in chapter 3.1 was made.

3.1.2.1 Dip-coating

Dip coating was primarily used for cathodes in the sol-gel form to be coated on metallic foam current collectors. To improve the adhesion to the foams, they first had to undergo a thermal treatment where the oxide of the metal is formed. Nickel metal foam from Inco was mainly used, and when heated to 600 °C a nickel-oxide layer was formed. This layer was more porous than pure nickel and supplied the coated cathode material with better adhesion to the substrate.

The coating itself was performed in a cleanroom to avoid the influence of particulates. The sol-gel was transferred into a beaker, and the fitted and thermally treated foams were fastened to the coating construction. The dip speed, acceleration, holding time and retracting speed could all be programmed, making it a half automatic process. Typical dip-coating parameters can be seen in table 3.3.
After dip coating the samples were left 30 minutes to evaporate, followed by

Table 3.3: Parameters used for dip coating.

Coating temperature	R. T.
Input speed	500 mm/min
Holding time	60 s
Output speed	120 mm/min

10 minutes at 125 °C to further remove organic rests. However, a calcination process was still necessary to complete the transition to $LiMn_2O_4$ spinel. The parameters of the calcination process can be seen in figure 3.1.

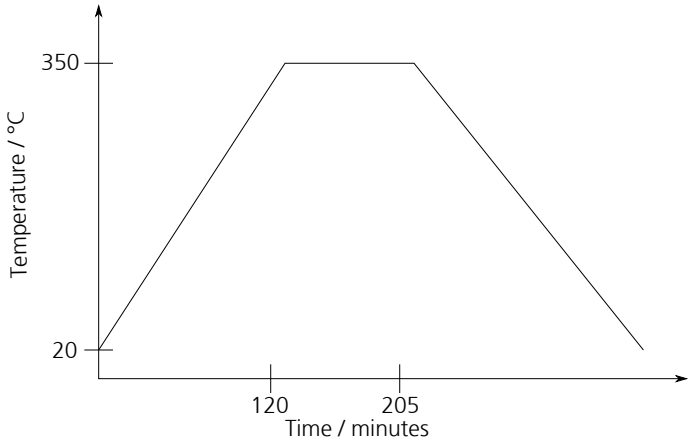

Figure 3.1: The thermal treatment procedure for formation of cathode $LiMn_2O_4$-spinels.

The coated samples were slowly heated (2.7 K/min) to 350 °C, and this temperature was held for 85 minutes. The calcination temperature was chosen as a result of TG-analysis from the sol-gels. The foam substrates were weighed before and after coating to determine the active mass of the dip coating. Upon the calcination process the coated foam samples could be directly assembled as electrochemical cells. The detailed description to cell assembly of these samples is found in chapter 3.3.1.

3.1.2.2 Doctor-blading

Doctor-blading was used for cathode materials in powder form, where the powder was made into a slurry and coated onto metallic foils via doctor-blading. This method allows for the formation of thin films with a well-defined thickness. A sharp blade is placed at a fixed distance from the substrate surface that is to be coated. Here the distance was fixed at 100 μm. The slurry is then placed in front of the blade that is

then moved linearly across the substrate leaving a thin wet film after the blade.[54] An Erichsen Coatmaster 510 was used, where metallic foils of size 10 x 30 cm^2 could be fixed with the use of vacuum. After coating, the foils were dried at 80 °C for 2 hours in vacuum. With the right slurry viscosity and coating parameters, an uniform coating without cracks and faults was made. The thickness after drying was reduced to 20 - 40 μm and measured with a Keyence CMOS gauge sensor. This coating method was used for the electrode materials from the University of Marburg as well as certain $LiMn_2O_4$-cathode materials to be compared with those on foam substrates. Standard metallic foils were used, and the mass of a substrate disc without coating was determined in order to calculate the active mass of the electrode.

3.1.2.3 Electrophoretic deposition

Electrophoretic deposition (EPD) is a colloidal process which requires short formation time, simple apparatus and little restrictions of the shape of substrate. EPD offers easy control of the thickness and morphology of a deposited film through control of the deposition time, applied potential and distance to electrode. In electrophoretic deposition, charged powder particles, dispersed or suspended in a liquid medium are attracted and deposited onto a conductive substrate of opposite charge on application of a DC electric field.[55] A schematic drawing of the electrophoretic deposition can be seen in figure 3.2.

Due to occurring edge effects from dip coating, electrophoretic deposition was investigated, to compare the thickness and layer controllability. First the sol-gel precursors where calcinated, as seen in figure 3.1 to obtain a $LiMn_2O_4$-powder. The resulting powder was mixed with carbon black, binder and acetone as described by J. Hamagami et al.[57]. The solution was stirred for 20 minutes, then placed in an ultrasonic bath for another 20 minutes to ensure the complete dispersion of the $LiMn_2O_4$ particles. The composition of this EPD solution can be found in table 3.4.

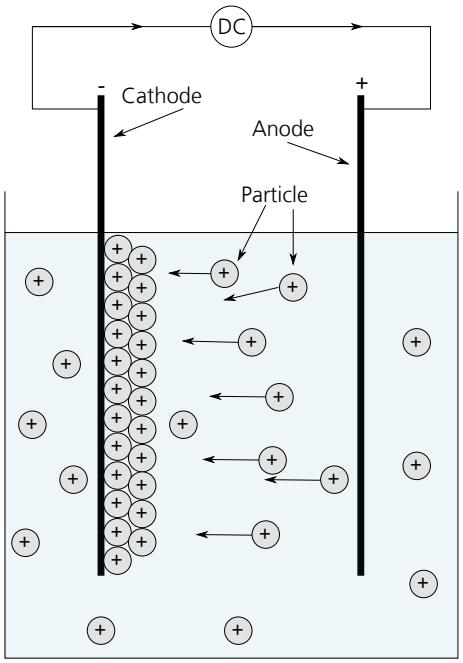

Figure 3.2: Schematic drawing of electrophoretic deposition, adapted from Sarkar et al.[56]

Table 3.4: Composition of EPD solution.

Precursors	Amount
$LiMn_2O_4$	500 mg
Carbon black	10 mg
Binder (PVDF)	24 mg
Iodine	20 mg
Acetone	50 ml

A small amount of iodine was added to produce charged particles in the solution.[58] A fitted foam substrate as working electrode was fastened to the EPD setup, where the applied voltage was given from a Heinzinger TN power supply and set to 100 V. The deposition time varied between 2 - 15 minutes. A stainless steel plate was used as the counter electrode and the electrode spacing was held constant for all experiments. After drying at room temperature, the electrodes were further treated at 80 °C for 2 hours to remove leftover organics. The foam substrates were weighed before and after coating, to determine the mass of $LiMn_2O_4$.

3.1.2.4 Infiltration

Another aim of the coating of metal foams was to completely fill the pores with active material to get the highest possible volumetric efficiency. With dip coating or

electrophoretic deposition this proved to be a extensive process, as the steps had to be repeated to achieve the wanted filling grade. Hence, infiltration with a viscous $LiMn_2O_4$-slurry was investigated. A standard slurry, as described in table 3.1, was made, although the amount of solvent (NMP) varied, to reduce the viscosity. A silicon template was used to hold the fitted foam in place, and the pressure infiltration setup was assembled. The $LiMn_2O_4$ slurry was smeared onto the foam and with the use of air pressure, the slurry was infiltrated into the foam pores. This step was repeated on the other side of the foam to ensure filling on both sides, and the sample was left to dry. First at room temperature, then at 80 °C for 3 hours to remove the remaining solvent in the slurry.

3.1.3 Synthesis of the anode materials

Sn-containing anodes

Different Sn-based anode materials were fabricated at the University of Cologne, in the research group of Professor S. Mathur. The following synthesis description is based on the description from the colleagues at the University of Cologne where the synthesis took place. The SnO_2 nanowires deposited on copper foil were fabricated by low pressure chemical vapour deposition (CVD). The $Sn(OtBu)_4$-precursor was heated to sublimation point, and once in the gas phase it would decompose directly on the substrate. Here a copper substrate was used, which was heated to 700 °C. Normally the growth of SnO_2 would need gold particles as a catalyst, but here it was not necessary as the Cu on the surface of the metallic foil melted and gave the same function. Normally anode CVD was performed on substrates of 1x1 cm^2 and these were later punched into the wanted electrode size and assembled as a half cell as described in section 3.3.1. The SnO_2 deposited on a nickel foam current collector was also fabricated with the same CVD parameters. Further description of the synthesis of SnO_2 anodes can be found in the PhD thesis of R. Fiz, University of Cologne[59].

The Sn-containing carbon nanofibres were produced via the electrospinning route. A precursor solution containing tin(IV)ethoxide ($Sn(IV)(OEt)_4$) and polyvinylpyrrolidone (PVP) was solved in a 1:8 mixture of acetic acid and ethanol. The precursor solution was mixed under vigorous stirring at room temperature for 3 hours. The obtained viscous sol was transferred into a syringe feeding 20 μl/min to a metallic

needle with an inner diameter of 0,8 mm, which was set to a potential of 20 kV for sol-gel electrospinning. In a distance of 8 cm a grounded aluminum was placed to collect the generated nanofibers as non-woven and the alkoxide precursor got hydrolysed at ambient conditions for 12 hours. The nanofibers could easily be peeled off from the aluminum foil after drying in vacuum over night and transferred to a flat substrate for the calcination process. The purpose of calcination was the carbonisation of PVP and the carbothermal reduction of $Sn(OR)_4$. The fibers were heated in nitrogen atmosphere with a heating ramp of 10 °C/min up to 650 °C for 2,5 hours and then the samples were allowed to cool down to room temperature without external cooling. The standard composition for the precursor solution can be seen in table 3.5. To generate Sn-CNF with varying Sn:C ratio, different amounts of $Sn(IV)(OEt)_4$ (0,17 mol/l, 0,22 mol/l and 0,33 mol/l) were solved in the precursor solution while keeping the amount of PVP as carbon source constant at 33,3 g/l. Further details to the synthesis of Sn-CNF can be found in the PhD thesis of R. von Hagen, University of Cologne[60].

Table 3.5: Composition of standard Sn-CNF precursor solution.

Component	Amount
$Sn(IV)(OEt)_4$	0,33 mol/l
PVP	33,3 g/l
Acetic acid and ethanol	1:8

The resulting self-standing fiber electrodes were punched into the fitting electrode size and assembled as a half cell with Cu-foil as current collector (cell assembly described in chapter 3.3.1).

Synthesis of the lithium chalcogenidometalates

The new anode group of quaternary chalcogenidometalates was synthesised at Philipps-Universität Marburg in the research group of Professor S. Dehnen and the following synthesis description is based on their work. For the synthesis of $Li_4MnSn_2Se_7$ a stoichiometric mixture of 0.686 g (15.36 mmol) of Li_2S, 0.877 g (7.39 mmol) of Sn, 2.335 g (29.57 mmol) of Se, and 0.102 g (1.85 mmol) of Mn were mixed and melted together in flux conditions in a furnace with a definite temperature program: heating up to 650 °C, with a heating rate of 18 °C/h, keeping for 650 °C for 24 hours, cooling down to room temperature, with a rate of 6 °C/h.The product

was obtained as single crystalline phase beside ternary Li/Sn/Se phases and excess of selenium. To obtain the phase pure product, the mixture was washed with water to remove the soluble Li/Sn/Se phases and afterwards the selenium was removed via sublimation at 500 °C and reduced pressure of 10^{-6} Pa.

The synthesis of $Li_4MnGe_2S_7$ was similar; a stoichiometric mixture of 0.706 g (15.36 mmol) of Li_2S, 1.114 g (15.36 mmol) of Ge, 1.969 g (61.41 mmol) of S, and 0.211 g (3.84 mmol) of Mn were mixed and melted together in flux conditions in a furnace with the same temperature program as above. The product was obtained as single crystalline phase beside ternary Li/Ge/S phases and excess of sulphur. To obtain the phase pure product, the mixture was washed with water to remove the soluble Li/Ge/S phases and afterwards the sulphur was removed via sublimation at 320 °C and reduced pressure of 10^{-6} Pa. Both syntheses were performed with strong exclusion of air and external moisture (argon atmosphere at a high-vacuum, double-manifold Schlenk line or nitrogen atmosphere in a glove box).

3.2 Methods of characterisation

3.2.1 Electron microscopy

One of the most applied methods for structural characterisation is electron microscopy. This technique allows unlimited possibilities to examine a sample beyond what is possible with the human eye. The image formation can be controlled so that certain structural details of a sample are accentuated. Structural and chemical information are achieved through the electron diffraction pattern in scanning or transmission electron microscopy.[61] The following chapters describe the apparatus used for this thesis.

3.2.1.1 Scanning electron microscopy

In scanning electron microscopy (SEM) the sample surface is scanned with the use of a primary electron beam. Depending on the sample material and the set accelerating voltage, different excitation volumes occur, and can be seen in figure 3.3.

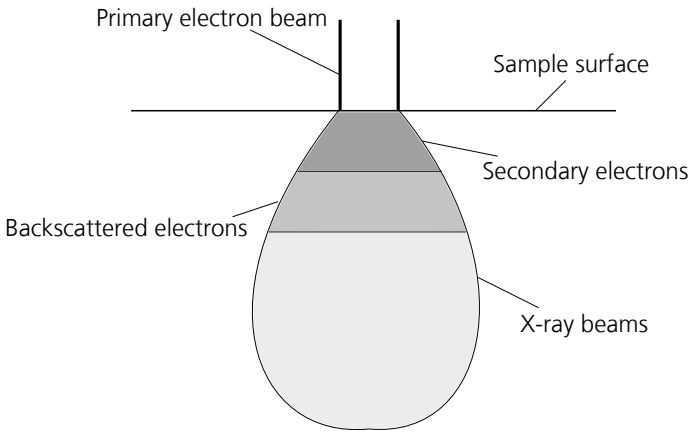

Figure 3.3: Excitation volume, where secondary, backscattered electrons and X-ray beams origin, adapted from Goodhew et al.[61].

Depending on the penetration depth of the electrons, different secondary products are created. For the imaging, the secondary and backscattered electrons are mostly used. The secondary electrons occur through inelastic scattering of the primary electrons at the atom nucleus or at the electrons in the atomic shell.[61, 62] In this work, the in-lens and SE2-detector were mostly used, when not otherwise stated. All imaging was performed on a Supra Zeiss 25 in a vacuum of about 10^{-4} Pa. The cross section samples were prepared with a cross section polisher (CSP) using an argon via Argon beam milling.

3.2.1.2 Energy dispersive X-ray spectroscopy

The Supra Zeiss 25 is also equipped with an energy dispersive X-ray spectrometer (EDS), where the characteristic X-ray beams seen in figure 3.3 come to use. When the primary electron beam hits the sample surface, electrons will be expelled out of the atomic shell, leaving a hole to be filled by electrons from higher shells and thus providing characteristic X-ray beams for every element.

There are several EDS methods, one being spectrum imaging where the visible SEM area is scanned and the X-rays originating here are detected. Line scan where the distribution of the elements along a line is investigated, as well as mapping of the element distribution are available techniques.

3.2.1.3 Transition electron microscopy

In a transmission electron microscope (TEM), the amount of the electron beam that is transmitted through the sample is investigated. As a comparison to SEM where only the backscattered or secondary electrons are examined. This, however, limits the sample preparation of TEM, the samples need to be very thin, and the thinning processes can affect the samples, both in structure and chemistry.[63] Nevertheless, TEMs are capable of imaging at a significantly higher resolution than light microscopes and SEM, and finer details are made visible.

The transmission electron microscope used in this work was a JEOL JEM 2011, with 200 kV acceleration voltage and equipped with both EDS and scanning transmission electron microscope (STEM), which combines the advantages of both TEM and SEM. The thinning process was performed with a focused-ion beam (FIB) to create a thin lamellar sample.

3.2.2 X-ray diffraction

The X-ray diffraction method (XRD) was mainly used to examine the crystallinity and phase purity of the electrode materials. The X-ray waves interact with the electrons of the atoms of a crystal, resulting in a diffraction pattern. When the Bragg law is fulfilled (equation 3.1), a constructive interference occurs which is recorded at the detector. The diffraction pattern of a crystal includes both the positions and intensities of the diffraction effects and can be seen as the fingerprint of the substance, providing a rapid identification. Analysis of the positions of the diffraction effects leads immediately to a knowledge of the size, shape and orientation of the unit cell.[62, 64]

$$n\lambda = 2d \cdot \sin\theta \tag{3.1}$$

Equation 3.1 describes the Bragg law, where n is an integer, the order of the reflection, λ is the wavelength of the X-rays, d the interplanar spacing between successive atomic planes in the crystal, and θ is the angle between the atomic plane and both the incident and reflected beams. The majority of the XRD analyses were performed on a Philips PW 1710 with Cu-rays in a 2θ-range from 10° to 80° with a scan rate of 0.02 °/min. However, grazing incident diffraction (GID) to examine thin films was

only possible with the setup of a Siemens D 5005. The peak indication and some data treatment were performed with the EVA XRD Software from Bruker.

3.2.3 Thermoanalysis

In thermal analysis particular physical and chemical material properties are measured as a function of the temperature. The sol-gel process and some substrates were examined with thermogravimetry and differential thermal analysis. In thermal gravimetric analysis (TG) the sample's change in weight (due to oxidation and pyrolysis effects) during a given temperature-time program at a defined atmosphere is determined. For a differential thermal analysis (DTA), the temperature difference between the sample and a reference specimen is measured. The temperature of the sample and reference remain the same until a thermodynamic process occurs (like melting, decomposition or crystal structure changes). If the sample's temperature rise increases, it is an exothermic process, and opposite, an endothermic process if the temperate rise decreases. [65, 66] With both techniques the reactions and transformations of the samples are indicated, this also includes the spinel formation of $LiMn_2O_4$.

All samples in this work were measured on a Netzsch STA 409 C Jupiter in synthetic air atmosphere in the range from room temperature to 1000 °C with a heating rate of 10 K/min. The aim of thermoanalysis was either to determine the temperature for spinel formation or to examine the decomposition of organic solvents.

3.2.4 Inductively coupled plasma optical emission spectrometry

Inductively coupled plasma optical emission spectrometry (ICP-OES) utilises a plasma, an ionized gas, several thousand kelvin hot. The energy used to provide this plasma, is electromagnetically made with an induction coil, hence the name inductively coupled plasma. The sample to be examined is brought into the plasma, and at such high temperatures all chemical bonds dissociate, meaning that the analysis is independent from the chemical bonding of the sample. In the plasma, the atoms and ions are stimulated to light emission, and the generated wavelengths can be used as identification of the elements. The intensity of the emissions determines the concentration of the elements. This technique is advantageous due to the simultaneous emission from all elements present in the sample, giving a shorter measurement time.[67]

The ICP-OES shown in this work were all measured on a Vista-PRO Simultaneous ICP-OES with an argon plasma source, with temperatures reaching 6000 - 10000 °C. The samples were diluted with water and hydrochloric acid before measurement.

3.3 Electrochemical characterisation

3.3.1 Electrode fabrication and cell assembly

For the electrodes that have been doctor-bladed onto a metallic foil (chapter 3.1.2.2), the next steps include punching and pressing of circular electrodes to be built as electrochemical cells. The electrodes were punched to a 11 mm diameter and subsequently pressed with 87 kN/cm^2 to ensure a homogeneous surface, to reduce the diffusion paths, improve the particle-particle contact and to increase the volumetric energy density. The resulting disk electrodes were introduced to a MBraun glove box with inert atmosphere, and once again dried to remove remaining moisture. In the glove box the electrodes were dried in vacuum at 80 °C for 5 hours.

The cell assembly followed in the glove box in argon atmosphere, with H_2O and O_2 values below 1 ppm. Depending on the type of electrode material and substrate, different types of electrochemical cells were chosen. For electrodes coated on metallic foils a Swagelok® -cell was chosen (figure 3.4(a)) due to the improved accurateness and the optimised electrode size. For the larger electrodes on foams, the 3-electrode cell (figure 3.4(b)) was chosen, where ease of preparation and sufficient electrolyte amount played an important role. However, the 3-electrode cell has not been proven to be completely air-tight, thus it should not be used for very long measurements when it can be avoided.

For the majority of the electrochemical measurements a half cell was build, meaning that only the working electrode was to be examined, and the counter and reference electrode consisted of metallic lithium. When not otherwise specified, the electrolyte used consisted of $LiClO_4$ in 1:1 EC/EMC, known to be more compatible with the $LiMn_2O_4$ spinel cathode material[25]. For the cell showed in figure 3.4(b) a separator is not needed, for a Swagelok® -cell two layers of separators were used. First, a commercial Celgard 2325, to prevent the growth of dendrite from the metallic lithium

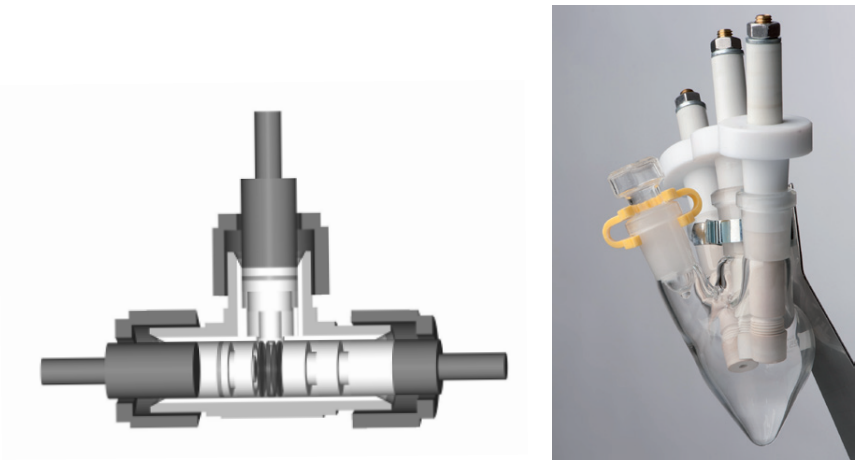

(a) (b)

Figure 3.4: Different cell types. a) The T-shaped Swagelok®-cell, b) a typical 3-electrode electrochemical cell.

to reach the working electrode. The Celgard 2325 is a 25 μm thick microporous trilayer membrane consisting of polypropylene (PP) and polyethylene (PE) in the order PP/PE/PP[44], the function of this trilayer membrane is to prevent thermal runaway as described in chapter 2.5.2. A second non-woven separator from Freudenberg ensures the passage of ions and the necessary pore volume storage of excess electrolyte quantities.

3.3.2 Cyclic voltammetry

The cyclic voltammetry experiments described in chapter 2.6.1 were all performed on a multi-channel Solartron 1400 potentiostat. Most experiments were conducted with a potential sweep rate of 0.1 mV/s, when not otherwise stated. 3-5 cycles were recorded, for the anode materials usually in the range between 3.0 - 0.01 V vs. Li/Li^+, and for the cathode material in the range 3.0 - 4.5 V vs. Li/Li^+.

3.3.3 Galvanostatic measurements

The galvanostatic or constant current measurements were performed on the battery and cell tester Maccor 4000. The potential range for cathode and anode material was the same as for the cyclic voltammetry, and the general program setup can be seen in chapter 2.6.2. The C-rate is given as an input before each measurement. According to the *Electrochemical Dictionary*[52] the discharge rate is expressed in amperes or

in C rate, which is expressed as a multiple of the rated capacity in ampere-hours. For standard, state-of-the-art materials, the C-rate is computed from the theoretical capacity as that is often close to the practical capacity. For the new materials, with unknown theoretical capacity and more degradation than the established materials, the C-rate was per definition found from the fifth discharge cycle. However, a discharge current of 100 mA/g was used as standard current density for the initial measurements.

Chapter 4

Cathode coating on porous current collectors

4.1 $LiMn_2O_4$ on nickel foam

$LiMn_2O_4$ has been the main focus as a cathode material in this thesis. As mentioned in chapter 2.4, the material was chosen due to the lesser toxicity, abundant material source and a high specific capacity of 148 mAh/g.[4, 27] The $LiMn_2O_4$ material system is a relatively well studied cathode system, although in combination with a porous current collector new possibilities appear. A metal foam substrate have advantages such as high porosity, improved mechanical strength and adhesion as well as increased electrical conductivity.[48, 49] The combination of these two systems could improve the electrochemical properties of $LiMn_2O_4$ and at best give a superior high-rate specific capacity due to the high surface area of the current collector.

4.1.1 Structural characterisation

Choice of metallic foam as current collector

Several manufacturers provide commercially available metallic foams, the most common ones being nickel, aluminum or alloys of the two with chromium. A selection of foams was made and the description of the initial foam variety can be seen in table 4.1. These metallic foams were thermally treated at different temperatures to obtain a homogeneous oxide layer which is needed for the adhesion to the cathode material. Thermogravimetrical analysis in addition to X-ray diffraction and electrochemical

tests were executed to find the most suited current collector for the $LiMn_2O_4$ cathode material.

Table 4.1: The initial selection of metal foams.

Foam	Abbreviation	Foam composition	Manufacturer
Ni-foam	Ni	100 % Ni	Recemat and Inco
Ni-Cr-foam	NiCr	60 % Ni, 40 % Cr	Recemat
Ni-Cr-Al-foam	NiCrAl	45 % Ni, 40 % Cr, 5 % Al	Recemat
Al-foam	Al	100 % Al	m-pore
Al-Si-Mg-foam	AlSiMg	55 % Al, 40 % Si, 5 % Mg	m-pore

A simple electrochemical test was performed to examine the stability range of the foams. The foams were assembled in a 3-electrode cell as described in chapter 3.3.1 and a linear potential sweep was induced between 0.01 V and 4.8 V. When a foam was stable (in terms of electrochemical inactivity) in this potential window, it was considered an electrochemically suitable current collector. The results of the foam stability test can be seen in figure 4.1.

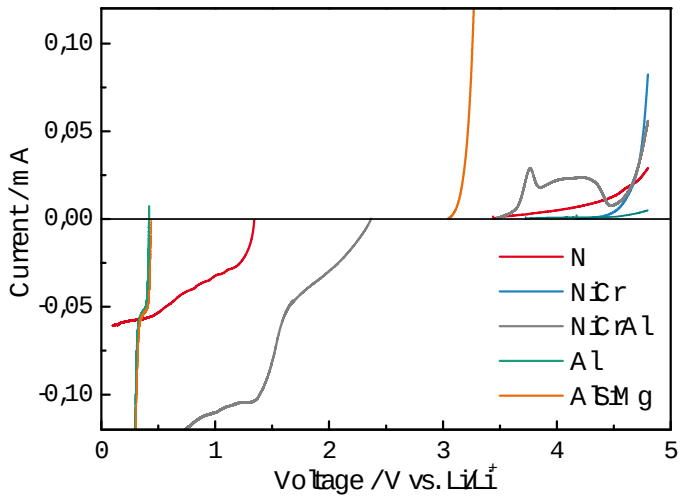

Figure 4.1: Electrochemical stability of the foam selection.

The stability test shows that most foams are stable in the potential window, and of more importance is the cathode range from 3.0 - 4.5 V. However, the AlSiMg-foam is further excluded from the selection as the foam is only stable within 0.2 - 3.3 V and would be unsuited as a current collector for a cathode material. Electrochemical measurements with a cathode on the AlSiMg-foam would lead to electrochemical

oxidation of the foam when cycling beyond 3.3 V and a complicated assignment of the redox processes occurring. The Al-foam is also unstable at a voltage below 0.2 V, but as the foams are wanted as a current collector for cathodes, this is not significant. The other foams (Ni, NiCr and NiCrAl) remain relatively stable in the wanted potential window.

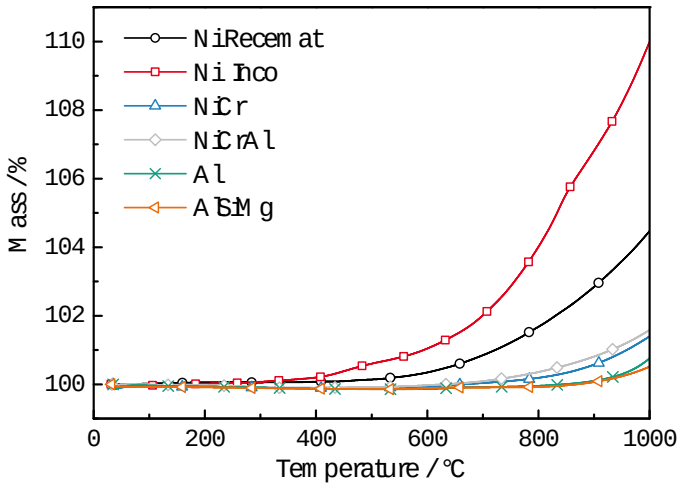

Figure 4.2: Thermogravimetrical analysis of the foam selection.

Figure 4.2 includes the TG analysis of the different metallic foams, where the oxidation process was examined. Apparently, both nickel foams (Inco and Recemat) form an oxide layer at a much lower temperature than the rest of the foams. The oxide layer on the metallic foams gives a higher porosity, higher surface area and hence a better adhesion to the cathode material (chapter 3.1.2.1). The nickel-chromium and aluminum foams oxidate first after reaching 750 °C which makes the process more ineffective in terms of energy consumption. The TG analysis clearly shows that the two nickel foams are better suited to obtain an oxide layer at a lower temperature. Furthermore, the nickel foam from Inco shows oxidation from 400 °C, giving it an advantage over the Recemat nickel foam.

Further analysis of the nickel-chromium foams led to the exclusion of these substrates as well. Ul-Hamid et al.[68, 69] describes the oxide formation for Ni-Cr and Ni-Cr-Al alloys, and several different oxide layers such as NiO, $NiCr_2O_4$, Cr_2O_3 and Al_2O_3 appear. Scanning electron microscopy combined with EDS also revealed a very inhomogeneous surface of the mixed nickel-chromium foams (figure 4.3).

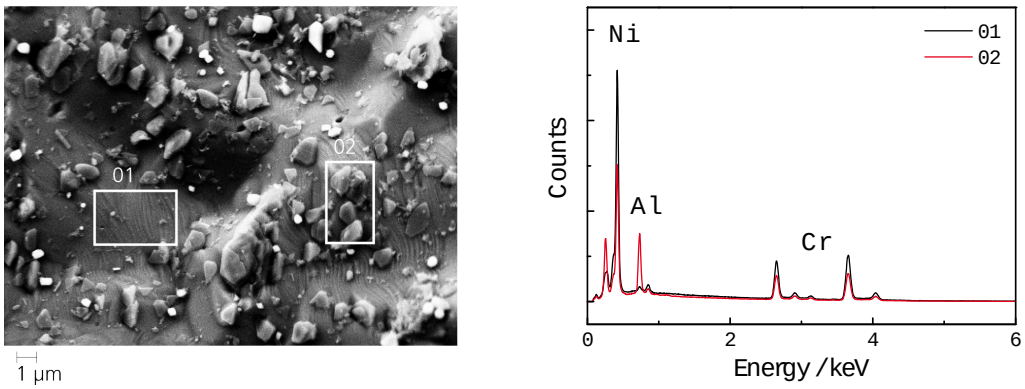

(a) (b)

Figure 4.3: EDS analysis of a Ni-Cr-Al foam. a) The scanned EDS areas b) the following EDS spectra.

As the EDS spectra in figure 4.3(b) show, the particles that are seen on the surface of the foam (figure 4.3(a)) are mainly aluminum, while the bulk material consists of nickel and chromium. The surface of the NiCrAl foam is very inhomogeneous and having such particles on the surface could be very disadvantageous as they can electrochemically react and cause unwanted side reactions when in contact with electrolyte or the cathode material. As only aluminum particles were detected, they will be stable in the electrolyte (As mentioned in chapter 2.5.3 aluminum foil is used as a standard current collector for cathode materials). However, an inhomogeneous surface is an unwanted feature for the substrate which leaves the nickel foams for further examination. Both the Recemat and the Inco nickel foam have an electrochemical stability up to 4.4 V vs. Li/Li^+ which is marginal considering the wanted cathode potential window is 3.0 - 4.5 V. However, the aluminum foam has a higher voltage range, but not a porous oxide layer which is needed for the improved adhesion of cathode material, and it was decided that the standard metallic foam substrate should be a nickel foam. The further selection was made on the basis of SEM images of the surface structure after thermal treatment at different temperatures (figure 4.4).

Figure 4.4 shows the different oxidation processes of the two foams at different stages. Generally, the set temperature was slowly reached and held for 85 minutes. The first row of images show the two foams as received. It can be concluded that the Recemat foam has a more inhomogeneous surface with several nanosized particles. With EDS

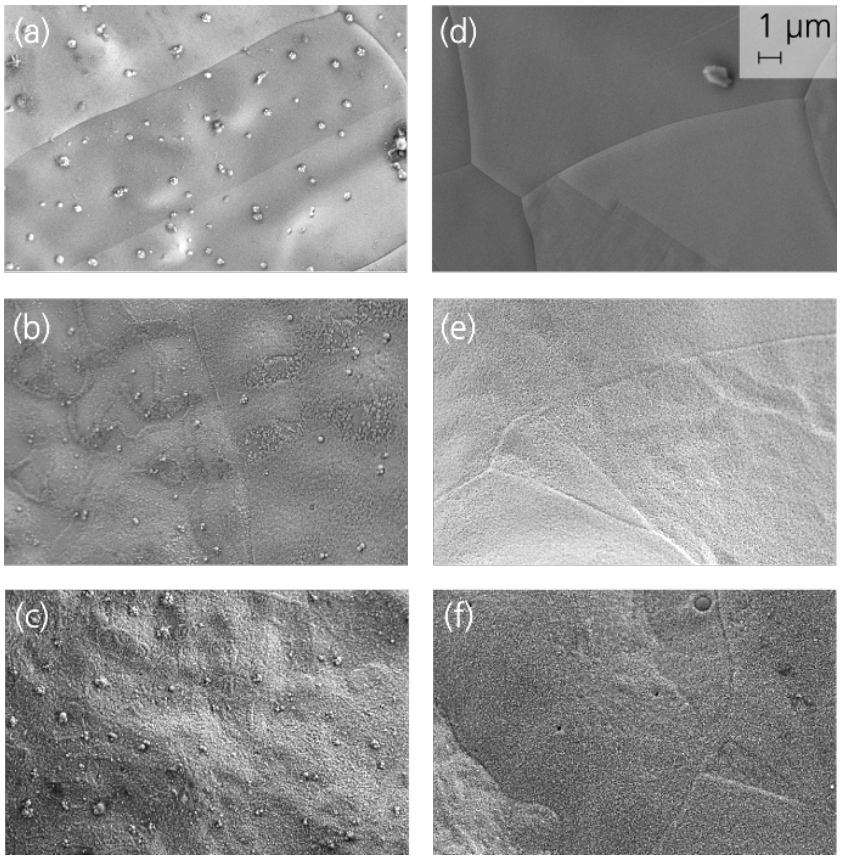

Figure 4.4: SEM images of the two nickel foams with varying thermal treatment temperatures. Recemat nickel a) untreated, b) at 470 °C, c) at 600 °C and Inco nickel d) untreated, e) at 470 °C, f) at 600 °C.

it was confirmed that these were nickel particles, however these irregularities at the surface played a major role in the oxidation. As can be seen in the further images, the oxidation at 470 °C is less complete for Recemat Ni, than for Inco Ni. 470 °C was chosen as a result of the TG analysis seen in figure 4.2, where the oxide formation for the nickel foams was proven to start at around 450 °C. However, the Recemat Inco requires a higher oxidation temperature. First at 600 °C some oxidation and the wanted porosity of the Recemat nickel was seen. This indicates a much higher energy demand for the thermal process of Recemat nickel foam, hence the Inco nickel foam was chosen as the standard porous current collector for the further work in this thesis. Figure 4.5 shows the XRD analysis of the thermal treatment of the Inco nickel foam to confirm that the layer seen with SEM actually consists of NiO as suggested.

In the XRD of the untreated nickel foam only peaks identifying nickel are seen. At 470 °C an oxide layer was detected with SEM, as seen in figure 4.4 and with EDS

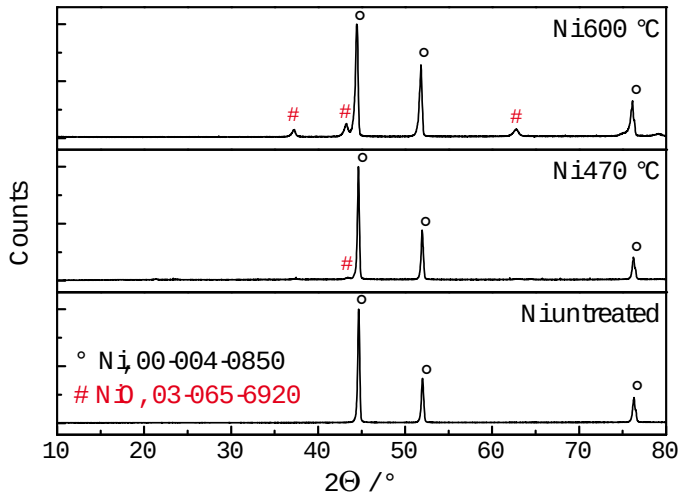

Figure 4.5: XRD of Inco nickel foam (untreated, 85 minutes at 470 °C and 85 minutes at 600 °C).

a higher oxygen content was detected, indicating that the layer is NiO. However, the XRD at 470 °C can only partly confirm a NiO layer. The peak at 43° indicates the NiO-phase, but it cannot be completely confirmed via XRD with just one peak. Nevertheless, at 600 °C all characteristic NiO peaks are detected. This discrepancy between the XRD and SEM analysis does not necessarily mean that there is no oxide layer formed at 470 °C, it is rather an indication that the formed layer is too thin for XRD measurement. Hence, as the layer can be seen in the SEM images and partly detected via EDS it is assumed that the NiO layer exists at 470 °C as well. As the standard temperature for oxide formation as a pre-treatment of the foams, 600 °C was chosen for the Inco nickel foams to ensure a complete layer.

Similar XRD measurements were performed with the Recemat nickel foam (seen in figure 4.6). Corresponding with the SEM images and the results of the Inco foam, an oxide layer on the Recemat nickel foam was first detected at 750 °C, again indicating that the layer seen in the SEM image at 600 °C was too thin to be properly characterised. Nevertheless, the oxide formation for Recemat Ni was once more confirmed to be happening at higher temperatures compared to Inco Ni. Further, two unknown peaks appeared at 75° and 78° which could not be allocated to any known substance. The indication of an impure oxide formation by Recemat confirmed the choice of Inco nickel foam over Recemat nickel foam.

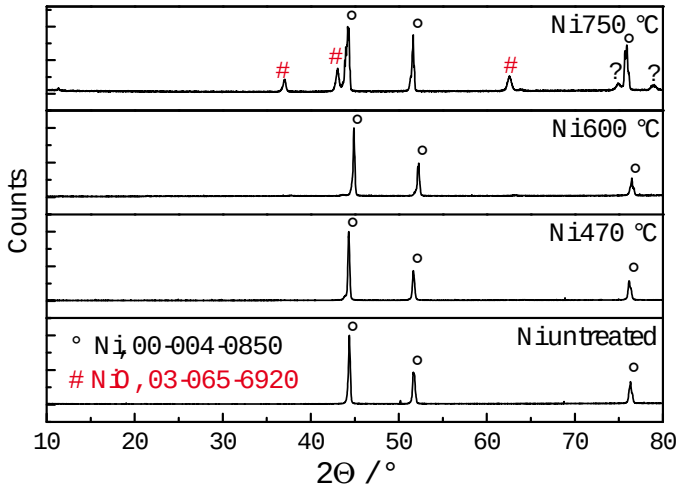

Figure 4.6: XRD of Recemat nickel foam (untreated, 85 minutes at 470 °C, 85 minutes at 600 °C and 85 minutes at 750 °C).

Development of a standard $LiMn_2O_4$ sol-gel

Before the right composition of the $LiMn_2O_4$ sol-gel could be found, a few nearly stoichiometrical solutions were obtained. Inductively coupled plasma analysis (ICP) proved that a 1:2 relation between the precursors, lithium acetylacetone and manganese(II) acetate tetrahydrate, gave the composition $LiMn_{1.97}O_4$, thus a 1:2.1 relation of the precursors was necessary to achieve the wanted $LiMn_2O_4$ composition. The amount of precursors and solvents used for the $LiMn_2O_4$ precursor solution was listed in table 3.2. After the composition of the precursor solution was confirmed via ICP, a thermogravimetrical analysis was performed in order to examine the spinel formation and the decomposition of the solvents.

Figure 4.7 displays the thermoanalysis of the $LiMn_2O_4$ precursor solution, executed as described in chapter 3.2.3. Both the black TG-curve and the red DTA-curve confirm that the spinel formation (also confirmed from the XRD in figure 4.10) as well as the solvent decomposition were completed at about 350 °C. The first endothermic DTA peak can be attributed to the evaporation of the solvents, here ethanol and 1.5-pentanediol. The notable weight loss in the TG curve is due to the decomposition of the inorganic and the organic constituents of the precursor followed by crystallisation of the $LiMn_2O_4$ phase. The exothermic DTA-peak at 350 °C is also attributed to pyrolysis of the solvents. At higher temperatures (above 370 °C) the TG curve becomes flat and no peaks are seen in the DTA curve, indicating that no phase transformation

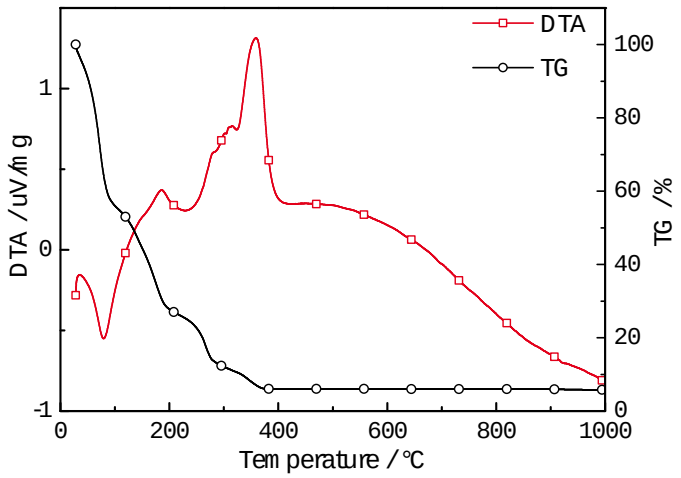

Figure 4.7: A thermoanalysis of standard $LiMn_2O_4$ precursor solution with DTA on the left axis and TG on the right axis.

occurs, and that any further heating makes the sample more crystalline.[70] The total weight loss in the TG curve also confirms the calculated solids content of 5 %. This information was used to optimise the calcination process (figure 3.1) where the coated precursor solution is thermally treated to obtain $LiMn_2O_4$ spinel.

After confirmation of stoichiometry via ICP and spinel formation via TG/DTA, the sol-gel could be used for coating. As described in chapter 3.1.2.1, thermally treated and fitted nickel foams were dip coated with the $LiMn_2O_4$ precursor solution. After calcination the samples could be examined with SEM, EDS, XRD and electrochemically measured. The average loading of cathode material with the dip-coating method was 15 - 20 mg per sample (approximately 1 cm^2). Figure 4.8 displays the scanning electron images of a $LiMn_2O_4$ coated nickel foam.

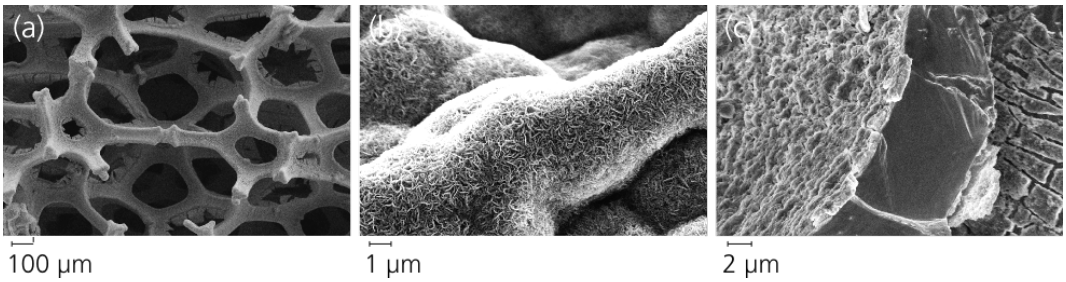

Figure 4.8: Scanning electron images of a $LiMn_2O_4$ coated Ni foam.

Dip coating is a versatile technique where the coating can be partly controlled by

varying the solids content of the precursor solution and coating parameters such as retracting speed and acceleration. However, the final result of the coating depends just as much on the following thermal treatment. Figure 4.8 shows three different SEM images of the $LiMn_2O_4$ coated foam. On the left side, an overview of the foam is seen. The pore edges are often partly coated and smaller pores can be completely filled. Figure 4.8 (b) shows the structure of the $LiMn_2O_4$ coating on a microscopic scale, where a homogeneous, porous surface is detected. The right image displays a cross section of the coated foam, prepared by dipping the foam in liquid nitrogen and breaking of a sample to be examined with SEM. The bulk area of nickel can be seen as the darker part of the cross section, with a porous coating. Several cracks can also be seen in figure 4.8 (c), although it is not certain if they have originated due to strain from preparation method (liquid N_2 and breaking) or from the coating and thermal treatment itself.

EDS analysis was also performed on the cathode coated nickel foam, and elements such as Ni, Mn, O and C were detected. Carbon and oxygen are always detected with the standard EDS method as the sample holder contains these elements as well. Lithium is a too light element to be detected by EDS, leaving the quantitative analysis of manganese and nickel. The bulk area seen in figure 4.8 (c) was detected as nickel, and the coating contained manganese. However, an analysis confirming spinel $LiMn_2O_4$ is not possible with EDS, although an indication of $LiMn_2O_4$ is confirmed. Further examination followed with the use of X-ray diffraction and transmission electron microscopy.

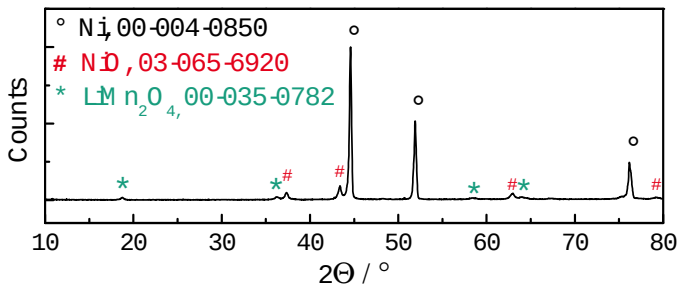

Figure 4.9: XRD of a $LiMn_2O_4$ coated nickel foam.

The XRD analysis of a coated nickel foam can be seen in figure 4.9, and at a first glance it does not differ much from the XRD of the thermally treated nickel foam

(figure 4.5). The thermally treated nickel substrate with nickel oxide is dominating the XRD-spectra as the thickness of the bulk material outbalances the coating, and the high intensity of the Ni/NiO peaks is absorbing the signals from the $LiMn_2O_4$ spinel. Only when the peaks are magnified can a partial spectrum of $LiMn_2O_4$ be detected. The star-symbols in figure 4.9 represent each detected $LiMn_2O_4$ peak, although several characteristic peaks cannot be found. The $LiMn_2O_4$ spinel can only with difficulty be confirmed directly from the coated nickel foams, as the coating is presumably too thin and the Ni peaks are too dominating.

It was decided to confirm the spinel from the precursor solution directly, and not after coating on the nickel. The standard sol-gel solution described in chapter 3.1.1 underwent the same thermal treatment as the $LiMn_2O_4$ after the dip-coating (heated to 350 °C for 85 minutes to complete spinel transformation), and the resulting powder was examined with XRD. The resulting spectrum can be seen in figure 4.10.

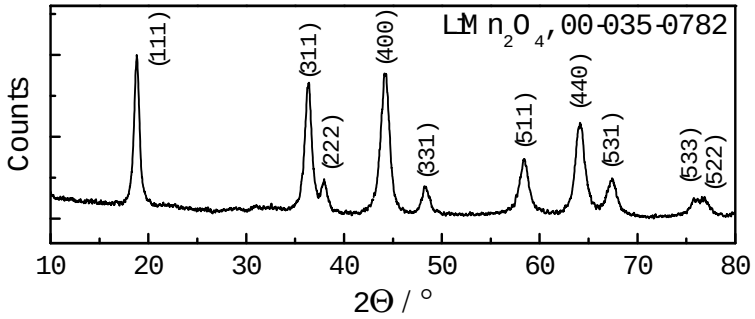

Figure 4.10: XRD of a the dried $LiMn_2O_4$ sol-gel.

The characteristic peaks were compared with those of $LiMn_2O_4$ using the XRD software Diffrac^{Plus} EVA from Bruker. Peaks with the *hkl* value of (1 1 1), (3 1 1), (2 2 2), (4 0 0), (3 3 1), (5 1 1), (4 4 0), (5 3 1), (5 3 3) and (5 2 2) were found and correspond to the cubic phase of $LiMn_2O_4$ (JCPDS 035-0782). No sign of impurity phases was observed and all the peaks could be indexed to the cubic spinel of the space group Fd3m.[71] The (1 1 1) peak has the highest relative intensity (100 %) and this showed that Li^+ occupies the tetrahedral sites. The absence of the (2 2 0) peak indicates the absence of the inverse spinel as this peak only appears when a cation occupies the tetrahedral site.[72] Table 4.2 summarises the parameters found with the X-ray diffraction analysis of $LiMn_2O_4$.

Table 4.2: Unit cell parameters of spinel $LiMn_2O_4$.

Lattice parameter / Å	8.2476
Unit cell volume / $Å^3$	561.03
Space group	Fd3m

The examination of the cross section of the three layers (Ni-NiO-$LiMn_2O_4$) was of importance and as shown in figure 4.8 (c), preparing a cross section with liquid nitrogen did not give satisfactory results. To improve the cross section view, samples were prepared with a cross section polisher (CSP), and the resulting SEM images can be seen in figure 4.11. The left image displays the untreated nickel foam embedded in a resin carrier. Figure 4.11 (b) shows the next treatment step, after heating at 600 °C where the oxide layer is formed and figure 4.11 (c) shows the completed product with a coating of $LiMn_2O_4$ on the thermally treated nickel foam.

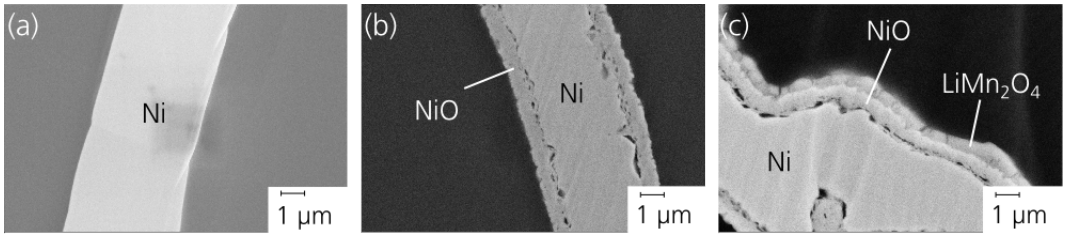

Figure 4.11: Cross section images of (a) untreated nickel foam, (b) thermally treated nickel foam and (c) nickel foam both thermally treated and coated with $LiMn_2O_4$ via sol-gel technique.

The CSP images display the coating of each layer, and an important issue that can be seen is the porous transition between nickel and the nickel oxide layer. The nickel oxide is 0.6-1.0 μm thick, but the adhesion to the pure nickel is not as anticipated. With a relatively slow oxide formation at 600 °C, such pores as can be seen in figures 4.11 (b) and (c) were not expected. Chapter 3.1.2.1 describes the importance of this oxide layer, and figure 4.4 (f) shows its increased porosity ensuring the improved adhesion to the cathode material. This designated property is illustrated in figure 4.11 (c), where it can be seen that the adhesion of the third phase (NiO-$LiMn_2O_4$) is significantly better than that of Ni-NiO.

Several attempts were made to avoid this phenomena as an inhomogeneous ox-

ide layer with pores, cracks and microchannels could lead to reduced electronic contact of the current collector for the electrochemical measurements. The nickel foams were first treated at higher temperatures, then a lower heating rate (2 K/min) was tested. However, following SEM examinations revealed no significant change in structure, and the porous transition remained in spite of the numerous efforts. F. Czerwinski et al.[73] have described how the surface structure of nickel has a great influence on the nucleation of the oxide growth. Certain surface treatments, such as chemical or mechanical polishing, can lead to an oriented nucleation and epitaxial growth of NiO. Such surface treatments could improve the NiO growth on the nickel foam. In addition, S.V. Kumari et al.[74] described the different oxide growth processes at different temperatures. Mainly it can be said that the nickel oxide grows along short-circuit paths, mostly along grain boundaries, but also through cracks and microchannels. At room temperature a very slow oxidation takes place, and above 200 °C a grain boundary diffusion is observed. At higher temperatures the oxidation is said to be controlled by the diffusion of Ni into the oxide layer along the grain boundaries.

The Kirkendall effect could also explain the porous transition seen in figure 4.11 (c). When atoms of different sorts diffuse with unequal partial diffusion coefficients, a vacancy diffusion mechanism, called the Kirkendall effect, occurs. Kirkendall found that displacement of one part of diffusion couple relative to another one was accompanied by a pore formation. Later experiments proved that the Kirkendall effect is quite general for any directed vacancy fluxes and the effect is present in such processes as self-diffusion in the single-component couples with contacting layers of different structure.[75] J.G. Railsback et al.[76] have examined the Kirkendall effect during the oxidation of nickel nanoparticles. Depending on the size of the nanoparticles, either a hollow (single void) or porous (multiple voids) NiO_x was obtained upon oxidation. When the outward diffusion of the metal cation is much faster than the inward diffusion of the anions, an inward flux of vacancies accompanies the outward metal cation flux to balance the diffusivity difference. The porous transition between Ni and NiO can be explained through a slow self-diffusion (slower than cation diffusion through the NiO layer) and several voids and multiple bridges form that connect the bulk Ni to the NiO layer. Railsback et al. also proved that the oxidation temperature of nickel does not affect the reaction mechanism itself,

only the reaction rate. Although literature [76, 77] presumes that the diffusion coefficient of metal is higher than that of oxygen, it would be interesting to measure the diffusion coefficient of the two components as a means of proof for the Kirkendall effect. However, due at the time it was decided that a TEM analysis was necessary to understand more of the oxide growth and to learn more about the microstructure of the coated nickel foam.

A selection of the STEM and TEM images of the $LiMn_2O_4$ coated nickel foam can be seen in figure 4.12. A rod of the foam lattice (as seen in figure 4.8) has been cut and thinned by the FIB method, resulting in this lamellar. Figure 4.12 (a) display a STEM image of the coated nickel foam. Figure (b) shows a TEM image with a focus on all three layers and the porous transition between nickel and nickel oxide.

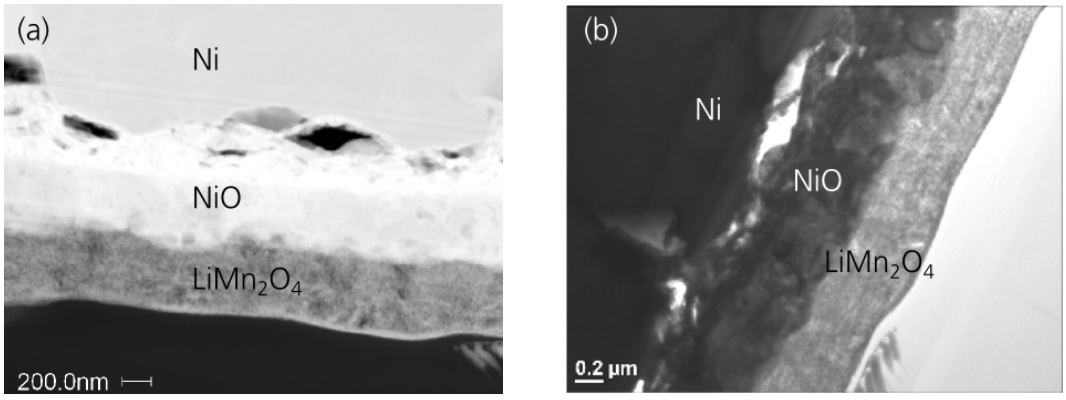

Figure 4.12: Transmission electron microscopy images of $LiMn_2O_4$ coated nickel foam. a) STEM image and b) TEM image.

By the means of the TEM analysis it could be stated that the nickel base material is polycrystalline with several crystal boundaries within larger grains. The oxide layer was seen to have two different zones, the inner one (to Ni) consisted of coarser grains and the large pores as discussed above. The pores were between 0.2-0.8 μm in length and could be found either on the boundary between Ni and NiO or in the NiO layer itself. The outer NiO zone (to $LiMn_2O_4$) consisted of finer grains and appeared more homogeneous. The $LiMn_2O_4$ layer was also found to be polycrystalline with finer grains than the other two compounds. With the use of TEM images, other interface layers besides the one in NiO was not observed, however, an EDS linescan as well as elemental mapping were made to further investigate interface layers of the coatings.

A vertical line in the sample was chosen for scanning (figure 4.13(a)), spanning from the nickel base material and into the carbon-based resin. A total of thirty EDS measurement points were used, resulting in a linescan (figure 4.13(b)).

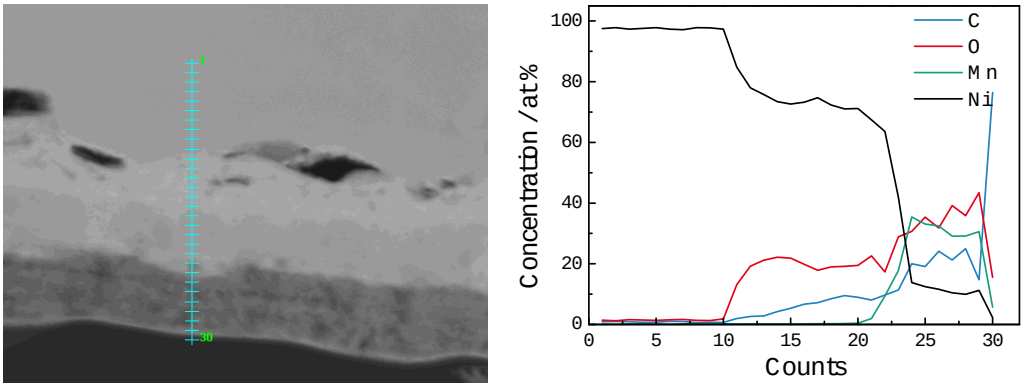

(a) (b)

Figure 4.13: EDS linescan of the different layers of nickel foam with $LiMn_2O_4$ coating. a) TEM image of area scanned, b) linescan.

In the EDS linescan pure nickel is detected until point 10. From there on the Ni-NiO layer begins, however, the ratio is not 50:50 at% which suggests that an non-stoichiometrical oxide formation occurred or that the nickel diffusion along the grain boundaries have created an non-stoichiometrical relation in the layer. The outer $LiMn_2O_4$ layer stretches from point 22-29. The atomic percent of Mn rapidly escalates while the Ni-content decreases. An increased oxygen content is also observed as there are more oxygen found in the $LiMn_2O_4$ layer than in NiO. Also, about 20 % carbon can be found in the outer layer, indicating that the carbon-based resin has infiltrated cracks and microchannels in the $LiMn_2O_4$-coating. A small amount of nickel can also be found in the outer layer which suggests that nickel diffuses further out with the thermal treatment of the $LiMn_2O_4$-coating. However, repeated EDS linescans showed lower values of nickel in the $LiMn_2O_4$ layer (1-10 %), thus leaving it open for discussion what the absolute value of nickel in the $LiMn_2O_4$ layer is, and how this could influence the $LiMn_2O_4$ layer surface.

The elemental mapping is imaged in figure 4.14. The image above illustrates the scanned area, and the four smaller images represent the elements oxygen, manganese,

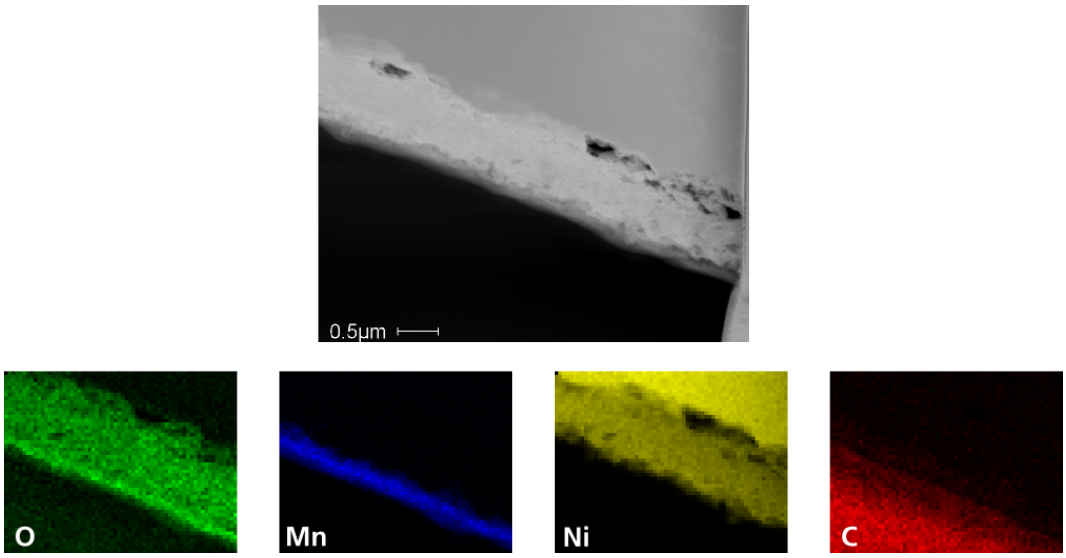

Figure 4.14: Elemental mapping of the $LiMn_2O_4$ coated nickel foam.

nickel and carbon. The results of the EDS mapping confirms what could be seen in the linescan. Oxygen was present in the two outer layers, NiO and $LiMn_2O_4$, although the concentration was seen to increase in the $LiMn_2O_4$ layer. Mn could only be found in the outer layer, whereas Ni could be seen in larger quantities in the bulk material, as well as in the NiO-layer. The EDS linescan in figure 4.13(b) showed a nickel content in the $LiMn_2O_4$ layer, however, this was not found via EDS mapping. Carbon was mainly found in the resin, although it could again be seen that the carbon has diffused into the $LiMn_2O_4$ layer through cracks or microchannels.

Coating methods

Due to ease of preparation with the precursor solution the first coating attempts were executed via dip coating as described above. As seen via SEM images and XRD analysis, the first coatings were relatively thin, ranging from 0.5 - 1.0 μm. However, to utilise the large surface area of the foam structure and also increase the volumetric energy density, experiments with thicker coatings were carried out. A thicker coating could either be obtained through a higher solids content of the precursor solution or by multiple dip-coating. A higher solids content of the precursor leads mainly to inhomogeneities in the distribution of the material on the foam substrate. Dripping effects upon coating gave a dense coating on the lower edge of the substrate and a thinner layer on the upper parts of the substrate. From double and triple dip coating more cracks and inhomogeneities on the surface originated. The adhesion between

the layers was also questionable, although it was not further studied.

To obtain thicker coatings and more control of the layer parameters, different coating methods were studied. Electrophoretic deposition (described in chapter 3.1.2.3) seemed to be an interesting method as the layer thickness could be controlled by varying parameters such as voltage, holding time and the distance to counter electrode. A solution of $LiMn_2O_4$ powder with binder and carbon black was made as described in table 3.4, and fitted nickel foam substrates were attached to the potentiostat setup and coated via the electrophoretic deposition method. SEM images of the resulting samples can be seen in figure 4.15.

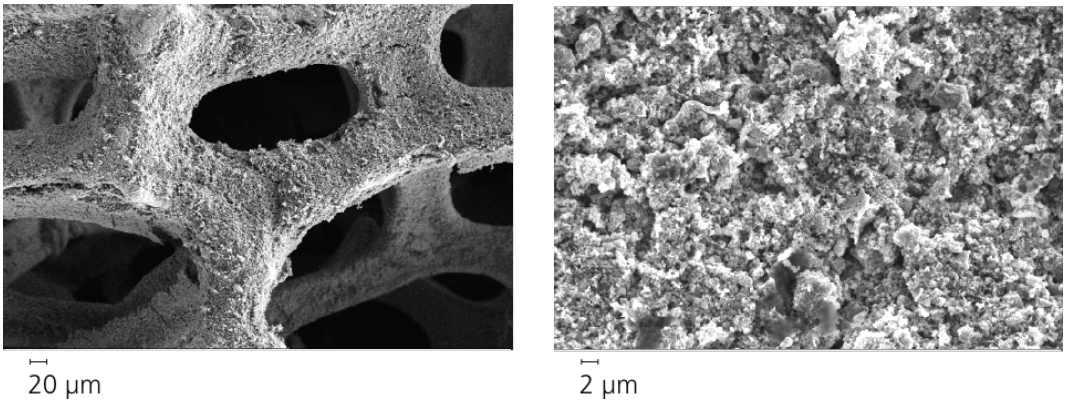

Figure 4.15: Scanning electron microscopy images of $LiMn_2O_4$ coated Ni-foam via electrophoretics.

The coated foam lattice is displayed in the left figure. A relatively thick coating can be seen, although the layer does not appear to be completely even. A difference in thickness can be seen, and most likely this is dependent on the foam lattice orientation to the counter electrode. Not all areas of the foam lattice possess the same accessibility of the $LiMn_2O_4$ dispersion due to the counter electrode being on one side of the foam. The setup of the electrophoretic deposition was illustrated in figure 3.2. Electrophoretic deposition leaves the pores open, and in figure 4.15 (right) a fine microporous structure can be seen. Nanoscale particles are evenly distributed, although they tend to agglomerate. The loading of the foams can easily be controlled by varying the deposition time, as the voltage and distance to the counter electrode were held constant. Depending on deposition time the loading varied between 10 and 40 mg per sample where an area of about 1 cm^2 was inserted

into the $LiMn_2O_4$ dispersion. However, an unwanted effect by EPD was detected. A sample set would be coated using the same dispersion, but after coating the first sample, the current decreased indicating that the amount of charged powder particles also decreased. This resulted in a reduced loading for the later samples coated in one set. Using a fresh dispersion solutions for each sample would avoid this effect, but demand more material. The electrochemical effects can be found in chapter 4.1.2.

Another approach to the metallic foams was to utilise the pores and fill them with cathode material, hence increasing the volumetric energy density of the sample. With the 3D-structure of the current collector, the active material would have short diffusion paths and would ensure improved kinetics upon charging/discharging. The previous coating methods did not fulfill this requirement with filling the pores, and infiltration (as described in chapter 3.1.2.4) was examined as a new coating method.

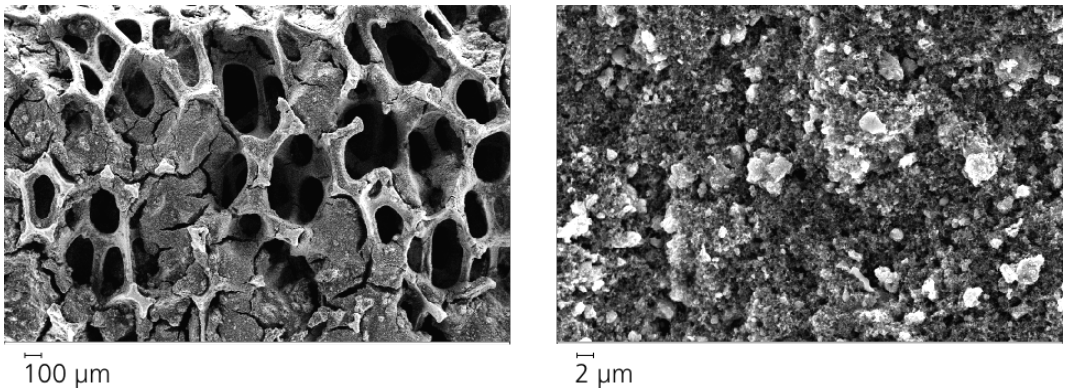

Figure 4.16: Scanning electron microscopy images of $LiMn_2O_4$ coated Ni-foam via infiltration.

Fitted nickel samples were placed in a silicon holder and the $LiMn_2O_4$ containing slurry was infiltrated on both sides of the foam. The SEM images of the resulting samples are shown in figure 4.16. In the left figure it can be seen that the pores are partially filled, however not all the pores have been infiltrated with the $LiMn_2O_4$ slurry. Nevertheless, the material amount when coating with the infiltration method has increased (the loading of cathode material increased to 100 mg/sample), and the more interesting electrochemical results can be found in chapter 4.1.2. Filling all pores could be obtained by varying the viscosity of the slurry or by multiple infiltration. The right SEM image in figure 4.16 shows the microstructure of the

coating. Some larger particles in μ-range can be seen, though most particles are nanoscale and have agglomerated as with the microstructure of the electrophoretic coating. When preparing the slurry, the $LiMn_2O_4$ powder is ground and then mixed with carbon black in a planetary mill. The milling time and speed could be optimised to obtain a more homogeneous particle distribution.

4.1.2 Electrochemical characterisation

One of the greatest challenges using $LiMn_2O_4$ as a cathode material is the Mn dissolution into the electrolyte (as described in chapter 2.4). B. L. Ellis et al.[25] describes how acidic electrolytes, formed from the hydrolysis of Li salts in organic electrolytes will etch a $LiMn_2O_4$ electrode via a disproportionation reaction: $2Mn^{3+} \rightarrow Mn^{2+} + Mn^{4+}$. The electrolyte $LiPF_6$ was mentioned to release HF. Thus, the dissolution of $LiMn_2O_4$ and strategies to avoid it, have been the subject of extensive research. The Mn dissolution in other electrolytes than $LiPF_6$ was to be examined. By soaking the $LiMn_2O_4$ powder in different electrolytes for 2 weeks at room temperature in an argon filled glovebox, the Mn dissolution content is found via ICP-OES and the results are shown in table 4.3.[78]

Table 4.3: Mn dissolution in different electrolytes.

Electrolyte	Mn dissolution / ppm
$LiClO_4$ in PC	1
$LiClO_4$ in 1:1 EC/EMC	2
$LiPF_6$ in 3:7 EC/DEC	80
$LiPF_6$ in 1:1 EC/EMC	9

Clearly, the $LiClO_4$ electrolyte is a better choice when measuring $LiMn_2O_4$ electrodes. The Mn dissolution in both $LiClO_4$ in PC and $LiClO_4$ in EC/EMC is negligible, however, the much larger dissolution found in $LiPF_6$ in 3:7 EC/DEC confirms that the released HF will increase the Mn dissolution. All experiments with $LiMn_2O_4$ in this thesis was performed with $LiClO_4$ in 1:1 EC/EMC.

As described in chapter 2.6.1 cyclic voltammetry is one of the most versatile electrochemical methods available. As a first characterisation, a cyclic voltammogram (CV) is often analysed. The characteristic redox peaks of the substance can be confirmed

and the peaks can be compared with similar ones from literature. Also, any impurities in the substance would often appear as additional peaks and could also be detected in the CV. The $LiMn_2O_4$ coated nickel foam was assembled in a 3-electrode cell as described in 3.3.1 and the resulting CV curve can be found in figure 4.17.

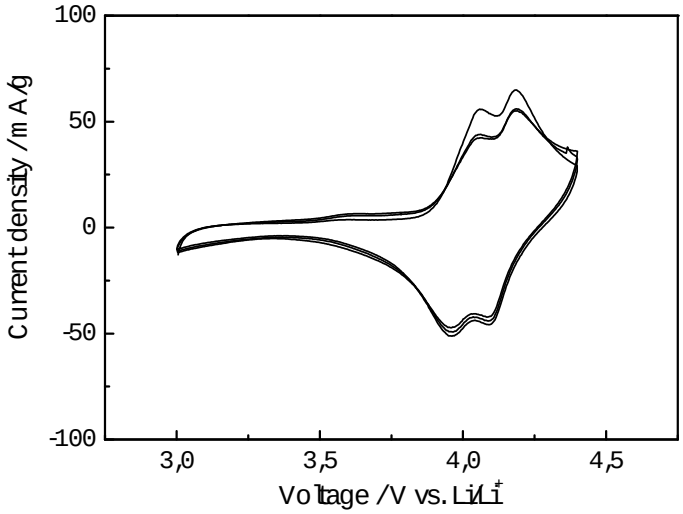

Figure 4.17: Cyclic voltammetry of the $LiMn_2O_4$ coated nickel foam with a potential sweep rate of 0.05 mV/s.

Two reversible redox peaks are seen in the CV, corresponding to Li^+ extraction and insertion and confirming the two-step redox reaction described by equations 2.6 and 2.7. Half a Li-ion is extracted at the time, the first reduction peak is at 4.1 V, the next at 3.9 V. The two oxidation peaks are seen at 4.0 V and 4.2 V. The redox peak positions correlate with values found in the literature[32, 79–81] and thus confirming the synthesis of pure $LiMn_2O_4$ as no impurity peaks are found.

At best, the current would return to zero before changing from oxidation to reduction, which is not the case for the CV of $LiMn_2O_4$ coated nickel foam seen in figure 4.17. The CV area appears a bit elongated in the vertical scale and the peaks are not very well defined. To examine the influence of the current collector on the shape of the cyclic voltammetry, a CV in the same voltage range was made on the thermally treated nickel foam without the $LiMn_2O_4$ coating. As seen in previous SEM and STEM images the coating contains cracks, therefore it is possible that the NiO-surface (available through cracks or microchannels) reacts with the electrolyte. Literature reviews reported the use of NiO as an anode material, obtaining a specific capacity

between 400 - 700 mAh/g.[47, 82–85] The effect of having NiO as an anode material on the current collector will be discussed in chapter 4.3. In addition the thermally treated nickel foam will also be examined in use with an anode material in chapter 5.1.2. First the contribution of the NiO layer must be determined in the cathode region and the cyclic voltammogram of the Ni/NiO foam can be seen in figure 4.18(a).

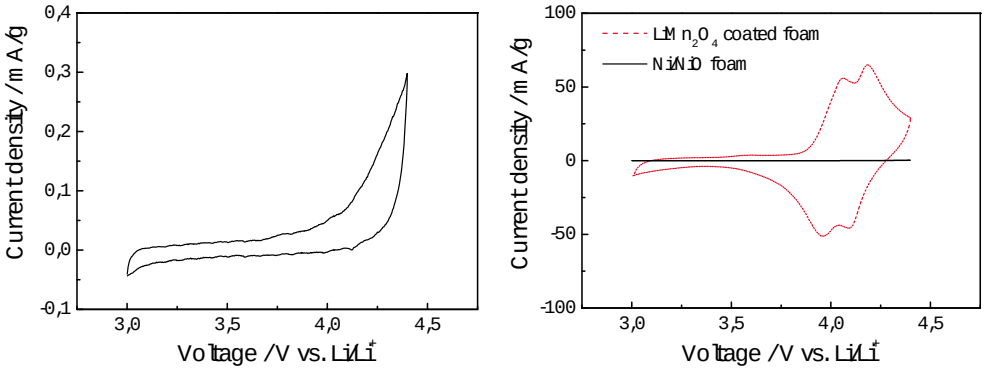

(a) (b)

Figure 4.18: Cyclic voltammetry of the thermally treated Inco foam at a 0.05 mV/s sweep rate. a) The nickel-nickel oxide foam b) the nickel-nickel oxide foam with $LiMn_2O_4$ coating.

Some activity of the nickel-nickeloxide foam can be seen, especially at a higher voltage where it seems that the substrate is not completely stable. Although when comparing the activity of Ni/NiO with that of $LiMn_2O_4$ (figure 4.18(b)) using the same scaling it becomes apparent that the activity of Ni/NiO has no influence on the overall cyclic voltammogram of $LiMn_2O_4$ coated on Ni/NiO foam. The indistinctive $LiMn_2O_4$ redox peak can thus be explained through sweep rate, cell assembly or electrolyte variation.

Galvanostatic tests in a potential range from 3.0 to 4.4 V with a current density of 100 mA per gram active material were carried out to measure the electrochemical performance of the prepared samples over several cycles. The active material was determined by weighing the sample before and after the coating and subsequent calcination process. The voltage profiles can be seen in figure 4.19(a). In general, the voltage profile for lithium extraction of $LiMn_2O_4$ is divided into two distinct plateaus around 4.0 V.[29, 86–88] The two plateaus indicate the two-step reaction (equations 2.6 and 2.7) and the two peaks seen in the cyclic voltammogram of the $LiMn_2O_4$ coated nickel foam. However, the voltage profiles in figure 4.19(a) did not

exhibit two clear voltage plateaus, although this can be explained by the indistinct CV peaks. In addition other studies of $LiMn_2O_4$ as a cathode material report the same behaviour[89, 90].

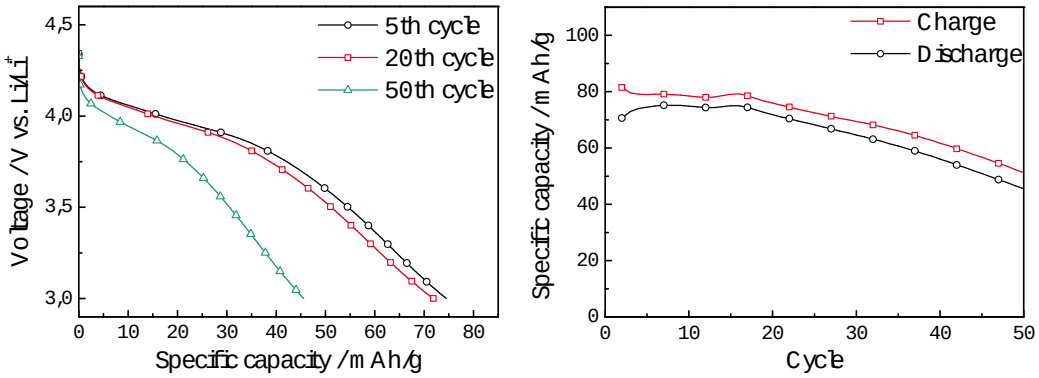

(a) (b)

Figure 4.19: Galvanostatic measurements of $LiMn_2O_4$ coated nickel foam a) Voltage profiles with constant current cycling b) Cycling behaviour with constant current cycling.

The lithium extraction curve for the 5th and the 20th cycle are comparable, the capacity reaches 75 and 72 mAh/g respectively. However, the 50th cycle shows a much lower capacity, reaching only 45 mAh/g. Obviously, the capacity retention for the first 20 cycles is much better than for the following 30 cycles. Voltage profiles can display some information about the electrochemical processes upon cycling in addition to the achieved capacity, though to study the life time expectancy of a battery, the cycling behaviour as seen in figure 4.19(b) is often presented. The cyclic behaviour of the cell displays the capacity as a function of the cycles.

The discharge capacity seen in figure 4.19(b) maintains 75 mAh/g over the first twenty cycles, then the capacity stoops to about 45 mAh/g for the 50th cycle. However, the theoretical capacity of $LiMn_2O_4$ is 148 mAh/g[91]. This extensive difference between obtained specific capacity and theoretical specific capacity can have two reasons. Either the synthesised $LiMn_2O_4$ material via the sol-gel route does not deliver the desired capacity or there are some unwanted side effects by using the relatively unknown thermally treated nickel foam. The large capacity gap could also be a combination of the two effects. In order to understand the reason for the low capacity, new measurements with $LiMn_2O_4$ coated onto an aluminum foil were

conducted. The standard current collector for cathodes is aluminum foil, hence the measurements can be directly compared with literature studies. This step would exclude the use of a porous foam as current collector and examine the material itself. The results of $LiMn_2O_4$ coated on aluminum foil can be found in chapter 4.2.

To examine the material's rate capability and the kinetics of the active material another measurement with varying C-rate (as described in chapter 2.6.2) was performed. Here the 1 C rate was defined at a current density of 75 mA/g (found in figure 4.19 at the fifth cycle as defined in chapter 3.3.3) and C-rates between 0.5 C (37,5 mA/g) and 16 C (1200 mA/g) in a potential range from 3.0 - 4.4 V were used. The resulting plot can be seen in figure 4.20.

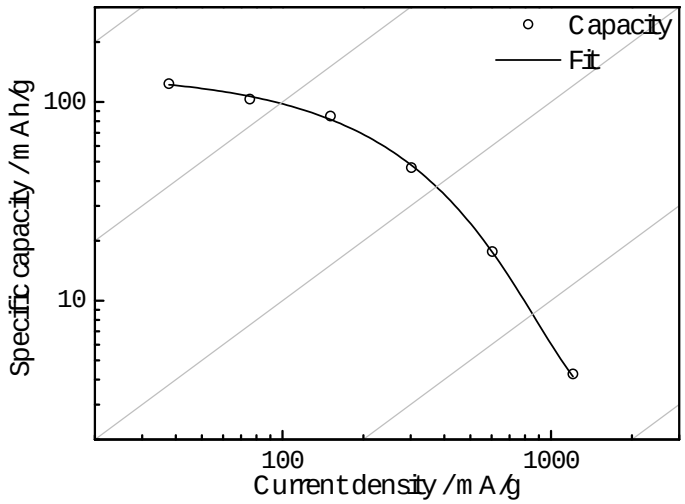

Figure 4.20: Specific capacity as a function of current density for the $LiMn_2O_4$ coated nickel foam.

As described in chapter 2.6.2, a smaller C-rate will give a higher capacity as the material has more time for lithium diffusion and charge transfer reactions. For the $LiMn_2O_4$ coated nickel foam a C-rate of 0.5 C (30 mA/g) corresponds to a capacity of is 124 mAh/g. Compared to the capacity found in figure 4.19 at 75 mAh/g, it is confirmed that the lower C-rate gives a higher capacity. At higher C-rates the capacity decreases accordingly as the time for the electrochemical reactions is reduced, and at C-rates above 4 C (300 mA/g), the system cannot deliver an acceptable capacity. 8 C and 16 C results in specific capacities of 17 and 4 mAh/g, respectively, thus the $LiMn_2O_4$ material can only withstand current densities of up to 300 mA/g.

Other coating methods were also tested, as described in the previous chapter. To utilise the large surface area of the nickel foam and to increase the volumetric energy density, coating of $LiMn_2O_4$ via electrophoretic deposition (EPD) and infiltration was carried out. The average loading of dip coating was about 17 mg/cm^2, for EDP the average loading was actually reduced to about 10 mg/cm^2, but the obtained coating was more homogeneous. Infiltration resulted in the highest loading with approximately 50 mg/cm^2 and naturally the highest volumetric density can be expected of the infiltration samples. In a comparison experiment, samples via dip-coating, EPD and infiltration were assembled in a 3-electrode cell and cycled between 3.0 - 4.4 V with a constant current density of 100 mA/g of active material. Figure 4.21 displays the comparison of galvanostatic measurement of the different coating methods.

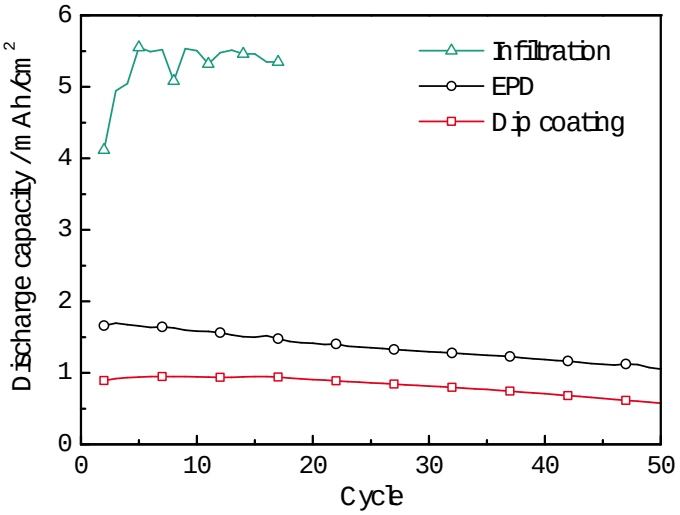

Figure 4.21: Cycling behaviour of $LiMn_2O_4$ coated nickel foam via three different coating methods: dip coating, electrophoretic deposition and infiltration

As expected, the $LiMn_2O_4$-infiltration sample shows a much higher area capacity at 5.5 mAh/cm^2, almost three times higher than that of the EPD sample with an initial capacity of 1.6 mAh/cm^2. Although the loading of the dip coating is slightly higher than that for the EPD sample, the volumetric capacity reaches only 1.0 mAh/cm^2, however, the capacity retention of the dip coating sample is the better one. For the infiltration sample, the cell sustained only 18 cycles before short-circuiting due to extensive dendrite growth on the lithium counter electrode. Fatal dendrite growth was seen to increase with current density, and as the infiltration sample was measured

at the highest current, (approximately 5 mA) the infiltration samples were subjected to extensive dendrite growth and long term cycling proved to be difficult. The result seen in figure 4.21 is to be handled with caution as it only portraits the area capacity. Using gravimetric capacity (mAh/g) the result would favour the dip coated sample with the lesser loading. However, both electrophoretic deposition and infiltration have proved to be interesting coating methods, and the average loading of the foam sample can be controlled by varying the coating method.

As mentioned above and shown in figure 4.19, the dip coating with the $LiMn_2O_4$ precursor solution does not reach the theoretical capacity of 148 mAh/g, and it cannot be confirmed if this unwanted capacity difference originates from the use of the foam, or if the synthesised material is not adequate. Therefore, measurements of the same $LiMn_2O_4$ precursor solution were performed when coated on aluminum foil as seen in the next chapter.

4.2 $LiMn_2O_4$ on aluminum foil

In order to examine the synthesised $LiMn_2O_4$ material without influence of other unknown parameters (such as the nickel foam current collector), the $LiMn_2O_4$ precursor solution was made into a $LiMn_2O_4$ powder, mixed into a slurry and coated onto a standard metallic current collector. The precursor solution was first thermally treated as shown in figure 3.1 resulting in a $LiMn_2O_4$ powder (the purity and phase was confirmed by XRD as described in chapter 4.1.1). This powder was mixed with binder, carbon black and solvent with a composition displayed in table 3.1 and coated onto an aluminum foil via doctor blading as described in chapter 3.1.2.2. The use of aluminum as a standard current collector for cathode materials was depicted in chapter 2.5.3 as the substrate is stable in the wanted potential window for cathodes, 3 - 5 V. Swagelok®-cells were assembled with circular disks of punched and pressed $LiMn_2O_4$ electrodes (chapter 3.3.1) and electrochemically tested.

4.2.1 Structural characterisation

As the active material coated on Al-foil originates from the same $LiMn_2O_4$ precursor solution as characterised above, a thorough structural characterisation of the material on aluminum was not necessary. A SEM image of the coated $LiMn_2O_4$ on aluminum foil can be seen in figure 4.22.

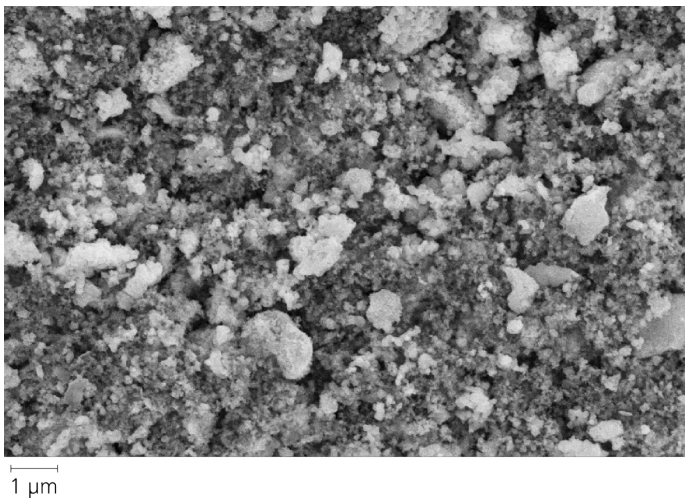

Figure 4.22: SEM image of $LiMn_2O_4$ cathode material on aluminum foil.

The SEM image illustrates a well dispersed powder, with some agglomerates in

μm range, although the main particles are rather in the nanometer scale. Punching of the electrodes into circular disk for cell assembly revealed that the adhesion between cathode material and current collector was not optimal. The adhesion is a common problem when using untreated aluminum foil as a current collector, however the adhesion can be improved via etching or sputtering of an interface layer to reduce the resistance between the current collector and the cathode.[92, 93] For these experiments the aluminum foils were only etched, however a lack of adhesion was still confirmed. After punching there was some material loss found on the edges of the circular electrode.

Doctor blading was performed with a distance of 100 μm for the slurry coating, however, after drying the thickness of the $LiMn_2O_4$ coating was reduced to an average of 25 μm. The average loading equates to 1.45 mg/cm^2. The electrochemical results of the $LiMn_2O_4$ coated onto aluminum foil can be found in chapter 4.2.2.

4.2.2 Electrochemical characterisation

A cyclic voltammogram was again made as the first electrochemical characterisation of the material. The CV of $LiMn_2O_4$ coated on Al-foil assembled in a Swagelok®-cell with a sweep rate of 0.1 mV/s can be seen in figure 4.23. The cyclovoltammogramm displays the two redox peaks characteristic of $LiMn_2O_4$ (described in equations 2.6 and 2.7) evolving around 4.1 V.

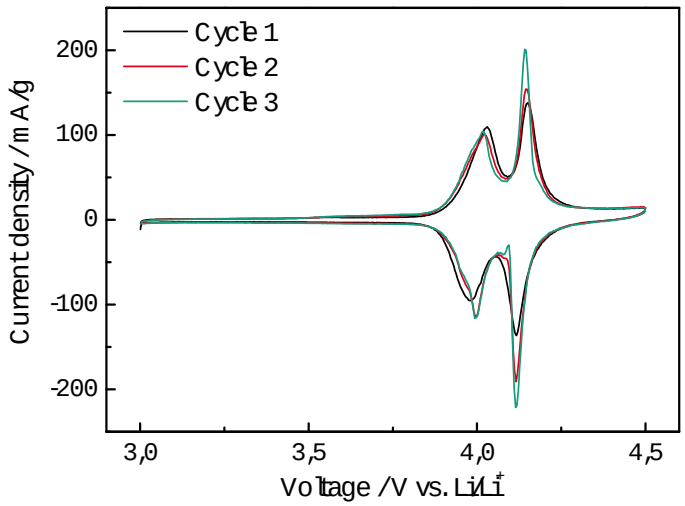

Figure 4.23: Cyclic voltammogram of $LiMn_2O_4$ coated on Al-foil via doctor blading.

The CV of the $LiMn_2O_4$ coated Al-foil have an ideal $LiMn_2O_4$ appearance, similar to many literature findings.[94–96] The CV peaks are more distinct and narrower, indicating faster kinetics of the material. When comparing the CV of the $LiMn_2O_4$ coated Al-foil with the CV of the $LiMn_2O_4$ coated foam (figure 4.17), the main feature of a CV is similar. Both cyclic voltammograms show the double redox peaks at around 4.1 V and further differences in the CV appearance will be discussed. However, the significance of these differences are partly unknown. In chapter 4.1.2 the minor influence of the foam on the CV appearance was discussed (figure 4.18(b)), although the difference in CV appearance between the $LiMn_2O_4$ coated foam and $LiMn_2O_4$ coated aluminum can be explained through other theories. The cell setup was different for the two samples, the $LiMn_2O_4$ coated Ni-foam was assembled in a 3-electrode cell and the $LiMn_2O_4$ coated Al-foil was assembled in a Swagelok® cell. The different cells give rise to different internal resistances, especially as the 3-electrode cell does not contain a separator, and this could influence the CV appearance. Another factor is the sweep rate of the CV. K.-L. Lee et al.[97] showed that an increased cyclic scan rate influenced the peak height of the CV as well as the position of the peaks. With an increasing scan rate, the anodic/cathodic current increases as well. Another factor could be the particle size. T.-F. Yi et al.[94] proved that the particle size of $LiMn_2O_4$ influences the peak height and position in a CV. A smaller particle size would shift the oxidation peaks to a higher voltage, indicating that more driving force is necessary to remove the lithium-ions from the cathode and thus resulting in a higher resistance of charge transfer for smaller particles. As the two samples were fabricated via different routes (dip coating on nickel foam vs. doctor blading on aluminum foil), the particle size will differ and hence influence the CV appearance. The difference in CV appearance between figure 4.23 and figure 4.17 most likely originates from all the factors mentioned above.

Electrochemical characterisation of $LiMn_2O_4$ coated on Al-foil followed with galvanostatic measurements (figure 4.24) to observe the cycling behaviour at a current density of 100 mA/g.

The specific capacity of both charging and discharging vs. cycle number is outlined, as well as the coulombic efficiency as a function of cycle number. It can be seen that a specific discharge capacity of 145 mAh/g is reached in the first cycles, thus

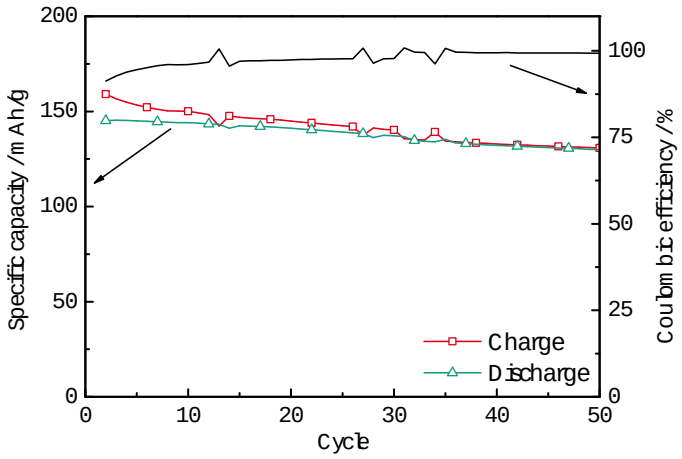

Figure 4.24: Cycling behaviour of $LiMn_2O_4$ coated on Al-foil via doctor blading measured with a current density of 100 mA/g.

obtaining a specific capacity near the theoretical capacity of 148 mAh/g[91]. This value exceeds most of the specific capacities of $LiMn_2O_4$ coated on Al-foil found in the literature[29, 32, 70, 79, 94] and thus proves that the synthesised material has excellent electrochemical properties. The specific capacity is calculated by using the active mass of the sample, i.e. subtracting the amount of carbon black and binder. On the right axis in figure 4.24 the coulombic efficiency is depicted. The coulombic efficiency (CE) is defined as the ratio between discharge capacity to charge capacity. After 35 cycles the CE has reached 99.5 %, showing the excellent cyclability and lack of unwanted side reactions.[98] Further cycling of the material (over 50 cycles as shown) reveals some instability of $LiMn_2O_4$ as described in chapter 2.4 and can be related to the Mn dissolution and the Jahn-Teller effect. Although the Mn dissolution was in this case reduced (as proven in table 4.3) as a non-HF producing electrolyte was used ($LiClO_4$ in 1:1 EC/EMC).

Thus the question that arised in the end of chapter 4.1.2 has been answered; the synthesised $LiMn_2O_4$ material possesses the wanted qualities expected of a cathode material, an outstanding specific capacity as well as an adequate stability over the first 50 cycles. The reason for the lower capacity when coating $LiMn_2O_4$ on nickel foam must originate from effects with the foam itself or with the NiO layer.

However, comparing the results on another basis would also favour the foam substrate samples. All comparison of the two samples was made on the basis of the

mass specific capacity. However, considering the capacity in mAh per area (cm^2) would give the foam samples an advantage. Figure 4.25 compares the two substrates with $LiMn_2O_4$. Figure 4.25(a) displays the comparison on the basis of a gravimetric capacity, whereas the area capacity is displayed in figure 4.25(b).

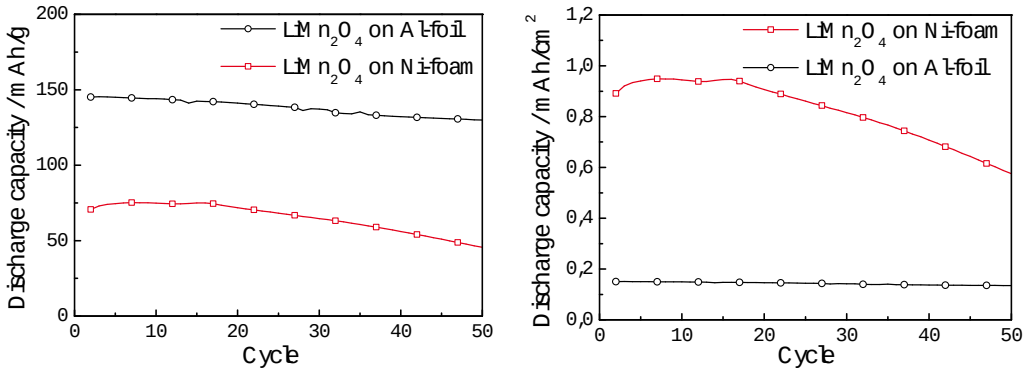

(a) (b)

Figure 4.25: Comparison of galvanostatic measurements of $LiMn_2O_4$ cathode coated on nickel foam and coated on aluminum foil. a) Area specific capacity and b) active mass specific capacity.

Y. Gogotsi et al.[99] claim that reporting the energy or power density per weight of active material alone, may not give a realistic picture of the performance of the assembled device. The weight of the other components, such as current collector, separator, connectors and packaging have to be taken into account. The thickness of the electrode is also an important factor, and much uncertainty arises from only reporting gravimetric capacities. The gravimetric density is almost irrelevant compared to area or volumetric energy for microdevices and thin-films energy storage solutions, as the weight of the material used in a micrometer-thin film on a chip is negligible. Thus the importance of reporting the areal or volumetric energy increases as the market for lithium-ion batteries is expanding. As can be seen in figure 4.25, with a necessity for a higher areal capacity, the $LiMn_2O_4$ coated on foam substrates would be the better choice. However, reporting the true volumetric capacity of the foam samples proved difficult due to the large porosity. The commercially available nickel foams contain pores as large as 1 mm, thus having empty space that will be flooded by electrolyte, thereby increasing the weight of the device without adding to the capacity. To optimise the volumetric density, the pore size would have to be reduced, and the foams made thinner. For automotive applications, or storing large

amounts of energy, the gravimetric capacity is still the more important issue, hence, the $LiMn_2O_4$ coated on aluminum foil is better suited for such applications.

4.3 Summary and general discussion

This chapter has described the synthesis and characterisation of the cathode material, $LiMn_2O_4$. The focus was both on the material itself, but also on the choice of a current collector. $LiMn_2O_4$ was chosen due to the increased obtained capacity compared to the commercially used $LiCoO_2$. Other properties of $LiMn_2O_4$ included abundance and lesser toxicity. A novel porous foam substrate was used as a current collector, supplying new possibilities with the cathode interaction. High porosity, increased mechanical strength and a 3-dimensional network providing enhanced electric conductivity were a few of the advantages with using a porous metal foam as current collector. In addition, the synthesised $LiMn_2O_4$ was also coated on a standard aluminum foil, to better understand the discrepancies between theoretical values and the obtained values (chapter 4.2).

In chapter 4.1.1, a foam selection was made based on availability and electrochemical stability within the wanted potential frame. A thermogravimetrical analysis was performed, thus the formation of an oxide layer could be studied. The oxide formation would lead to an improved adhesion with the cathode material, thus it was thoroughly studied via scanning electron microscopy and X-ray diffraction analysis. Due to energy consumption and a more heterogeneous surface structure, the commercially available nickel foam from Inco was chosen as the current collector for the $LiMn_2O_4$ cathode.

Next, the synthesised $LiMn_2O_4$-sol was studied. Through inductively coupled plasma investigations, the right stoichiometric composition could be found. The solution was also analysed with thermogravimetrical measurements, thus examining the spinel transition of the $LiMn_2O_4$ precursor solution and optimising the following thermal treatment. The $LiMn_2O_4$ spinel could also be determined via XRD, however, only with the powder form of $LiMn_2O_4$. The combination of $LiMn_2O_4$ on nickel foam lead to uncertainties as the nickel substrate dominated the spectrum (as seen in figure 4.9).

For analysis of the entire system, $LiMn_2O_4$ coated on thermally treated nickel foam ($LiMn_2O_4$/NiO/Ni), cross section analysis with SEM and TEM proved beneficial. The excellent adhesion between NiO and $LiMn_2O_4$ was confirmed, although an unwanted porous transition layer between the nickel and the nickel oxide was observed. Various attempts were performed to avoid the pores in the interface, but none proved effective. A possible explanation for the porous transition was found with the Kirkendall effect and due to different diffusion rates. However, the measurement of diffusion coefficients would be an interesting method to verify this explanation.

Several coating methods were examined to increase the average loading and to fully utilise the 3-dimensional structure that the foam offers. Through electrophoretics a homogeneous layer of $LiMn_2O_4$ could be deposited while the thickness could be controlled by varying the deposition time or other electrophoretic parameters. Infiltration of the foam with a viscous slurry provided a higher loading with partial filling of the pores. All samples were electrochemically characterised, and the methods and substrates compared against each other. A cyclic voltammogram of the $LiMn_2O_4$ on nickel foam, seen in figure 4.17, proved the expected two-step Li-insertion of $LiMn_2O_4$, and the contribution of the foam substrate alone was controlled. The NiO layer on the current collector is an anode material, thus electrochemically active in the anode region ($< 3V$). A control of the activity in the cathode region was necessary to understand possible interactions (figure 4.18).

The $LiMn_2O_4$ coated on thermally treated nickel foam was also galvanostatically measured, where a specific capacity of 80 mAh/g was observed in the first cycles (figure 4.19). A variation of the current densities also lead to the conclusion that the kinetics of the material was not sufficient at current densities above 300 mA/g, where the capacity rapidly dropped. The electrochemical analysis of the $LiMn_2O_4$ on Ni foam showed a major disagreement with the theoretical value of the capacity. Thus it was necessary to examine whether the disagreement came from the synthesised material itself, or from the interactions with the foam substrate.

To better examine the synthesised $LiMn_2O_4$, a known aluminum substrate was used as current collector. In chapter 4.2 it was proven that $LiMn_2O_4$ on Al-foil gave a specific capacity of 145 mAh/g which was very close to the theoretical capacity of 148 mAh/g. In addition, a coulombic efficiency as high as 99.5 % was obtained after the initial cycles. Hence, the synthesis of an excellent cathode material was confirmed, showing a very high capacity and excellent stability.

The main unresolved issue is why the $LiMn_2O_4$ cathode obtain much higher capacities when coated on aluminum foil than on the nickel foam. A certain difference is the coating method. $LiMn_2O_4$ was coated via doctor blading on aluminum, resulting in a rather homogeneous layer, although the adhesion to the etched Al-foil could be improved. Dip coating was used for $LiMn_2O_4$ on nickel foam, resulting in edge effects as the precursor solution runs to the edge of the vertically held foam and assembles on the edge, creating a very thick $LiMn_2O_4$ layer on the bottom of the foam, and a thinner layer on the top. If the full thickness of the $LiMn_2O_4$ layer can be utilised is questionable, as the lithium diffusion distances are longer and the electric contact very inhomogeneous.

Another reason might be the anode effect of the NiO layer on the thermally treated nickel foam. Literature studies have revealed NiO as an anode material, practically providing specific capacities in the range 400 - 700 mAh/g.[47] Whether this anode effect somehow interacts with the cathode material upon cycling has not been fully examined. The use of the Ni/NiO foam will be proven more successful in use with another anode material, as chapter 5 will show. However, a CV of the NiO in the cathodic potential range showed no apparent effect, thus a direct influence cannot be confirmed. Most likely, the disagreement with the theoretical capacity when using foam substrates might arise from the porous transition between the nickel and the nickel oxide as seen with cross section SEM and TEM. These voids and pores result in reduced electric contacting, which would significantly reduce the materials cyclability. Further work should investigate other methods to preserve the excellent adhesion of $LiMn_2O_4$ without the formation of the nickel oxide layer. A mechanical or chemical pre-treatment of the nickel foam might give the same results as the porous nickel oxide layer, and with that improving the capacity of $LiMn_2O_4$ on porous foam substrates.

Chapter 5

Tin-containing anodes

Extensive research on new, alternative anode materials has been performed over the last years. The commercially used graphite anodes are relatively stable and safe, however, the theoretical capacity of 372 mAh/g leaves room for improvement. Alloy anodes consisting of silicium or tin have been the subject of much research as the theoretical capacity can be greatly improved compared to the graphite anode. This chapter focuses on the use of Sn-anodes as alternatives to the carbon anode. Compared to the rather moderate Li-intercalation of graphite (chapter 2.3), a maximum of 4.4 lithium-ions per formula unit can be inserted into tin, giving a $Li_{4.4}Sn$ structure with a much improved theoretical capacity of 994 mAh/g[11]. The main challenge with using elements such as tin or silicon as anode is the great volume expansion upon cycling. This chapter will discuss this challenge and suggest several methods to improve the cyclability of the material.

5.1 Nanowire tin oxides

With the expertise from the University of Cologne on nanostructured compounds, a concept of nanowire tin oxides was developed. Via chemical vapour deposition (as described in chapter 3.1.3), nanowires could be directly deposited on a copper current collector. Nanowires or nanotubes offer several advantages over bulk material or standard film electrodes as there is no need for binder or other inactive materials. In addition, the nanowires provide short diffusion distances within the electrode. The novel process of growing the nanowires directly on the current collector ensures an efficient 1D electron transport down the length of every nanowire. In addition,

the increased surface area leads to higher rate capabilities and the nanowires can also provide the necessary volume of free space to accommodate the expansion and strain during alloying.[100, 101]

Various SnO_2-based materials have displayed extraordinary electrochemical behaviour such that the initial irreversible capacity induced by Li_2O and Sn formation and the abrupt capacity fading caused by volume variation could be effectively reduced when in nanoscale form.[20] The alloying mechanism of SnO_2 can be seen in equations 2.4 and 2.5 and the theoretical capacity of SnO_2 amounts to 781 mAh/g[21, 102, 103]. Literature studies show a dispersed view on the by-product Li_2O. Some reviews regard the by-product as inactive material produced by the irreversible transition in the first cycle, while others regard Li_2O as an additional buffering element to accommodate the strains and volume change of Sn upon cycling.[16, 21] Y.-D. Ko et al.[104] describe Li_2O as an inactive buffering part, well known to enhance cycling characteristics by mitigating the agglomeration of Sn or Li-Sn alloy domains resulting from substantial volume variations.

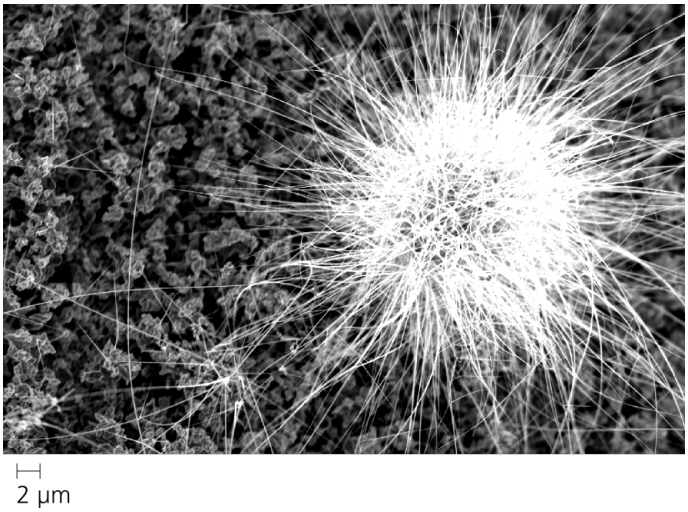

Figure 5.1: SEM image of initial SnO_2 sample.

Figure 5.1 shows a SEM image of the initial SnO_2 material, where the thin nanowires grown directly on a copper current collector can be seen. The SEM image reveals a cluster of nanowires, originating from one growth area, as well as regions without the wanted SnO_2 nanowires. A following EDS analysis excluded the presence of impurities, as only Sn, O and Cu were detected. A scan of the area seen in figure

5.1 without nanowires still reported the presence of substantial amounts of Sn. It cannot be claimed that there are regions without SnO_2, although it can be seen that the growth of nanowires did not take place in this region. Possibly, the SnO_2 growth was uneven, resulting in different morphologies with areas of nanowires and areas of a SnO_2 film. The effect of this uneven nanowire growth will be discussed later.

As a means of characterisation and identification of the new anode material, cyclic voltammetry was used. The method is described in chapter 2.6.1, and is often used to identify electrochemical reactions during cycling. The cyclic voltammogram (CV) of the initial SnO_2 sample can be seen in figure 5.2, here cycled between 3.00 and 0.01 V with a sweep rate of 0.1 mV/s.

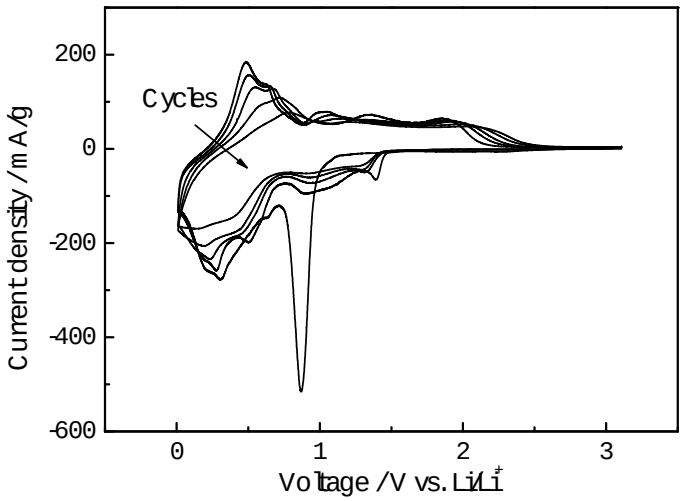

Figure 5.2: Cyclic voltammogram of the initial SnO_2 nanowire sample.

A major irreversible peak can be seen at 0.9 V, which is only occurring in the first cycle. This peak is related to the $SnO_2 \rightarrow$ Sn reduction as described by equation 2.4, and evidence of the distinctive peaks in the first cycle is found in literature[105, 106]. The minor peak at around 0.6 V can be attributed to the formation of solid-electrolyte-interphase (SEI) (confirmed in figure 5.14 without SnO_2- Sn transition). The reduction peaks from 0.5 V to 0.01 V are related to the formation of Li_xSn as described by equation 2.5. The following oxidation peak at 0.5 V can be attributed to the delithiation of Sn. From the second cycle, the redox processes seem to stabilise, although instead of the 0.9 V reduction peak, two smaller reduction peaks appear at 1.3 and 1.0 V, which remain over the next four cycles. M.-S. Park et al.[20] describes

similar reactions and argue that the single-crystalline structure of nanowires may disturb smooth Li^+ insertion into the interior of the nanowires, which leads to a slow lithiation. Furthermore, they claim that the new surface induced by the volume expansion in the first cycle will experience further electrolyte decompositions. Based on these considerations, it may be possible that the formation of Li_2O and electrolyte decomposition continues throughout the subsequent cycles.

The area under the curve of the CV represents a quantitative value of the materials specific capacity. Thus, as the area under the curve is significantly reduced, as seen in figure 5.2, it can be said that the specific capacity is reduced over the five cycles, and the stability of the material is not adequate. However, this quantitative evaluation is better examined with galvanostatic measurements. Figure 5.3 displays the voltage as a function of the specific capacity, measured at a constant current of 100 mA/g.

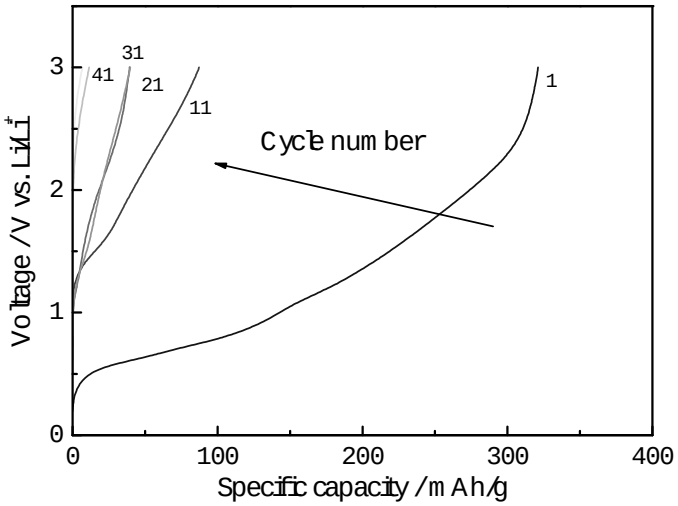

Figure 5.3: Voltage profiles of the initial SnO_2 nanowire sample.

The SnO_2 nanowire sample was cycled 50 times between 3.00 - 0.01 V, and figure 5.3 shows the voltage profile of every tenth cycle. The stability issue seen from the cyclic voltammetry is confirmed by the galvanostatic measurements. The SnO_2 material has a very low stability and the initial capacity loss is greater than acceptable. The first cycle reveals a specific capacity of about 320 mAh/g. However, after the tenth cycle this capacity is only 90 mAh/g and after fifty cycles the electrode is incapable of inserting any lithium. The initial capacity loss in the first ten cycles is too high, and after the tenth cycle only about 30 % of the initial capacity remains.

The electrochemical characterisation proved that the initially synthesised SnO_2 nanowire material did not provide the adequate strain relief upon cycling. With the great volume expansion from lithium insertion, the material could not accommodate the structural change with the initial concept and architecture. The cycled sample was examined with electron microscopy which could verify the massive structure change upon cycling, and chapter 5.1.1 illustrates the further effects of volume change upon cycling with the means of ex-situ electron microscopy.

Several possible solutions or improvements to the architecture of SnO_2 nanowires were suggested. Apparently, the buffering effects of Li_2O together with the free volume of the nanowires were not sufficient to reduce the stress upon cycling, and other architectures must be examined. In cooperation with the University of Cologne, several new concepts for the nanowires were developed, illustrated by the schematics in figure 5.4.

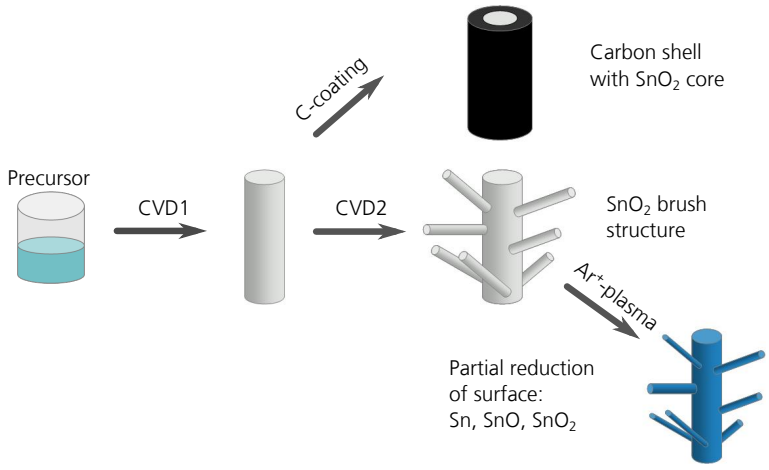

Figure 5.4: Schematic of different SnO_2 structure concepts, adapted from R. von Hagen[107].

The first improvement included carbon coating. After initial nanowire growth via CVD, an amorphous carbon coating was added, resulting in a core-shell architecture. Literature studies revealed an improved cyclic stability with the use of carbon coating, as the carbon shell acted as a structure stabilising matrix for the SnO_2 nanowires upon cycling.[108, 109] Although the literature studies revealed similar work with carbon coated Sn-nanowires, this work contained the first Sn-nanowires directly

grown on the copper substrate. The carbon coating should also provide a better adhesion to the substrate, thus preventing separation from the current collector. Further, the mechanical stability, the conductivity of the material and the electronic transportation was greatly improved with a carbon shell .

The second new improvement of the SnO_2 nanowires includes a second CVD-step, resulting in a brush-like structure. With the first CVD process, single nanowires are produced, and with the second CVD process, other nanowires grow onto the first, hence a much higher active surface area and space filling are achieved with a branch network of SnO_2 nanowires. A higher surface area is seen to give enhanced electrochemical reactivity and higher capacity.[21] The size and growth of the nanowires can be controlled by the CVD-parameters, such as pressure and temperature.

The third new architecture involved a surface reduction of the SnO_2. The brush-type SnO_2 nanowires grown by double CVD were modified by Ar/O_2 plasma treatment through preferential etching of the lattice oxygen atoms, which resulted in a non-stoichiometric surface composition.[110] The surface of the nanowires now consisted of a mixture of SnO_2, SnO and Sn, and part of the irreversible transition to Sn happening in the first cycle had already taken place, resulting in a higher theoretical capacity, above the 781 mAh/g for pure SnO_2. More details to the individual parameters used when producing these new SnO_2 structures can be found in the PhD thesis of R. Fiz, University of Cologne[59]. The SEM images of the new SnO_2 nanowire concepts can be seen in figure 5.5.

The carbon-coated SnO_2 nanowires as seen in figure 5.5(a) appear slightly thicker than the initial sample due to the additional carbon shell. The brush-type SnO_2 nanowires (figure 5.5(b)) represent a very high surface area with several very fine nanowires growing onto a central nanowire. The third concept, seen in figure 5.5(c), represent the Ar^+ plasma reduced surface of brush type SnO_2. A large structural difference from the standard brush type cannot be seen, although the Ar^+ reduction seems to make the outer nanowires slightly finer or thinner. All samples appear to have a thicker and more homogeneous loading than the initial SnO_2 nanowire sample, as seen in figure 5.1. Corresponding EDS measurements were performed on all three samples, and the presence of impurities could be excluded.

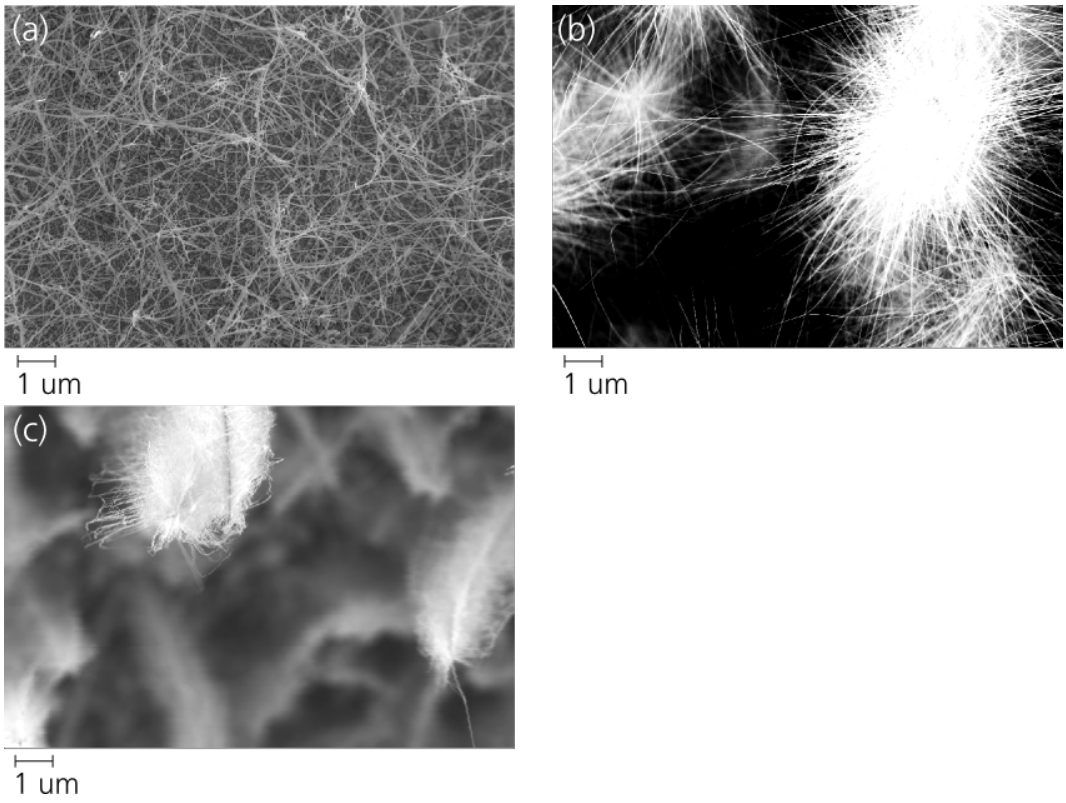

Figure 5.5: Scanning electron microscope images of the new SnO_2 concepts; (a) carbon-coated SnO_2, (b) brush-type SnO_2 and (c) Ar^+-reduced brush-type SnO_2.

In order to quantify the improvements of the new nanowire concepts, galvanostatic measurements were performed. All samples were cycled between 3.00 and 0.01 V with a constant current of 100 mA/g, and the specific capacities of the samples were compared (figure 5.6).

As can be seen in figure 5.6, all new SnO_2 concepts provide some improvement compared to the initial SnO_2 sample. The carbon shell with the SnO_2 core has the better properties, the capacity seems to stabilise after 40 cycles at a constant 60 mAh/g. However, typical of all samples is the substantial capacity loss in the very first cycles. Most samples have an initial capacity of about 300 mAh/g, which is still not close to the theoretical capacity of 781 mAh/g for SnO_2. Within the first 20 cycles, the capacity has been reduced to 100 mAh/g, meaning only a third of the Li-insertion capability remains. This typical first cycle loss is often described in literature[10, 11, 16, 18, 20, 22, 104–106], and is confirmed by the cycle behaviour

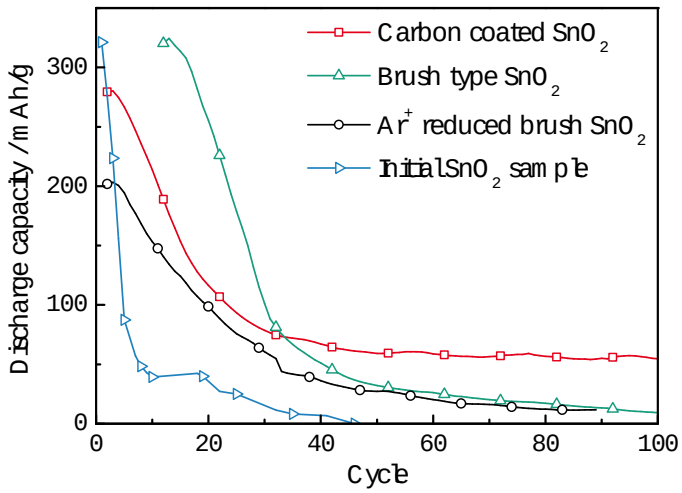

Figure 5.6: Cycle behaviour of the four different SnO_2 nanowire concepts; initial sample, carbon coated SnO_2, brush type SnO_2 and Ar^+-plasma reduced brush SnO_2.

measurements as seen in figure 5.6. Clearly, the new SnO_2 nanowire concepts showed minor improvements compared to the initial SnO_2 sample, although an ideal solution was not found with the new nanowire concepts.

It was decided to find the reason for the drastic capacity loss of the initial cycles with the means of ex-situ analysis of the cycled SnO_2 samples. The results can be found in chapter 5.1.1

5.1.1 Ex-situ analysis of cycled SnO_2 nanowires

As mentioned above, samples of the initial SnO_2 were examined via electron microscopy after the cycling was finished. The result showed a strong expansion of the nanowires, where they had grown together, forming thick wires. The nanowire network structure seen with SEM before the measurements, disappeared, leaving a two dimensional structure with longer Li-diffusion paths and most likely a separation from the current collector. Similar results were found when examining the improved SnO_2 samples after cycling. The SEM image of a SnO_2 sample after cycling can be seen in figure 5.7.

As the nanowires after 100 cycles were hardly recognisable, a series of experiments was developed in order to understand the process that took place upon cycling. Several standard SnO_2 samples were cycled to different voltages, each voltage repres-

Figure 5.7: Ex-situ scanning electron microscope image of a cycled SnO_2 nanowire sample.

enting a new process in the cyclic voltammogram. The cycled samples were examined with ex-situ SEM, to determine the stage of expansion and growth of the nanowires. A representative CV with the used stop-voltages can be seen in figure 5.8 and the succeeding SEM analysis in figure 5.9.

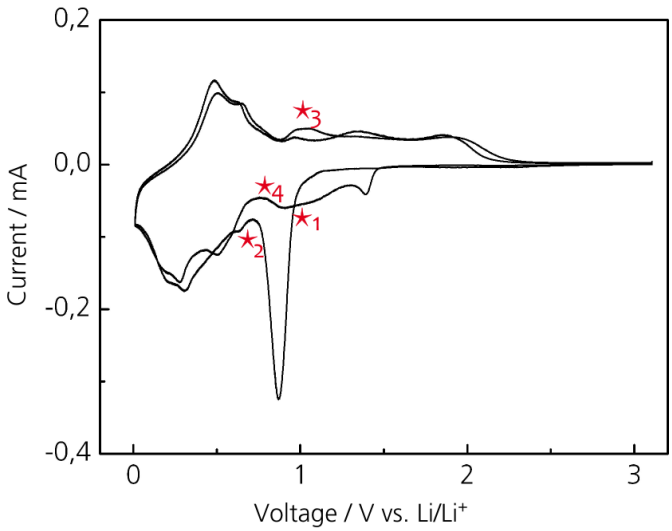

Figure 5.8: A typical SnO_2 cyclic voltammetry curve showing the stop-potentials for the ex-situ SEM analysis.

Four samples were cycled to different potentials. Each stop-voltage is marked with a star in figure 5.8, and the first sample was cycled to 1.0 V vs. Li/Li^+. This potential was chosen to lie before the transition peak seen at 0.9 V, thus no major structure

change should have happened at this potential. The second stop-potential was chosen after the transition peak at 0.7 V. The $SnO_2 \rightarrow Sn$ transition should be complete at this potential, and the expansion and growth of the nanowires might have started. The third potential was chosen in the oxidation region, at 1.0 V. The third sample was charged from 3.00 to 0.01 V, meaning full lithiation and great volume expansion, and further discharged back to 1.0 V. This potential was chosen because the delithiation seen in figure 5.8 should have taken place before 1.0 V, and the nanowires should ideally have shrunk back to their original size. The final sample was cycled to point 4, meaning that a full CV cycle took place, and further charging to 0.75 V. This sample underwent full lithiation and delithiation once, and was stopped short before the second lithiation took place. Each sample was examined via SEM and the following images can be seen in figure 5.9.

The uncycled SnO_2 sample is seen in figure 5.9(a) as a reference sample, where the size and structure of the nanowires before charge/discharge are illustrated. Figure 5.9(b) shows the sample cycled to point 1 (charged to 1.0 V), and already here a slight change is seen. The nanowires seem to have obtained a thicker layer, and the nanowires are connected together. However, this minor change could also originate from the ex-situ preparation methods. As the electrodes are removed from the Swagelok®-cells, they contain remains of electrolyte that has been absorbed in the electrode. The electrolyte leftovers were removed before the SEM analysis with the use of ethyl methyl carbonate (EMC), a solvent also found in the used electrolyte. The samples were washed with EMC and left to dry in argon atmosphere. For the sample in figure 5.9(b) it is possible that not all remains of the electrolyte were washed away, thus leaving a coating on the nanowires.

The second cycled sample was charged to 0.7 V, stopped right after the transition peak at 0.9 V. Figure 5.9(c) displays how this transition also changed the structure of the SnO_2 nanowires. The nanowires have expanded further, grown thicker and clustered together. Figure 5.9(d) represents the sample cycled to point 3, where a full lithiation and delithiation have taken place. This means that the nanowires underwent a great volume expansion on charging, and ideally they should have shrunk back to their original size after lithium extraction. However, as figure 5.9(d) shows, this is not the case. The nanowires have grown in thickness compared to the

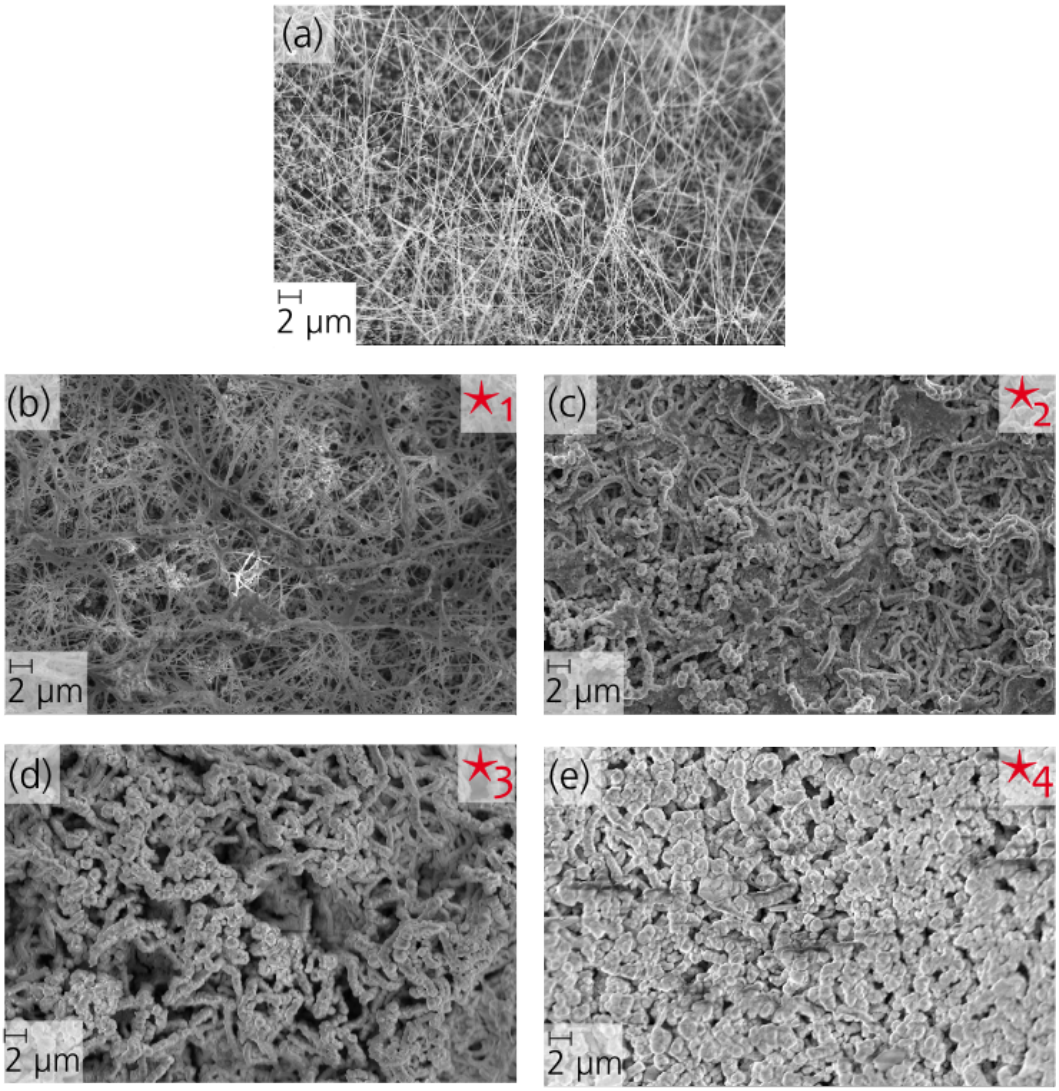

Figure 5.9: Scanning electron microscope images of the developing SnO_2 nanowire growth; (a) sample before cycling, (b) sample cycled to point 1, (c) sample cycled to point 2, (d) sample cycled to point 3 and (e) sample cycled to point 4.

previous samples, and the wanted shrinkage has not taken place. The last sample underwent a complete cycle, charged and discharged from 3.00 to 0.01 V, in addition charged to 0.75 V in the second cycle. Figure 5.9(e) shows the nanowire structure seen with SEM at this point. The nanowires have grown completely together and the thickness has increased by several orders. Indeed, the sample cycled to point 4 looks very similar to the sample examined after 100 cycles (figure 5.7) and it can be concluded that this massive structure change that is observed by ex-situ SEM takes place in the first cycle. Following cycles accentuate the process and eventually lead to separation from the current collector and wire-wire contact loss. The fine

3D network seen in figure 5.9(a) has transitioned into a thick layer of Sn with a 2D structure. The fine nanowires are no longer detectable resulting in longer lithium diffusion distances and a lower surface area. Further XRD and TEM analysis of the cycled samples can be found in the PhD thesis of R. Fiz, University of Cologne[59].

5.1.2 Anode materials on porous current collectors

The SnO_2 nanowires deposited via CVD on copper foil, experienced severe structural change upon cycling, as seen in chapter 5.1. With cycling, a segregation from the current collector was also observed and it was decided to utilise the benefits of a porous current collector as used for the cathode material in chapter 4.1. It was proven that the cathode material had a very good adhesion to the thermally treated porous nickel foam, in addition provided the foam a large surface area and a 3-dimensional structure. SnO_2 deposition via CVD on Ni foam proved feasible and several new samples were prepared with standard nanowire design. SnO_2 was deposited both directly on the Inco nickel foam and on the thermally treated nickel foam. Since the preparation of the anode materials took place at the University of Cologne, the thermal treatment was obtained with slightly different parameters (3 hours at 550 °C) where a thicker NiO layer was obtained.

As discussed in chapter 4, NiO is itself an anode material, with a theoretical capacity of 718 mAh/g[83], although practically obtaining capacities between 400-700 mAh/g[47, 82–85]. The thermal oxidation of nickel was initially performed to improve the surface structure and the adhesion to the cathode. Although, knowing that NiO also functions as an anode, the two charge/discharge mechanisms might add up and this possible double-anode effect was examined. However, nickel which has not been thermally treated and only contains traces of NiO, is not considered to be electrochemically active, thus SnO_2 is the only active element when deposited on pure nickel.

The SnO_2 nanowire growth was verified equal on Ni and Ni/NiO foam as the loading remained constant. The average loading of SnO_2 on the nickel foams was 3.32 mg/cm^2. A series of tests with the thermally treated foam was conducted to find the average oxide formation with the parameters used at the University of Cologne.

After thermal oxidation of several samples, with weighing before and after the oxidation, an average oxide formation of 8.9 % was found[111]. This value was used when calculating the complete active mass for the SnO_2 deposited on Ni/NiO as the NiO active part also had to be taken into account. Generally, the loading of SnO_2 on the nickel foam improved much compared to the previous loading on copper foil. The average loading on the standard metallic foil, when comparing all the SnO_2 concepts mentioned above, is 0.62 mg/cm^2. Thus, increasing the loading to 3.32 mg/cm^2 is possible when utilising the large surface area of the nickel foam. Figure 5.10 illustrates scanning electron images of the nickel foam with SnO_2 nanowires. A structural difference of SnO_2 grown on Ni or Ni/NiO was not observed with SEM.

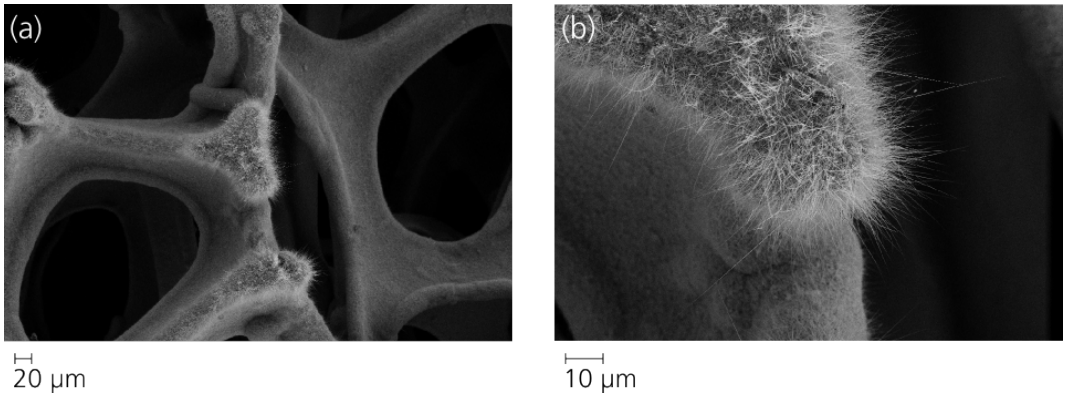

Figure 5.10: Scanning electron microscope images nanowire SnO_2 deposited via CVD on porous nickel foam.

The left SEM image display an overview of the porous foam structure where the SnO_2 nanowires can be seen. The growth of the nanowires is more distinguished at the foam edges and along the pore circumference. The right SEM image shows a magnification of the fine SnO_2 nanowires. It can be seen that they are several micrometers in length, but they do not really contribute to filling the porous structure as was seen with some of the cathode coatings in chapter 4. A finer pore structure of the foam would probably be better suited, unfortunately most commercial nickel foams have rather large pores. It can also be concluded from the SEM images that the SnO_2 nanowire growth is not homogeneous, and several areas will reveal the NiO structure, thus a double anode effect will be very likely and confirmed by the electrochemical measurements.

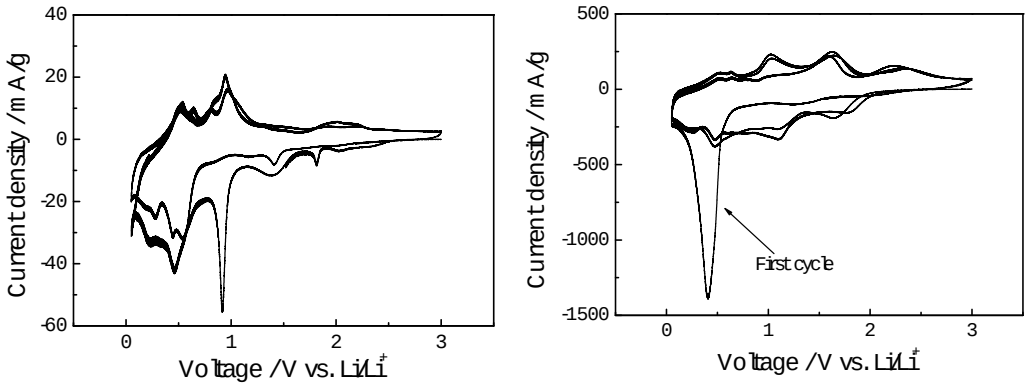

Figure 5.11: Cyclic voltammograms of the SnO_2 deposited on nickel foam (a) SnO_2 nanowires on pure nickel foam (b) SnO_2 nanowires on thermally treated nickel foam (Ni/NiO).

Figure 5.11 displays the cyclic voltammetry of the two SnO_2 nanowire samples deposited on porous nickel foam, cycled from 3.00 - 0.01 V with a sweep rate of 0.1 mV/s. In figure 5.11(a) the CV of SnO_2 on pure nickel foam is seen. The resemblance to SnO_2 on Cu-foil as seen in figure 5.2 is apparent, and any additional effects from the nickel foam cannot be seen. The characteristic transition peak at 0.9 V is present, along with the lithiation and delithiation peaks from 0.5 - 0.01 V. Figure 5.11(b) displays the CV of the SnO_2 nanowires on the thermally oxidised nickel foam. The relatively thick layer of NiO, obtained by thermal oxidation for 3 hours at 550 °C, gives rise to a CV that resembles more that of NiO alone than SnO_2. The irreversible reduction peak seen at 0.4 V vs. Li/Li^+, can be contributed to the reduction process from Ni^{2+} to Ni^0 (as seen in equation 5.1). In addition, this process is also associated with electrolyte decomposition and the reversible lithium insertion.[85]. However, this irreversible peak is often found in literature at 0.2 - 0.3 V and the shifting of this peak to higher voltages could originate from the SnO_2 influence. In the subsequent cycles one major reduction peak and one oxidation peak, representing the lithiation and delithiation, are often found in literature[47, 82, 83]. Figure 5.11(b) displays multiple redox peaks, hence an indication of mixture of the SnO_2 and NiO activity is seen in the cyclovoltammogram. The ratio of NiO to SnO_2 can also explain that the CV is relatively similar to pure NiO. With a 8.9 % oxide formation[111], a NiO layer of 6.55 mg was calculated, giving a NiO to Sn ratio of almost 2:1. The double quantity of NiO will naturally effect the CV appearance. A

cyclovoltammogram of pure NiO can be found in Appendix C, displayed in figure C.1.

$$NiO + 2Li^{+} + 2e^{-} \leftrightarrow Ni^{0} + Li_2O \tag{5.1}$$

Galvanostatic measurements of the two SnO_2 foam samples were performed, cycled between 3.00 - 0.01 V with a constant current of 100 mA/g. The comparison of SnO_2 on pure nickel foam and SnO_2 on Ni/NiO-foam can be seen in figure 5.12(a).

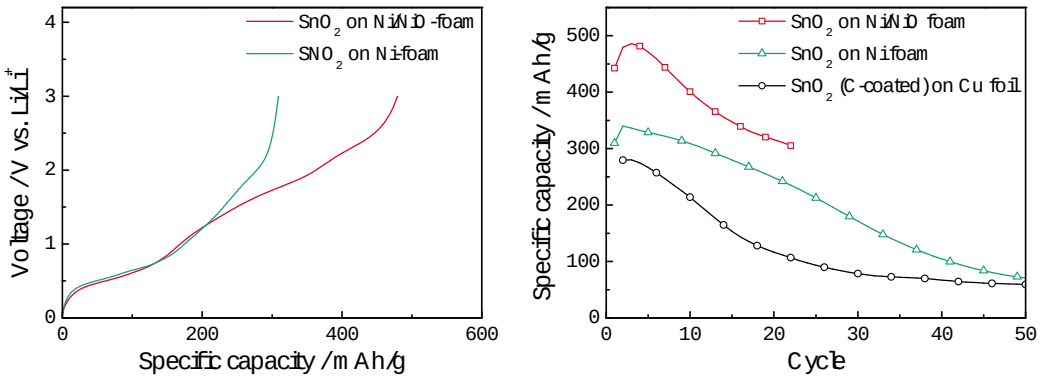

(a) (b)

Figure 5.12: Galvanostatic measurements of SnO_2 on Ni foam; (a) comparing SnO_2 on Ni-foam and Ni/NiO-foam, (b) comparing SnO_2 on nickel foam with SnO_2 on copper foil.

Voltage profiles of the second cycle are seen in figure 5.12(a). SnO_2 deposited via CVD on the thermally treated nickel foam show a considerable advantage over SnO_2 deposited on pure nickel foam. In cycle two, the SnO_2 on Ni/NiO foam gives a specific capacity of 480 mAh/g, compared to only 310 mAh/g of the SnO_2 on pure nickel. The following galvanostatic cycles show the same properties, hence it can be concluded that a SnO_2 deposition on the Ni/NiO foam is of advantage compared to pure nickel. Whether this is due to a better adhesion of the SnO_2 on the NiO surface or due to the double anode effect will have to be examined.

Figure 5.12(b) compares the two samples of SnO_2 on foam with the the SnO_2 deposited on Cu-foil as seen in chapter 5.1. Here the improved SnO_2 concept is shown, the carbon coated SnO_2 as displayed in figure 5.6. It can be noticed that both the foam samples have a higher capacity as the SnO_2 on copper foil, thus it can be concluded that the SnO_2 deposited on nickel foam lead to great improvements in capacity and stability of the electrode. The Ni/NiO foam gives the highest specific

capacity, with a maximum of almost 500 mAh/g, although the capacity is almost reduced to 300 mAh/g after the initial 20 cycles. As can be seen, the SnO_2-Ni/NiO cell could only deliver 22 successful cycles, the reason is the 3-electrode cell setup. As mentioned in chapter 3.3.1, the 3-electrode cells have not proved to be completely air-tight and the cells are not ideal for long-term measurements. However, all foams were measured in the 3-electrode cells as no alternative cells were found, although further work on the foam substrates demand an improved solution for long-term measurements.
It must also be mentioned that the basis of calculating the specific capacity for SnO_2 on pure nickel and SnO_2 on Ni/NiO differs. As pure Ni is not an anode material, only the weight of the SnO_2 nanowires needs to be taken into consideration. For the Ni/NiO substrate, the nickel oxide is also functioning as an anode, thus the weight of NiO is added to the active material, which almost triples the active loading for the Ni/NiO sample compared to pure nickel. However, it is not examined how much of the nickel oxide layer is available for electrochemical reactions. Figure 5.10 showed a rather uneven deposit of SnO_2, thus confirming that NiO will also react in the electrolyte, although the quantification of this remains. Considering the complete NiO-mass to the active part and therefrom calculate the specific capacity in $mAh/g_{\text{active material}}$ is excessive, although a fairer solution was not found. With this in mind, the specific capacity of SnO_2 on Ni/NiO would increase when the contributive part of NiO was known.

This chapter has illustrated the great improvement of depositing SnO_2 on porous nickel foam instead of using a traditional Cu-foil as substrate. After 20 cycles the specific capacity of SnO_2 on Ni/NiO remained at 315 mAh/g, whereas the capacity of the carbon coated SnO_2 on Cu-foil was only 115 mAh/g, resulting in a capacity increase of 200 mAh/g. The possibility of examining the systems on a long-term basis was not possible at the time, due to the geometry of the foam cells and their need for the 3-electrode cells. However, the tendency of this progress is clearly seen, and multiple experiments confirmed this tendency. Despite the great improvement with SnO_2 on foam substrates, the capacity loss seen in the first cycles, both in figure 5.12(b) and 5.6 for the standard SnO_2 samples, gave rise to concern. The capacity loss originates from irreversible chemical reactions leading to structure changes in the first cycles, as seen and examined in chapter 5.1.1, and the need for a better

framework was discussed.

In addition, the wanted stabilising effect of the Li_2O phases that form upon the $SnO_2 \rightarrow Sn$ transition as seen in equation 2.4 was not observed. It would be energetically more favourable to utilise pure tin instead of SnO_2 as the starting material. Pure tin as anode material has a theoretical capacity of 994 mAh/g, even higher than for SnO_2 (781 mAh/g).[11] The main irreversible peak seen in the cyclic voltammogram of SnO_2 at 0.9 V (figure 5.2) contributes to reducing the overall capacity as well as subjecting the cyclability. As the SnO_2 nanowire concept had not proven to be an ideal solution for Sn-containing anodes, other solutions were discussed. The importance of a backbone structure, a buffering matrix was stressed and new concepts were developed. The Sn-containing anode developments are described in chapter 5.2.

5.2 Tin - carbon nanofibers

As seen in chapter 5.1, all SnO_2 nanowires underwent a massive expansion upon cycling, and the nanowires alone could not handle the large volume change. Several improvements were made, by using other nanowire concepts or changing the current collector to improve adhesion and add a second anode material (NiO). However, the initial capacity loss was concerning, and new developments necessary. The Sn anodes were no longer to be synthesised as wires, but rather as spheres or particles deposited on a carbon matrix. The matrix consists of carbon nanofibers which work as a framework or backbone for the expanding Sn particles. This gives the electrode sufficient volume for expansion without the collapse of the structure with cycling.

The newly synthesised tin - carbon nanofibers (Sn-CNF) were produced via electrospinning at the University of Cologne as described in chapter 3.1.3. Electrospinning is a promising technique for the production of nanostructured electrode material due to the facile control of the fiber morphology and possible scalability of the process. Electrospinning also has the ability to form in-situ carbon containing composite fibers, with the right precursor particles in the spinning solution. The resulting fibers do not contain any binder or other additives and the carbon nanofibers enhance the conductivity of the electrode.[112, 113] The standard parameters used for electrospinning

are seen in table 3.5. A scanning electron image of the new Sn-CNF structure can be seen in figure 5.13.

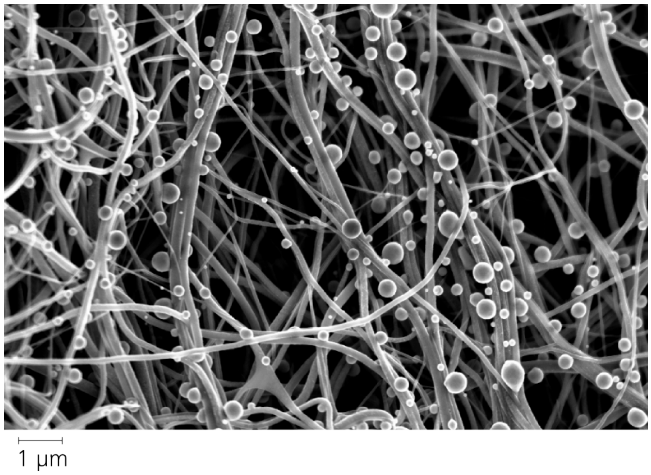

Figure 5.13: Scanning electron microscope image of the initial Sn-CNF sample.

The spheres in figure 5.13 are pure tin particles, and the fibers are of carbon. These findings were also confirmed with EDS, which also excluded the presence of impurities, although small amounts of SnO might still be present in the sample. The initial Sn-CNF samples were produced with 68 wt% Sn and 32 wt% C. The Sn content was confirmed at the University of Cologne via EDS where a different substrate holder was used that did not contain oxygen or carbon, thus giving a more exact value of the Sn content.

The Sn-CNF samples proved to be light and flexible, and the first batch of samples had an average loading of 2.30 mg/cm^2. As the samples were electrospun on a removable substrate, a current collector had to be attached to the sample. Two options proved feasible, first a copper foil of the same size as the punched electrode was added and attached in the Swagelok®-assembly. The spring pressure in the Swagelok®-cell supplied adequate contact between electrode and current collector. The second option utilised a sputtering technique to deposit a thin copper layer on the electrode. However, this technique proved relatively time-consuming and later experiments (figure 5.16(b)) proved that it was also not more efficient than adding a punched copper foil. A scanning electron microscope image of a Cu-sputtered Sn-CNF sample can be seen in figure C.2 in Appendix C.

As the new Sn-CNF samples contained large amounts of carbon, a new theoretical capacity had to be calculated. The theoretical capacity of pure Sn is 994 mAh/g, however, the presence of carbon nanofibers would reduce the overall capacity and the CNFs had a theoretical capacity of its own. The synthesised carbon nanofibers consisted mostly of a amorphous carbon based mixture, where the exact theoretical capacity was not known. Assuming that the CNFs could intercalate as many lithium-ions as graphite, the theoretical capacity would be 372 mAh/g. This gives a calculation for the theoretical capacity as seen in equation 5.2. However, the synthesised CNF being a mixed carbon material, the specific capacity cannot reach the theoretical value of graphite. Nevertheless, 372 mAh/g was used to calculate an approximate theoretical capacity. (The specific capacity of pure CNF was measured at a later stage and can be seen in figure 5.20(b).)

$$32\% \cdot 372\text{mAh/g} + 68\% \cdot 994\text{mAh/g} = 795\text{mAh/g}_{C+Sn} \tag{5.2}$$

A cyclic voltammogram of the assembled Swagelok®-cell was performed, cycled between 3.00 - 0.01 V with a sweep rate of 0.1 mV/s (figure 5.14).

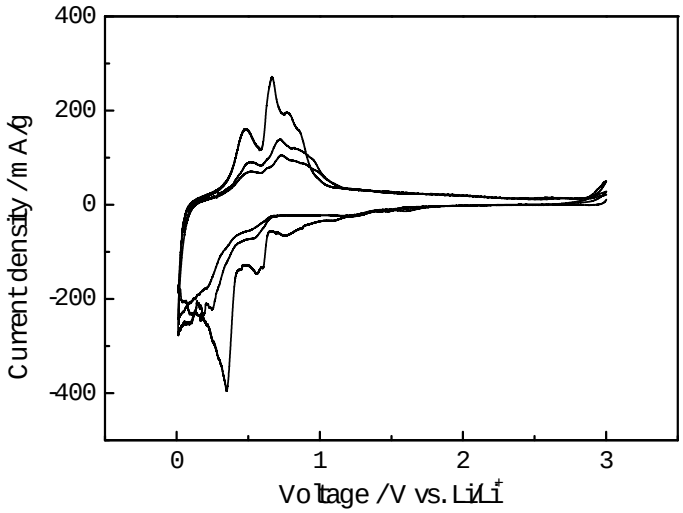

Figure 5.14: Cyclic voltammogram of the initial Sn-CNF sample.

The CV-measurement of the Sn-CNF sample shows similar characteristics as the SnO_2 nanowires (seen in chapter 5.1) with one major exception; the transition peak assigned to the reduction of SnO_2 at 0.9 V is, as expected, not present. However, the

first cycle reflects irreversible processes related to reduction of solution species which form passivating surface films on the carbon fibers.[114, 115] In the subsequent cycles, a more reversible behaviour is observed. Two waves at 0.53 and 0.25 V vs. Li/Li^+ can be seen, attributed to lithium alloying with tin, forming Li_xSn alloys. This reduction of Sn is followed by two oxidation peaks in the anodic scan at 0.53 and 0.74 V vs. Li/Li^+, related to the delithiation of Li_xSn.

The tin - carbon nanofibers were also galvanostatically measured, cycled between 3.00 - 0.01 V with a constant current of 100 mA/g. The charge/discharge behaviour of Sn-CNF, as well as the coulombic efficiency can be seen in figure 5.15.

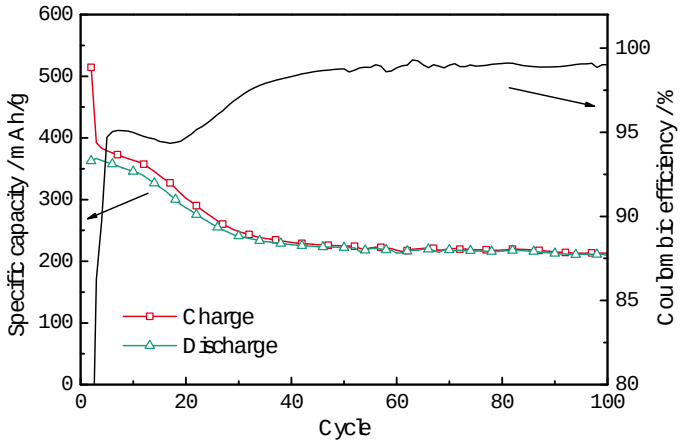

Figure 5.15: Cyclic behaviour of the initial Sn-CNF sample.

The initial Sn-CNF sample is seen to have a maximum discharge capacity in the first cycle of 360 mAh/g which then drops to about 230 mAh/g and stabilises after some 35 cycles. After stabilising at this capacity, the coulombic efficiency increases to a level of 99 % and remains constant for the following cycles. The first-cycle capacity loss is often observed in literature reviews, and is attributed to the decomposition of electrolyte, formation of the solid electrolyte interphase (SEI) at the high surface of the CNF and decomposition of possible traces of SnO_2 or SnO in the composite.[16, 22, 46, 113, 115, 116]. Y. Yu et al.[114] also describes the process of lithium intercalation in hollow carbon nanofibers, where it is said that the de-alloying of lithium in energetically disadvantageous positions leads to a lower capacity in the first cycles. The specific capacity seen in figure 5.15 is based on the entire electrode mass, i.e. both of the carbon nanofibers and of tin. This must be kept in mind when

comparing the capacity of the sample with literature reviews as these are often based purely on the mass of Sn, which would increase the specific capacity. However, the contribution of pure CNF will be discussed later (chapter 5.2.1).

As seen in the cycle behaviour (figure 5.15) the Sn-CNF sample stabilises at about 230 mAh/g; a large disagreement with the calculated capacity of 795 mAh/g, which leaves room for improvement with the Sn-CNF samples. However, the initial Sn-CNF sample can be compared with the previous SnO_2 to quantify a possible improvement with the carbon matrix. Figure 5.16(a) compares the carbon coated SnO_2 (as seen in figure 5.6) with the new Sn-CNF sample.

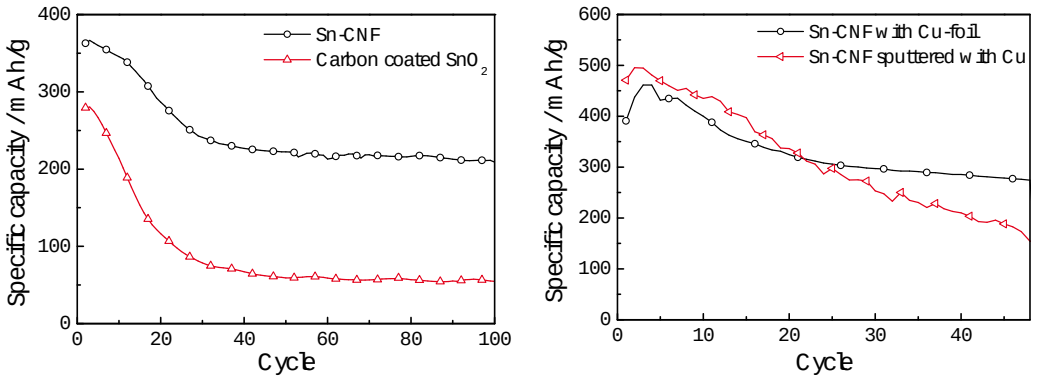

Figure 5.16: Galvanostatic measurements of the initial Sn-CNF sample; (a) comparing Sn-CNF with the carbon coated SnO_2 and (b) comparing method of current collector; Cu sputtering vs. Cu foil.

It can be seen in figure 5.16(a) that even the initial Sn-CNF sample achieves a great improvement to the best-performing SnO_2 sample on Cu-foil. Where the carbon coated SnO_2 stabilises after 30 cycles at 60 mAh/g, the Sn-CNF lies at a plateau of over 200 mAh/g. Thus a successful improvement of the Sn-based anodes is observed and the function of the carbon nanofiber matrix is confirmed. However, as stated above, the disagreement with the theoretical capacity of the Sn-CNF is too large, and further optimisation is necessary. With this in mind, the contacting of the current collector (as mentioned above) was examined. Two options were suggested, either a direct contacting in the Swagelok®-cell with a punched Cu-foil of the same size as the electrode or copper sputtering on the electrode surface. Both options were tried, and the comparison in terms of cycle behaviour can be seen in figure 5.16(b).

The Cu-sputtered sample shows the better capacity in the initial cycles, however, the capacity retention is lower. After 22 cycles the Sn-CNF sample with directly contacted Cu-foil appeared more stable with a capacity of 285 mAh/g after 40 cycles. The experiment was repeated with similar results. As the Cu-sputtering proved no major advantage and this was the more time-consuming process, a standard was set with using a punched Cu-foil as current collector for the remaining Sn-CNF samples. It should also be noted that the influence of copper sputtering vs. directly contacted copper foil could be examined more exactly via electrochemical impedance, where the material resistance can be further understood. However, the experiments with the two current collector approaches applies only for a smooth electrode surface. The reproducibility and appearance of the Sn-CNF samples will later be discussed, this primary choice of current collector might differ for electrodes that are thicker or with different surface structure. One important issue can be seen when comparing the two graphs in figure 5.16. Both black curves with circular symbols represent two Sn-CNF samples of the same batch, however, as can be noticed, the specific capacity varies quite remarkably. While the Sn-CNF sample in figure 5.16(a) stabilised at around 230 mAh/g, the Sn-CNF sample with Cu-foil in figure 5.16(b) obtained a specific capacity of 285 mAh/g after 40 cycles. This relatively large difference in specific capacity within one batch, implied problems with electrode reproducibility.

A new focus on optimising the Sn-CNF anode was chosen. Several parameters had to be varied, optimised and understood. For once, the reproducibility of an electrode within a single batch had to be improved, next the electrode appearance had to be improved as the flexibility and the thickness of the electrodes also varied within a batch. The optimal Sn-content should also be examined, as a better stability with higher carbon content competes with the higher capacity with a higher Sn-content. Also, the contribution of the carbon nanofibers alone was to be examined. Chapter 5.2.1 illustrates the changes and improvements of the Sn-CNF samples.

5.2.1 Optimising the Sn-CNF anodes

By varying the spinning solution, for example adding more of the tin(IV)ethoxide, the Sn content could be increased. The standard composition of the spinning solution is seen in table 3.5 in chapter 3.1.3. Simultaneously, the calcination parameters could

be varied. Adjusting the pressure and calcination temperature lead to changes in structure and morphology of the electrode. Further information on the variation and changes done to improve the Sn-CNF can be found in the PhD thesis of R. von Hagen, University of Cologne[60]. Some examples of different morphologies can be seen in figure 5.17.

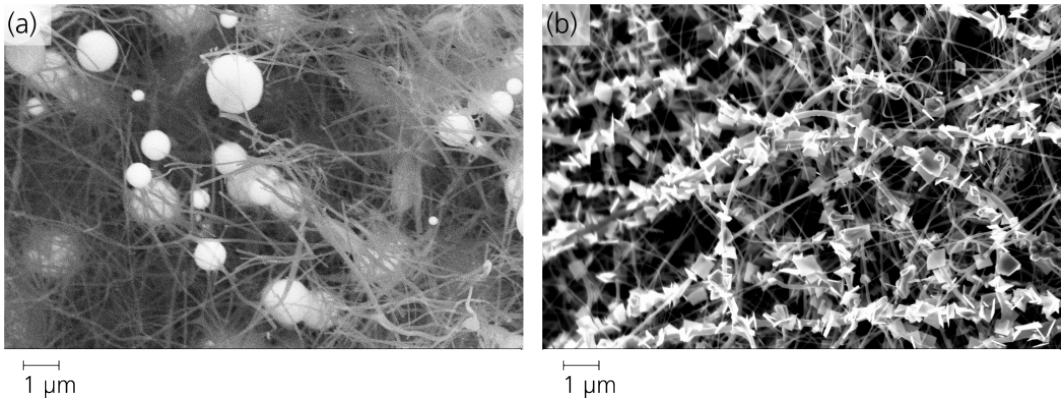

Figure 5.17: Various Sn-CNF structures illustrated with scanning electron microscopy; (a) thin carbon nanofibers with Sn particles and (b) carbon nanofibers with Sn plates.

Figure 5.17(a) shows a Sn-CNF sample where the Sn content was reduced to 50 % while the other parameters where kept constant. Very fine carbon nanofibers are observed, surrounding quite large Sn particles in the range from 100 nm to μm-particles. The right SEM image (figure 5.17(b)) displays a Sn-CNF structure where the calcination was performed at 685 °C for 1 hour while the amount of (Sn(IV)$(OEt)_4$) was kept constant (see chapter 3.1.3). The reduced calcination time resulted in plate-like Sn compounds in μm range. It was discovered via SEM and EDS that a longer calcination time turned these plates to the round particles seen in figure 5.17(a) and that the plates were a pre-phase to the pure Sn particles that also contained traces of SnO. Subsequent synthesis focused on obtaining Sn particles without SnO traces.

The spinning solution was changed to synthesise a series of samples with increasing tin content. The content of Sn was varied between 40 and 75 wt%, and the produced samples electrochemically characterised. Thus the trade-off optimum could be found. As pure tin has a higher theoretical capacity (994 mAh/g), a higher Sn-content would increase the specific capacity of the electrode. However, reducing the carbon matrix would result in a reduced stability as the Sn-particles need a backbone to

expand upon cycling without collapsing. A too high content of carbon, would again lead to a much lower specific capacity as the theoretical capacity of carbon is lower (372 mAh/g for graphite). An ideal trade-off content between Sn and CNF could be determined by comparing the cyclic behaviour in figure 5.18. All samples were cycled between 3.00 and 0.01 V vs. Li/Li^+ with a current density of 100 mA/g.

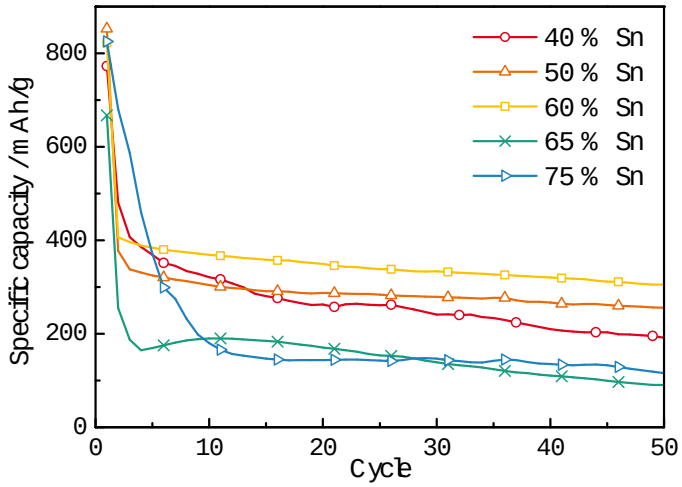

Figure 5.18: Cyclic behaviour of Sn-CNF with varying Sn content.

Variation of the Sn-content shows that 60 wt% of Sn gives a higher capacity. In figure 5.18, the sample with 60 % Sn stabilises after a few cycles and reaches 380 mAh/g. It can be seen that increasing the Sn content above 60 wt% leads to a collapse of the structure as the samples with 65 and 75 wt% obtained the lowest capacities. The minimised carbon backbone cannot absorb the volume expansion of the Sn particles. The sample with the highest stability proved to be with 50 wt% Sn, obtaining a specific capacity of 320 mAh/g after five cycles, and having the better capacity retention in the following cycles.

Due to differences in the electrospinning method, not all electrodes within a batch are of equal thickness and appearance as discussed above. An electrode with higher loading has naturally more active material, and would normally supply a higher capacity. However, the thicker electrodes seemed to consist of several thinner layers of Sn-CNF, and the contacting between these layers was not ideal. The rather porous structure lead to a reduced flexibility of the electrode, and without a good material contact, the lithium diffusion paths increased along with the reduced electrical con-

ductivity. Figure 5.19(a) shows a variation of the loading and the cyclic behaviour thereof.

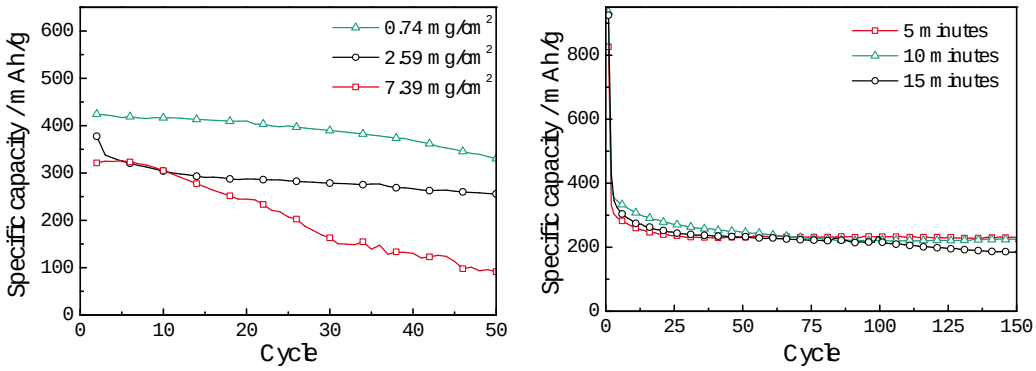

(a) (b)

Figure 5.19: Galvanostatic measurements of the improved Sn-CNF samples; (a) Differences in loading and (b) differences in deposition time.

Ideally, since all measurements in figure 5.19 are based on the specific capacity (mAh/g), all curves should obtain similar values. As this is not the case in figure 5.19(a), a loading dependency can be confirmed. Clearly, a lower loading of the Sn-CNF obtained a higher and more stable capacity (figure 5.19(a)). It could be observed that the samples with a lower loading were thinner, more flexible and had a smoother surface. This resulted in an advanced electronic contact between electrode and current collector, smaller lithium diffusion distances and thus an improved capacity. The samples with the higher loading were thicker, more brittle, and, as seen in figure 5.19(a), had a lower capacity retention. Thus, to improve the capacity of the Sn-CNF electrodes, the production method was changed to obtain rather thin samples.

The deposition time was also varied to study the differences in loading and the following electrochemical results. The electrospinning time was set to 5, 10 and 15 minutes, and the resulting samples were studied. The cyclic behaviour of the three samples is seen in figure 5.19(b). The 5, 10 and 15 minutes deposition time lead to a loading of 0.98, 3.32 and 3.89 mg/cm^2, respectively. Changing the deposition time from 5 to 10 minutes increased the loading extensively, while increasing the deposition time further five minutes only lead to a minor loading increase. However, as seen in figure 5.19(b), a deposition time variation did not lead to major differences in the cyclic behaviour. The sample with 10 minutes deposition had a slightly higher

capacity of about 270 mAh/g for the first 50 cycles, and the sample with 15 minutes deposition time averaged a bit lower for the last 50 cycles. A more relevant fact was the appearance of the electrodes. Despite the differences in loading due to deposition time, all samples remained flexible with a smooth surface, thus providing the electrical contact needed. Once again, the issue of electrode appearance proved to be more important than thickness, loading or deposition time. Producing an electrode with equal thickness, consisting only of one dense layer, with a smooth surface seemed to be the solution to optimising the Sn-CNF electrodes.

The matrix of nanofibers consisted of different amorphous carbon phases[60]. Previously it was assumed for calculations of the theoretical capacity that the fibers had similar properties as graphite with a theoretical capacity of 372 mAh/g. However, with the mixed carbon, this is certainly not the case. It was important to examine the capacity contribution of the carbon nanofibers alone, thus new samples of CNF without Sn were prepared. A different spinning solution without the Sn-precursor also gave a different structure of the calcinated CNFs. They were less flexible and shrunk up to 70 %, thus only samples of 0.5·0.5 cm^2 were possible. The samples were nonetheless assembled in Swagelok®-cells and electrochemically measured. Figure 5.20 illustrates both a scanning electron microscope image of the fibers, as well as the cyclic behaviour of the CNFs directly compared with the previously measured Sn-CNF. The fibers seen in figure 5.20(a) appear a bit thicker than the nanofibers decorated with Sn-particles (figure 5.13) and they are not as straight, but tend to curl up. The thickness of the fibers vary from a few nanometer up to 0.5 μm. A CV of the pure carbon nanofibers is displayed in Appendix C, figure C.3.

An initial cyclic voltammogram of the CNF sample displayed a typical curve of amorphous carbon with SEI-formation in the first cycle and Li^+-insertion between 1.0 - 0.01 V in the subsequent cycles. However, as the goal was to quantify the capacity contribution of CNF, the more important electrochemical examination is seen in figure 5.20(b). The pure carbon nanofibers obtained a maximal capacity of 295 mAh/g after 3 cycles, however, the stability of the material was quite low, thus, after 50 cycles the capacity was reduced to 88 mAh/g. In comparison, the optimised Sn-CNF obtained a capacity of 330 mAh/g after the 50 cycles. It was feared that the contribution of the CNFs was high, i.e. that after several cycles, the Sn had expanded

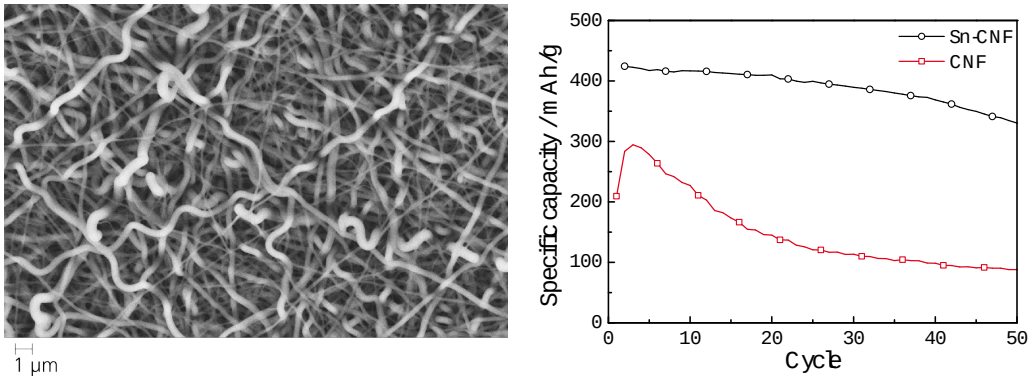

(a) (b)

Figure 5.20: Measurements of pure carbon nanofibers; (a) Scanning electron microscopy of CNF and (b) comparison of cyclic behaviour of CNF vs. Sn-CNF.

to such an extent that it lead to partial collapse of the material, and the remaining capacity observed after the initial loss, originated from the CNF alone. However, this comparison proves the opposite. After several cycles, the carbon nanofibers contribute to about 25 % of the overall capacity, thus also confirming the composite effect of the carbon nanofiber matrix.

As a measure of the rate capability of Sn-CNF, measurements with various current densities were conducted. From the experiments, the specific capacities as a function of the current density are plotted in figure 5.21.

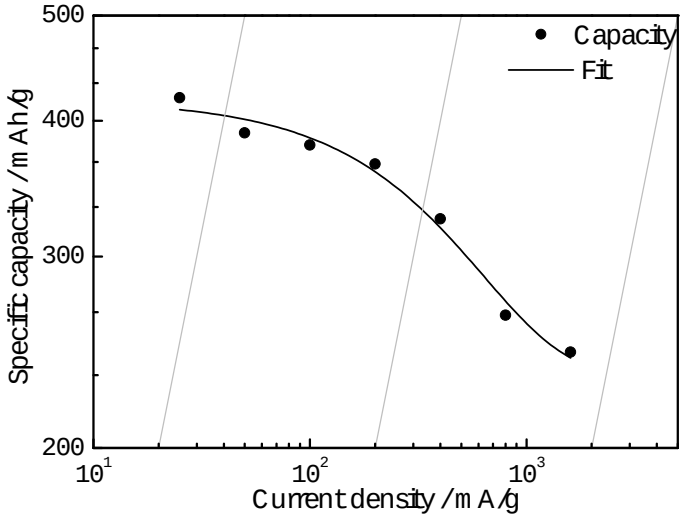

Figure 5.21: Specific capacity as a function of current density for the Sn-CNF.

As mentioned in chapter 2.6.2, varying the current density or the C-rate of the measurements can give information about the cell's load capability and the kinetics of the material. As seen in figure 5.21 the specific capacity decreases as expected with an increasing current density. With a lower discharge time, the time for lithium diffusion and charge transfer is not adequate, and the cell cannot supply the same capacity. A current density of 25 mA/g, which is four times slower than the standard measurement using 100 mA/g, gives a capacity over 420 mAh/g. However, even a much higher current density of 1600 mA/g results in a specific capacity of almost 250 mAh/g. When the cell is discharged 16 times faster than normal, it can still deliver sufficient discharge capacities, thus demonstrating the excellent load capability of the Sn-CNF anodes.

This chapter about the Sn-CNF anodes has proven the success of integrating a carbon framework into the structure. The carbon nanofibers gave enough support and volume for the great expansion of the Sn particles upon Li-alloying. A new deposition technique, electrospinning, has also showed convincing properties, such as scalability, no need for binder and self-supporting, flexible electrodes. The very first Sn-CNF sample was seen to achieve a higher capacity and stability over the carbon coated SnO_2, still the Sn-CNF samples had room for improvement. The Sn-content was varied between 40 and 75 wt%, and an optimum found at 60 wt% Sn. The structure of the electrodes was looked into, with regards to the deposition time, loading and choice of current collector. The contribution of the carbon nanofibers without Sn particles was determined to 25 % of the overall capacity for the optimised Sn-CNF samples. And finally, reproducible, stable Sn-CNF electrodes were produced with excellent rate capability and fast kinetics, showing the overall improvement of the Sn-CNF samples.

5.3 Summary and discussion

In this chapter several Sn-containing anode materials have been presented. SnO_2 anodes deposited via CVD on both copper foil and porous nickel foam were fabricated, in addition to tin - carbon nanofibers via the electrospinning method. The work with the Sn-containing anode materials has been performed in close cooperation with several colleges from the University of Cologne, where the anode synthesis took place.

This thesis has focused on the electrochemical characterisation of the materials, as well as developing new concepts for improving the anode materials.

Initially, SnO_2 nanowires were synthesised with the use of chemical vapour deposition. The thin nanowires were meant to give enough free volume for the known expansion of Sn during lithiation. In addition, during the transition from SnO_2 to Sn, a by-phase (Li_2O) was formed, that was supposed to act as a supporting matrix. Several new nanowire concepts were developed (as seen in figures 5.4 and 5.5) to improve the stability, the electronic conductivity and increase the surface area of the electrodes. However, as seen in chapter 5.1, the SnO_2 nanowires could not maintain the initial high capacity, and the capacity drop over the first cycles could not be ignored. The new concepts, including surface reduction of SnO_2, brush-like structure and carbon coating, made significant improvements, although, it was seen that the nanowire structure could not support the large volume expansion (figure 5.6). The large structure change upon charging was explicitly examined with the use of ex-situ analysis (chapter 5.1.1). The known volume change of up to 300 % was observed, however, the nanowires did not regain its original size and shape upon lithiation. Within a few cycles the fine 3-dimensional structure was reduced to a 2-dimensional structure with longer lithium diffusion paths and reduced electronic conductivity as the adhesion to the copper current collector failed.

SnO_2 samples were deposited on porous nickel foam, where two main effects were observed. It was confirmed with the cathode material in chapter 4.1 that the thermally oxidised nickel foams obtained a thin layer of nickel oxide, which gave a much better adhesion to the electrode material. Secondly, the thermally obtained NiO is itself an anode material, and as the deposited SnO_2 was not a dense layer, a double anode effect could be observed. A quantification of the NiO contribution was not possible, it was presumed that the entire nickel oxide layer contributed. An exact value of the NiO available to electrochemical reactions would facilitate the understanding of the double anode effect. Depositing SnO_2 on a thermally treated nickel foam increased the overall capacity of 200 mAh/g (figure 5.12(b)), and it was also proved that depositing SnO_2 on untreated nickel foam did not have the same effect (figure 5.12(a)). However, the foam substrate had some limitations with measurement setup and the choice of a measurement cell was confined to the 3-electrode cell. With this

in mind, and the necessity of a more supporting framework for the volume expansion new Sn-containing anodes were developed.

The third development of the Sn-containing anodes included the tin - carbon nanofibers synthesised via the much promising electrospinning method. Thin, nanometer-range, self-supporting nanofibers constituted a matrix for the Sn-expansion upon cycling. The Sn was found in particle form, decorated on and between the carbon nanofibers (seen in figure 5.13). The initial Sn-CNF sample achieved a much higher specific capacity than the SnO_2 on Cu-foil, and the Sn-CNF samples were further improved. An optimum Sn-content was found at 60 wt% Sn (figure 5.18), with just the right balance between the high capacity of Sn versus the stability given by the CNF matrix. Two options for the current collector were examined, either the attachment of a punched copper foil or Cu-sputtering. In addition, the influence of morphology, electrode structure, loading of electrode material and the deposition time of the electrospinning were examined. The carbon nanofibers were synthesised without Sn particles to investigate the contribution of the carbon phase on the overall capacity (figure 5.20). The capacity contribution of the pure CNFs was found to be about 25 % of the overall capacity of Sn-CNF. A final comparison of the three Sn-containing anode materials can be seen in figure 5.22.

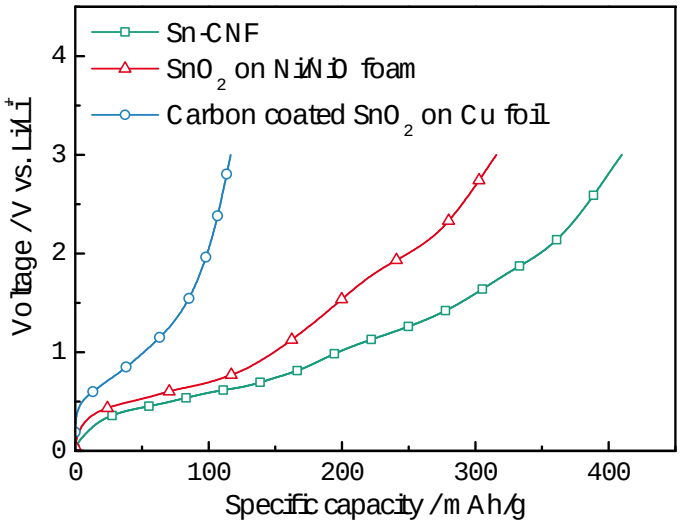

Figure 5.22: Comparison of the three Sn anode materials investigated in this thesis (voltage profiles of lithium extraction in the 20th cycle).

All samples were cycled with a current density of 100 mA/g, and the voltage profiles

seen in figure 5.22 are taken from the 20th cycle to investigate the capacity after the initial-loss phase. It can clearly be seen that the Sn-CNF sample obtained the highest capacity of the three samples. For the Sn-CNF, the SnO_2 on Ni/NiO foam and the carbon coated SnO_2 on Cu-foil the specific capacity in the 20th cycle are 410, 315 and 115 mAh/g, respectively. The Sn-containing anodes have proven to be promising substitutes for the commercially used graphite, mainly due to the improved theoretical capacity. The most encouraging material is the Sn-CNF, where a practical capacity of over 400 mAh/g can compete with the theoretical value of 372 mAh/g for graphite. The large expansion of Sn is also observed in the Sn-CNF samples, although they stabilise more rapidly, needing only a few cycles before a plateau is reached. And as seen in figure 5.21, the rate capability of Sn-CNF is excellent, with adequate capacities obtained with a 15 times higher discharge rate. The background of calculating the specific capacity has to be mentioned once more. Whereas in most publications, the specific capacity in mAh/g would be based on the active mass of only Sn, it is here based on the entire electrode, of both Sn and the CNF. It was proven that the CNF contribute to about 25 % of the overall capacity, and it seemed wrong to extract this value. However, the capacity of Sn-CNF would increase by 40 % when only the active mass of Sn would be considered.

With a maximal obtained capacity of about 400 mAh/g for the Sn-CNF, the disagreement with the theoretical capacity still exists. This is mainly due to the capacity loss in the first cycles, with the formation of the SEI-layer and the structure changes that take place. Several other concepts of Sn-containing anodes have proven to be promising, however, with the limited time-frame and the scope of the KoLiWIn-project, not all concepts could be examined. A few will be mentioned as further possibilities and eventual further work.

Combining several Li-alloying components was mentioned in chapter 2.3, and interesting work would include silicon particles with the existing tin particles. As silicon has a much higher theoretical capacity (4200 mAh/g with $Li_{4.4}Si$), it has become one of the most interesting new anode materials. However, the volume change upon cycling is still the greatest challenge for using Si. A backbone structure that would support the large expansion will have to be developed when utilising Sn, Si or the combination of the both. Work with composite anodes of both Si and

Sn was performed within the KoLiWIn project, however, it was not a part of this thesis.

Another possibility of improving the stability of the Sn-anodes would be to integrate the particles within the carbon fibers. Several literature reviews report of success with hollow structures encapsulating Sn particles.[16, 114, 116] This technology could be extended to core-shell solutions with or without voids that supply free volume for the expansion, as well as to hollow wires, tubes or coaxial fibers. However, the fabrication process must be taken into account. For a possible commercialisation, ease of preparation and scalability are two very important factors, and the electrode fabrication should ideally be a one-step process.

Chapter 6

Lithium chalcogenidometalates

As mentioned in the introduction the thesis a brand new network of Li^+-inserting quaternary chalcogenidometalates was synthesised within the KoLiWIn-project at the Philipps-Universität Marburg. As a new material group for lithium-ion batteries it was not certain if Li-ions could be inserted into the structure, in what potential region this would happen or how stable and reversible the Li-uptake was. This had to be determined using mainly electrochemical measurement methods (described in chapters 2.6.1 and 2.6.2) as the initial structural characterisation was performed at Philipps-Universität Marburg. More details about ionic conductivity and characterisation of single-crystals can be found in the PhD thesis of T. Kaib[117].

6.1 $Li_4MnSn_2Se_7$

Due to lack of large amounts of the $Li_4MnSn_2Se_7$ material, (delivered as crystals) electrodes were fabricated from the crystals and further characterisation was performed with the electrodes itself. The crystals were ground and the resulting powder mixed and made into a slurry as described in chapter 3.1. Table 3.1 describes a typical slurry composition (as used for the cathodes in chapter 4), although the $Li_4MnSn_2Se_7$ slurry was made with only 60 % of active material to save material usage. The resulting slurry was coated on a copper foil via doctor blading (chapter 3.1.2.2). As the material contains the toxic element selenium and the material proved to be relatively air sensitive, all preparation was performed in the glovebox in argon atmosphere. With a standard cell assembly procedure the electrodes would ideally be pressed after punching (as described in chapter 3.3.1), however this was not done

with the $Li_4MnSn_2Se_7$ electrodes due to difficulties to provide the argon atmosphere for this equipment.

6.1.1 Structural data

The unit cell structure of $Li_4MnSn_2Se_7$ can be seen in figure 6.1. The synthesised $Li_4MnSn_2Se_7$ showed a hexagonal diamond structure with several channels suited for Li-insertion.

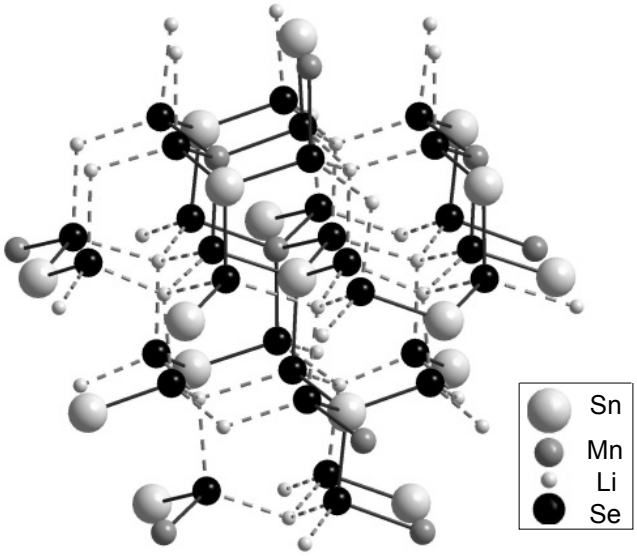

Figure 6.1: The unit cell structure of $Li_4MnSn_2Se_7$ showing a hexagonal diamond structure. The unit cell structure was modeled by the research group of Professor S. Dehnen, Philipps-Universität-Marburg[118]

Further characterisation of $Li_4MnSn_2Se_7$ followed with electron microscopy to examine the microstructure of the material, particle size and distribution. Energy dispersive X-ray spectroscopy (EDS) was used to exclude the presence of impurities. Figure 6.2(a) displays the results of the electron microscopy.

The SEM image shows $Li_4MnSn_2Se_7$ mixed with binder and carbon black coated on a Cu-foil. Some larger particles in the micrometer range can be seen, as well as smaller ones measuring only a few nanometers. It was assumed that the larger particles were the $Li_4MnSn_2Se_7$ powder, and the smaller particles consisted mainly of the carbon black. This theory was confirmed by the EDS measurement of this scanned

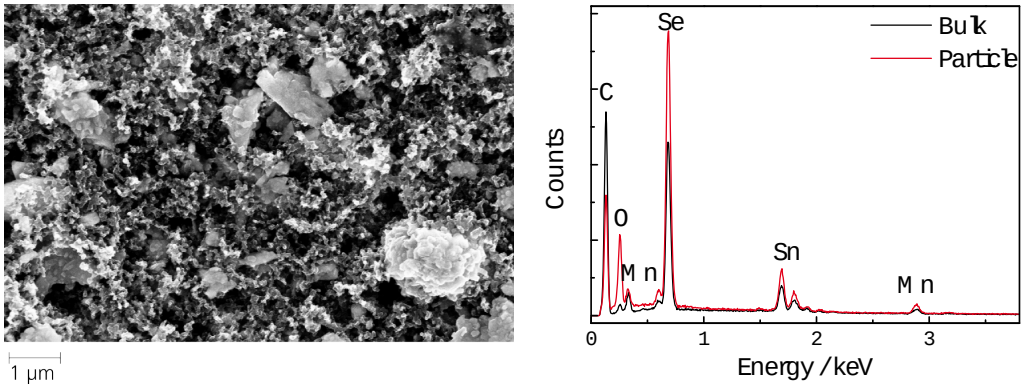

(a) (b)

Figure 6.2: Scanning electron microscopy of $Li_4MnSn_2Se_7$. a) SEM image and b) EDS spectra.

area (figure 6.2(b)) A spectrum of the bulk material was recorded, showing a high carbon content. Another spectrum of the larger particles was recorded, showing a higher content of mainly Se, but also Sn and Mn. This confirms that the μm-particles are $Li_4MnSn_2Se_7$ and the nm-particles are carbon black. The EDS spectra show no signs of other phases present in the sample, thus the existence of impurities can be excluded. The distribution of the larger particles seems adequate and a homogeneous electrode is obtained. Variation of particle size through grinding or other methods was not examined. Further work would include optimisation of particle size and slurry composition.

An XRD analysis was also performed, again of the $Li_4MnSn_2Se_7$ coated Cu-foil. The grazing incidence diffraction (GID) mode on the Siemens apparatus was used to examine the thin film on the Cu-foil and the result is displayed in figure 6.3.

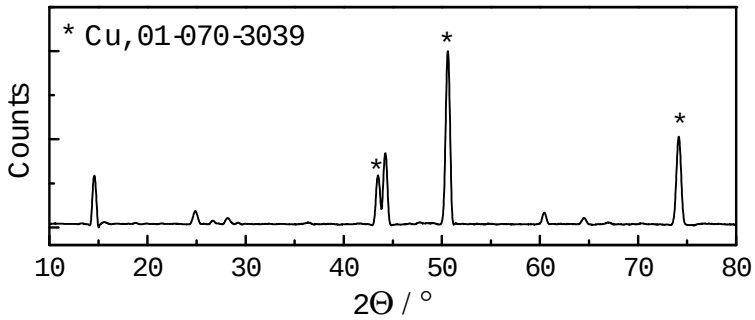

Figure 6.3: XRD of $Li_4MnGe_2S_7$ coated onto copper foil.

As $Li_4MnSn_2Se_7$ has not been previously characterised, there is no literature comparisons, and also no entry in the XRD-software. The peaks at 43.5°, 50.5° and 74.0° can be associated with the Cu-substrate, and these peaks are also more dominant. However, there are other characteristic peaks at 14.5°, 25.0°, 28.5°, 44.5°, 60.5° and 64.5° which cannot be assigned to Cu, thus must arise from the $Li_4MnSn_2Se_7$ coating. A complete characterisation cannot be confirmed, although it can be said that the sample is crystalline, as an amorphous sample would not give such distinct peaks.

After one initial cycle with the Solartron potentiostat, an new XRD was made, resulting in a very different structure than that seen in figure 6.3. The crystalline structure seen above had changed to amorphous, where mainly the Cu-peaks of the current collector remained. This indicates a strong structure change upon cycling as will be discussed in chapter 6.1.2.

6.1.2 Electrochemical characterisation

As previously explained in chapter 2.6.1 a cyclic voltammogram (CV) is a very suited first electrochemical characterisation of a new electrode material as it can be considered as a fingerprint of the material with its individual redox peaks. The CV can also be used to quantify the electrochemical activity, also important when examining new electrode materials.

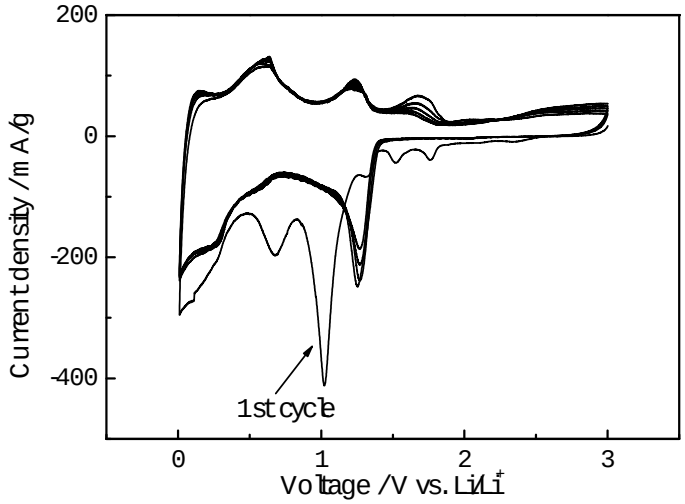

Figure 6.4: Cyclic voltammogram of $Li_4MnSn_2Se_7$ with a sweep rate of 0.1 mV/s.

The $Li_4MnSn_2Se_7$ electrodes were assembled as Swagelok®-cells and cycled in the anode region between 3.00 and 0.01 V with a sweep rate of 0.1 mV/s. The resulting CV can be seen in figure 6.4.

From the CV one can see that the material is indeed electrochemically active and that lithium insertion takes place. Several redox peaks are seen which indicate a step-wise lithium insertion, although exactly how many Li^+ insert into the unit cell cannot be determined at this point. It can also be seen that the first cycle is differing from the later ones. As explained in chapter 2.5.1.1 the first cycle displays several irreversible processes such as the formation of a solid electrolyte interphase (SEI). These processes can be seen in the CV from the irreversible peaks at 1.8 V, 1.5 V, 1.0 V and 0.7 V. Some of the peaks arise from irreversible structure transitions in the material itself while other peaks originate from the SEI-formation. The XRD analysis of a cycled sample revealed an amorphous structure after just one cycle and confirmed that a major structure change took place.

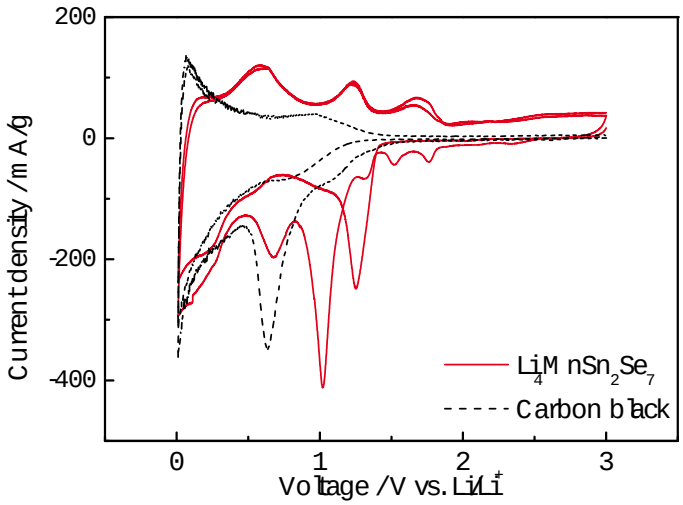

Figure 6.5: Comparison of the cyclic voltammogram of $Li_4MnSn_2Se_7$ and of carbon black.

The measured sample contains about 30 wt% of carbon black, and as carbon black has some capacity of its own when cycled in the same potential range, the influence of carbon black had to be determined. Which CV peaks can be assigned to the carbon black, and which can be assigned to the $Li_4MnSn_2Se_7$? Unfortunately, measurements of pure $Li_4MnSn_2Se_7$ proved difficult with lack of fabricated material, and the material itself was not sufficient electronically conductive. Therefore samples of pure

carbon black were fabricated and assembled via the same methods, and these samples were measured for comparison. Figure 6.5 illustrates the cyclic voltammogram of carbon black and $Li_4MnSn_2Se_7$.

The black dotted line in figure 6.5 shows the CV of the pure carbon black. It can be seen that there is one irreversible peak at 0.6 V in the first cycle indicating the SEI-formation. The main redox peaks of carbon black are close to 0 V, hence these similar peaks found in the $Li_4MnSn_2Se_7$ sample originate from the carbon black content in the electrode. As the other reversible peaks of $Li_4MnSn_2Se_7$ are not seen in the carbon black cyclic voltammogram, it can be concluded that they can be assigned to the $Li_4MnSn_2Se_7$ itself. The quantitative characterisation of $Li_4MnSn_2Se_7$ could rather be determined by galvanostatic measurements (constant current measurements) where the capacity of the material can be directly illustrated (figure 6.6).

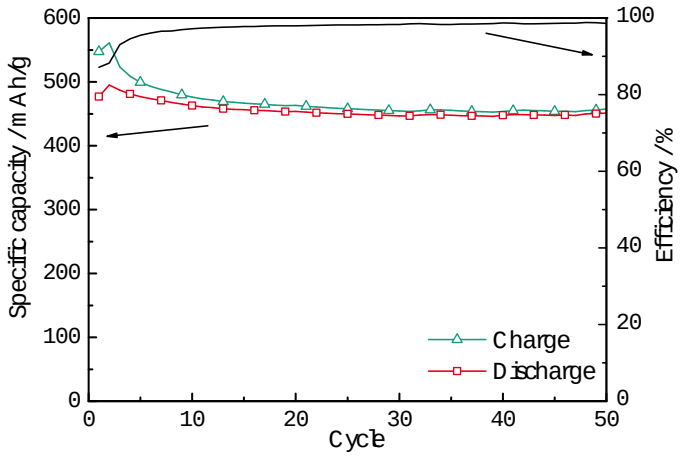

Figure 6.6: Cyclic behaviour of $Li_4MnSn_2Se_7$ measured with a current density of 300 mA/g from 3.0 - 0.01 V.

The $Li_4MnSn_2Se_7$ sample was cycled with a constant current of 300 mA/g between 3.00 V and 0.01 V, and figure 6.6 shows the initial fifty cycles. A specific capacity of over 400 mAh/g is obtained, the discharge capacity equals 420 Ah/g in the first cycle and 401 mAh/g in the 50th cycle, indicating a very good cyclability. The commercially used anode material, graphite, has a theoretical capacity of 372 mAh/g (with LiC_6 composition)[119]. However, this theoretical capacity is in most practical batteries not met, the capacity remains normally below 350 mAh/g. Hence, the newly synthesised $Li_4MnSn_2Se_7$ with a practical capacity of 400 mAh/g for over 50

cycles possess a great advantage over the commercially used graphite.

The specific capacity is often calculated on the basis of the active material alone, meaning that the weight of carbon black and the binder is subtracted before calculating the specific capacity. However, most literature studies do not admit to distinctively use the active mass as calculation basis and some confusion may arise. The specific capacity seen in figure 6.6 is calculated without subtracting the mass of binder and carbon black, i.e. the specific capacity shown is calculated on the basis of the entire electrode weight (minus copper current collector). The electrode contains only 60 % $Li_4MnSn_2Se_7$, thus regarding the specific capacity on the basis of $Li_4MnSn_2Se_7$ alone would definitely increase the specific capacity (over 660 mAh/g), giving the material an even higher advantage over graphite as anode material. However, as can be seen in the cyclic voltammogram in figure 6.5, the relatively large amount of carbon black does influence the capacity of the anode material and it was decided not to subtract the mass of carbon black when calculating the specific capacity. Galvanostatic measurements with pure carbon black were performed to quantitatively determine the influence of carbon black on the overall specific capacity. Samples with pure carbon black obtained a stable specific capacity of about 80 mAh/g, although somewhat higher in the very first cycles. The cyclic behaviour of pure carbon black can be found in Appendix C, figure C.4.

The stability seen in figure 6.6 is also outstanding where the left axis displays the coulombic efficiency (CE). It can be seen that after some cycles the efficiency amounts to 98-99 %. More importantly is also the first cycle loss. Graphite is a very stable anode material, thus it is still the material-of-choice on the anode side, despite its relatively low specific capacity. The Si/Sn-composite anode materials have a very high capacity, theoretically up to ten times higher than graphite, (established in table 2.2) but they are very unstable due to the large material expansion upon cycling. Also the initial capacity loss of Sn-compounds is quite serious (as seen in chapter 5) as most of the capacity gets lost in the very first cycles. The coulombic efficiency in the very first cycle can be as low as 35 % for Si-compounds and with further cycling the electronic contact between the Si particles degrades, resulting in a decrease in capacity.[120] The first cycle CE for $Li_4MnSn_2Se_7$ is 87 %, hence the initial capacity loss of this material is significantly lower than for typical Sn or Si compounds.

Galvanostatic experiments with a varying C-rate were also performed. From figure 6.6 the 1C-rate was determined at 480 mAh/g and the discharge current density was varied between 77 mA/g (0.16 C) and 4923 mA/g (10 C) while the charge current density was set to 100 mA/g. The resulting graph can be seen in figure 6.7.

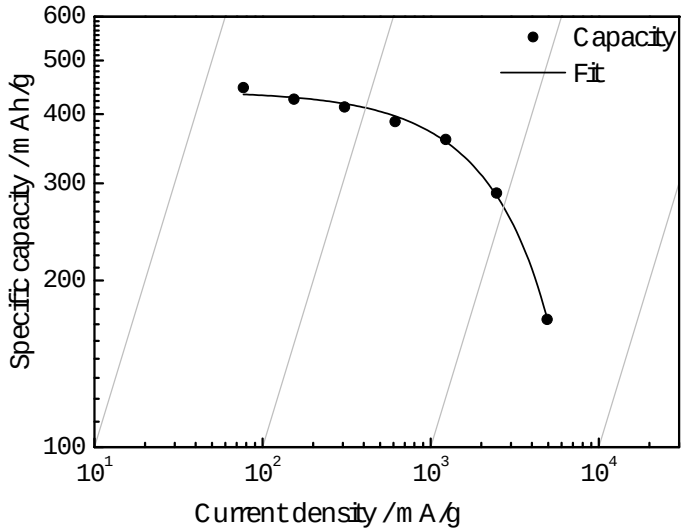

Figure 6.7: Specific capacity as a function of current density for $Li_4MnSn_2Se_7$.

Chapter 2.6.2 explains the benefits of varying the C-rates or current densities for galvanostatic experiments, as the materials load capability and kinetics can be determined. When the C-rate is increased to 10 C it means that the electrode is discharged in 1/10 of an hour (6 minutes), and it can be determined how fast the kinetics of the material is by comparing the specific capacity. As long as the capacity does not drop with increasing current density the cell has enough time for charge transfer and diffusion, and lithium can still be inserted. The $Li_4MnSn_2Se_7$ material obtains a specific capacity of almost 450 mAh/g at 0.16 C (77 mAh/g) and over 400 mAh/g at 1 C (480 mAh/g). The current density is gradually increased up to 10 C (4923 mA/g) where the capacity was reduced to 170 mAh/g. The specific capacity generally decreases with the increase of current density, which is mainly caused by the lower Li^+ diffusion rate.[82] The $Li_4MnSn_2Se_7$ material still shows a very adequate capacity at 5 C, (with 288 mAh/g) confirming the materials excellent load capability.

As supporting information to better understand this newly synthesised Li^+-inserting

quaternary chalcogenidotetrelate compound, Fraunhofer IWM performed several simulations of $Li_4MnSn_2Se_7$. The lithium insertion with two different density functional theory (DFT) methods (LDA and PBE) was simulated. The DFT simulation was based on a 28 atom unit cell, $Li_8Mn_2Sn_4Se_{14}$. The insertion simulation resulted in several energy barriers which could be compared with the cyclic voltammogram in figure 6.4 with great success as most peaks were compliant with the simulated energy barriers. The comparison of simulation (Fraunhofer IWM) and the experimental data can be seen in figure 6.8. The specific capacity seen is based only on the $Li_4MnSn_2Se_7$ material (without the contribution of carbon black), hence the capacity values are higher than reported previously in this chapter.

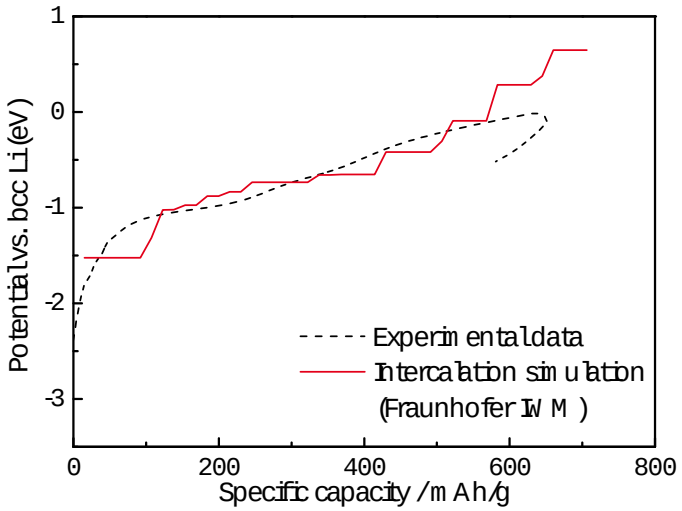

Figure 6.8: Lithium insertion simulation of $Li_4MnSn_2Se_7$, adapted from T. Kaib et al.[121].

There are 28 interstitials in the original unit cell, 14 octahedral, 14 tetrahedral. The simulation showed that a typical insertion of Li^+ does not take place. Filling all interstitials would result in a grave crystal structure change, it was found that the structure can only be stable when filling 10-24 sites with Li^+. The Sn-Mn-Se network is breaking on charging and new Li-Se phases form. The volume change by complete interstitial filling (24 Li^+, $Li_{4+24}MnSn_2Se_7$) was also calculated, resulting in an expansion of over 47 %. However, the insertion of the first 10 lithium-ions per unit cell ($Li_{4+10}MnSn_2Se_7$) gave a smaller volume change of only 17.3 %. The lithium migration was also calculated, found to be equally fast in all directions of the structure, and the migration barrier was roughly 0.5 eV, comparable to that of a

graphite anode.[107]

6.2 $Li_4MnGe_2S_7$

Considering the very promising results of the anode material $Li_4MnSn_2Se_7$, it was decided that other similar combinations of the lithium chalcogenidometalate network should be examined as an anode material. The substitution of selenium would remove the toxic aspect of the $Li_4MnSn_2Se_7$ compound, and substituting with lighter elements would increase the theoretical capacity according to Faraday's law (equation 6.1).

$$Q = \frac{m}{M/z\mathrm{F}} \tag{6.1}$$

Faraday's law describes the relation between the electric charge (Q) and the mass deposited on an electrode (m) when knowing the molar mass of the material (M) and the number of electrons exchanged (z). F is the the Faraday constant, 96485 C/mol.[6, 50] Using equation 6.1 an indication of the theoretical charge can be calculated with a new combination of quaternary chalcogenidometalates. Using lighter elements such as germanium and sulphur instead of tin and selenium, a lower molar mass is obtained. Assuming that the same amount of lithium-ions is inserted means that the deposited mass and electrons exchanged (z) remain constant. Leaving all parameters constant except the reduced molar mass would result in a higher electric charge and thus a higher theoretical capacity of the material.

The second synthesised lithium chalcogenidometalate network was $Li_4MnGe_2S_7$ where germanium substituted tin and sulphur substituted selenium (both substitutes found one period higher in the periodic system), thus reducing the molar mass of the compound from 872.8 g/mol to 452.4 g/mol. Substituting Se with Ge made the preparation of the slurry and following electrode less complicated as the preparation could be performed outside the glove box in normal atmosphere. The $Li_4MnSn_2Se_7$ substance was significantly more toxic and the substance relatively air sensitive. Preparation of $Li_4MnGe_2S_7$ however, enabled the pressing of the electrodes as described in chapter 3.3.1. Figure 6.9 shows a SEM image of a pressed $Li_4MnGe_2S_7$ electrode. Corresponding EDS analysis confirmed the composition of the different sized particles

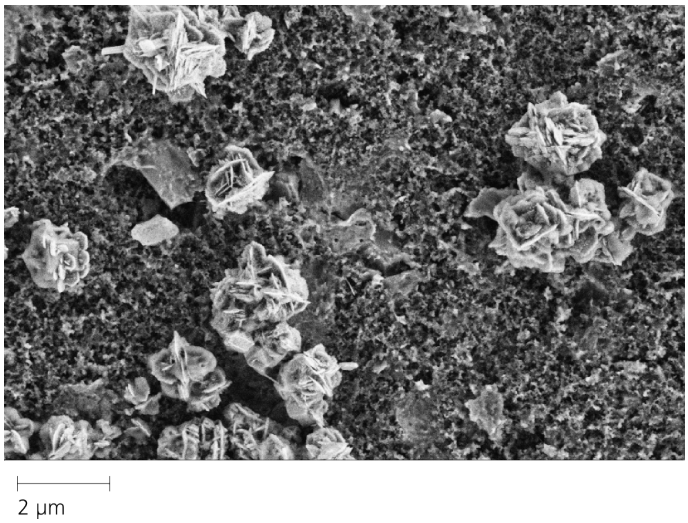

Figure 6.9: Scanning electron microscopy image of an $Li_4MnGe_2S_7$ electrode.

as for $Li_4MnSn_2Se_7$. The larger μm-scale particles consisted of $Li_4MnGe_2S_7$ and the finer nm-particles were carbon black. The EDS analysis could also exclude the presence of any major impurity traces as only the wanted elements appeared in the spectrum. Scanning electron microscopy was also performed on a non-pressed electrode where the larger particles have a more plate or disk-like form. It could be seen that their structure changed with pressing at 87 kN/cm^2, mainly through the agglomeration of the particles.

A cyclic voltammogram of a $Li_4MnGe_2S_7$ electrode can be seen in figure 6.10(a) and can be directly compared to that of $Li_4MnSn_2Se_7$ as seen in figure 6.10(b).

The sample of $Li_4MnGe_2S_7$ coated on Cu-foil has been cycled three times between 3.00 V and 0.01 V with a sweep rate of 0.1 mV/s, and it can be seen that the CV is not as stable as for $Li_4MnSn_2Se_7$ (figure 6.4). Several peaks are found, indicating a step-wise insertion of lithium-ions. At the same time, it can be seen that some of the peaks occur only in the first cycle. For example, the main oxidation in the first cycle at 1.9 V and 2.4 V in figure 6.10(a) show only indications of peaks in the following cycles. These disappearing peaks are a result of either irreversible reactions from strong structure changes upon charge/discharge or a result of the reduced capacity of the material. A decreasing capacity in the first cycles would also result in a smaller area under the CV-curve, as can be seen when comparing the reduced area under the curve for cycle one, two and three.

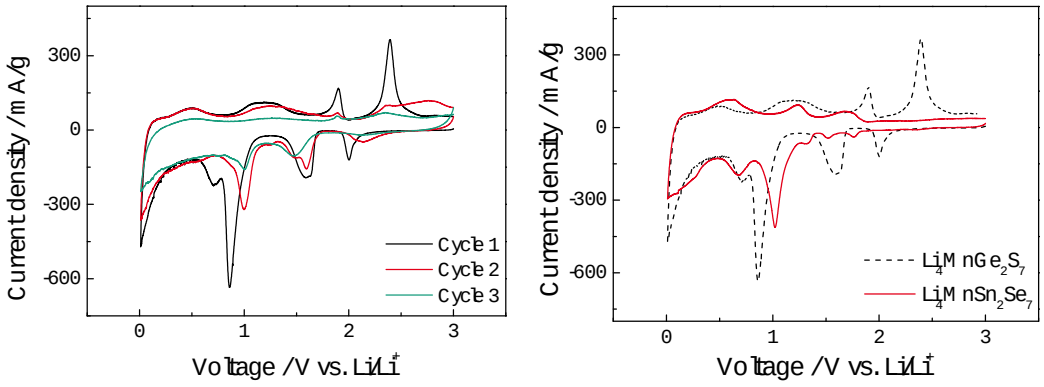

Figure 6.10: Cyclic voltammograms of $Li_4MnGe_2S_7$. a) three CV cycles of $Li_4MnGe_2S_7$ with a scan rate of 0.1 mV/s b) comparison of the first cycle of $Li_4MnGe_2S_7$ and $Li_4MnSn_2Se_7$.

A direct comparison with the first CV curve of $Li_4MnSn_2Se_7$ gives rise to several differences. The $Li_4MnGe_2S_7$ material has more peaks, although they appear to be irreversible, giving the second cycle of $Li_4MnGe_2S_7$ a better resemblance to $Li_4MnSn_2Se_7$. The $Li_4MnGe_2S_7$ material seems to undergo several structure changes in the first cycle, whereas the following cycles show a greater analogy to $Li_4MnSn_2Se_7$. In general it can be said that the $Li_4MnGe_2S_7$ material appears more unstable from the CV analysis, and a quantitative analysis of the material was performed with galvanostatic measurements as seen in figures 6.11 and 6.12.

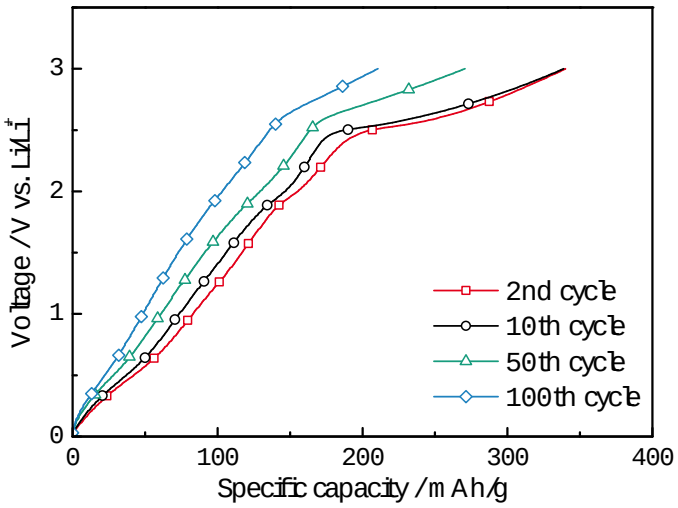

Figure 6.11: Voltage profiles with constant current cycling (current density 100 mA/g) of $Li_4MnGe_2S_7$.

The $Li_4MnGe_2S_7$ sample was cycled in the same potential window as for the cyclic voltammogram with a constant current of 100 mA/g for 100 cycles. The voltage profiles (figure 6.11) illustrate the materials specific capacity and the stability over the 100 cycles. Both the second and the tenth cycle give a specific capacity of about 340 mAh/g. As for the $Li_4MnSn_2Se_7$, this specific capacity is calculated on the basis of the entire electrode mass, as the electrode consists of more carbon black than normal for commercial electrodes, and the contribution of carbon black on the capacity will vary. The specific capacity has decreased to 270 mAh/g by the 50th cycle, and 210 mAh/g after 100 cycles. About 60 % of the specific capacity remains after 100 cycles compared to that achieved in the second cycle. As discussed above, the first cycle contains several irreversible reactions, where the CV curve of the first cycle is strongly different to that of the following cycles. It can be understood that these reactions are completed by the second cycle as the following specific capacities are stable for the first 10 cycles.

Theoretically the $Li_4MnGe_2S_7$ material should deliver a higher specific capacity than $Li_4MnSn_2Se_7$ due to the substitution of the lighter elements as calculated by Faraday's law in equation 6.1, if the reactions are analogous. To compare the specific capacity to $Li_4MnSn_2Se_7$, the cyclic behaviour of both materials is illustrated in figure 6.12.

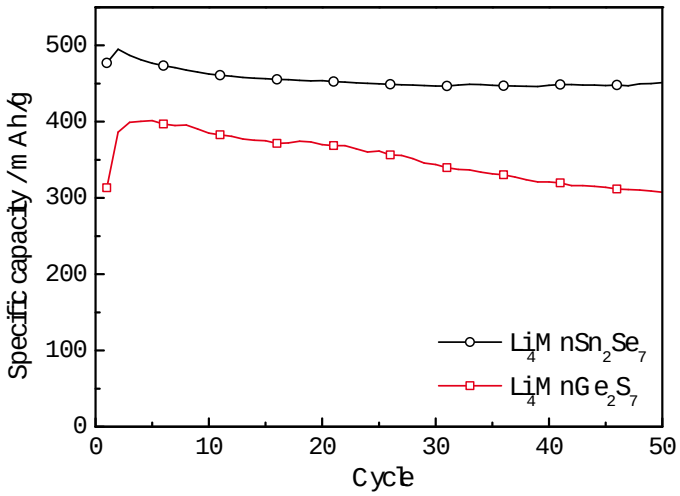

Figure 6.12: Comparison of the cyclic behaviour of $Li_4MnSn_2Se_7$ and $Li_4MnGe_2S_7$.

The cyclic behaviour of $Li_4MnSn_2Se_7$ and $Li_4MnGe_2S_7$ measured with a current density of 100 mA/g proves that the $Li_4MnSn_2Se_7$ material still provides the higher specific capacity of over 400 mAh/g. The $Li_4MnGe_2S_7$ material reaches a maximum capacity of 400 mAh/g by the fifth cycle, although it can be seen that the capacity is fading and the capacity retention of $Li_4MnGe_2S_7$ is lower than that for $Li_4MnSn_2Se_7$. After 50 cycles the specific capacity is reduced to just above 300 mAh/g, thus retaining only 75 % of the maximal achieved capacity. Despite the theoretical advantage of the $Li_4MnGe_2S_7$ material, electrochemical experiments proved that the material still achieved a lower capacity and cycle stability than the excellent $Li_4MnSn_2Se_7$ material. Preliminary simulation of the $Li_4MnGe_2S_7$ material (as performed on the $Li_4MnSn_2Se_7$ material) was performed at Fraunhofer IWM and large structure changes could be predicted, partially confirmed by the CV analysis, and a larger volume change upon charging was seen with the DFT simulation. These factors could explain the discrepancy between the assumed theoretical value of specific capacity and the obtained value.

In general the anodic properties of $Li_4MnGe_2S_7$ were shown by the electrochemical measurements, and although the specific capacity of $Li_4MnGe_2S_7$ did not quite meet the expectations or that achieved with $Li_4MnSn_2Se_7$, the material shows reversible insertion of lithium-ions and a specific capacity of over 300 mAh/g. Compared to the practical value with graphite as an anode, this capacity value is acceptable, thus confirming the prospect of the quaternary chalcogenidometalate group. Further work will examine other substitutions of Sn and Se as seen with $Li_4MnGe_2S_7$.

6.3 Summary and discussion

In this chapter a new class of anode materials for lithium-ion batteries has been characterised. This work focused on the electrochemical characterisation, such as cyclovoltammograms and galvanostatic measurements, as the main structural characterisation and the synthesis of the work is described in the PhD thesis of the project partner T. Kaib, Philipps-Universität Marburg[117].

Both $Li_4MnSn_2Se_7$ and $Li_4MnGe_2S_7$ have been examined, and the purity of the materials was confirmed via EDS (figure 6.2(b)), in addition, a crystalline structure could be confirmed with XRD analysis (figure 6.3). However, a complete confirmation of the compound via XRD was not possible, as the compound still has no occurrences in literature. The cyclic voltammogram showed a step-wise insertion of lithium-ions and a relatively high electrochemical activity for both materials. Simulations from Fraunhofer IWM suggested that 10-24 Li^+ was inserted upon charging, with a maximum of 47 % volume change with full lithium insertion. The outstanding specific capacity of $Li_4MnSn_2Se_7$ with over 400 mAh/g after 50 cycles and the coulombic efficiency were seen with the galvanostatic measurements (figure 6.6), as well as the good rate capability of the $Li_4MnSn_2Se_7$ material seen in figure 6.7.

However, the toxic aspect of Se in the $Li_4MnSn_2Se_7$ compound makes this material less commercially attractive, and the $Li_4MnGe_2S_7$ was synthesised as an alternative, also promising a higher theoretical capacity due to the use of lighter substitution elements. The second synthesised material of the lithium insertion quaternary chalcogenidometalates, $Li_4MnGe_2S_7$, proved to be electrochemically active, also with a step-wise insertion of Li^+, however, the specific capacity proved to be less than expected with about 300 mAh/g after 50 cycles. It should be noted that the specific capacities reported in this chapter are based on the entire electrode mass. The mass of carbon black was in this case not subtracted, as done for publications etc., as the electrode contained more carbon black than commercial electrodes. However, using this specific capacity on the basis of only active material would significantly improve the value and stress the advantage versus state-of-the-art anodes such as graphite. Figure C.5 in Appendix C illustrates the increased capacities of $Li_4MnSn_2Se_7$ and $Li_4MnGe_2S_7$ without the mass of carbon black.

The lithium quaternary chalcogenidometalate group has proven to be a very interesting material group for lithium-ion battery anodes and further work will continue the characterisation of these materials. The material combines wanted properties such as high capacity with great stability, thus overcoming the greatest challenge for anode materials as described in chapter 2.3. The commercially used graphite is very stable, however, with a lower capacity than the promising new anode composites containing both carbon and Sn or Si which so far have shown a very low cyclability. However, the amount of material produced for this thesis was often an issue, thus the ability for up-scaling of the synthesis will have to be examined as this is an important criteria for a potential commercialisation. Further work on this topic would also include the optimisation of particle size as well as the composition of the slurry. Due to initial material shortage, a slurry with a lower amount of active material was produced, thus, more work remains in finding the optimum composition without reducing the electronic conductivity. Other substitutions within the quaternary chalcogenidometalate network are also meant to be characterised and understood.

Chapter 7

Conclusions and outlook

This doctoral thesis presents work on new, alternative and improved electrode materials for lithium-ion batteries. It focuses on the synthesis of some materials, although mainly on the cell preparation with the use of various current collectors and electrochemical characterisation thereof. In the scope of the KoLiWIn project both cathode and anode materials, such as $LiMn_2O_4$, tin composites and $Li_4MnSn_2Se_7$ were examined as possible electrode candidates and compared with todayâĂŹs commercially used electrodes.

7.1 Conclusions

Commercially produced lithium-ion batteries mostly contain the cathode material, $LiCoO_2$, a highly dominant cathode material due to convenience, ease of preparation and a relatively high operating voltage. However, this material is very toxic and expensive due to limited availability of $LiCoO_2$, which leaves room for improvement. The spinel material $LiMn_2O_4$ possesses advantages such as an abundant material source, less toxicity and a higher specific capacity than $LiCoO_2$. In addition, the cathode material was to be coated onto a porous current collector which could improve the contacting of the material, the availability to the electrolyte, the loading of cathode material as well as several electrochemical features such as rate capability. The chosen cathode material, $LiMn_2O_4$, was synthesised with a sol-gel technique, and the right stoichiometry was easily controlled by varying the parameters of the precursors solution. The precursor solution was characterised with thermogravimetrical analysis, hence a prediction of the spinel formation with the concluding

thermal treatment was performed. As the cathode material was to be coated on a porous metal foam as a current collector, a selection of commercially available foams was made, based on availability, electrochemical stability within the wanted potential range, homogeneous surface and the thermal oxidation properties. Finally a pure nickel foam from the company Inco was chosen, and a standard thermal treatment (600 °C for 85 minutes) was optimised to ensure a porous nickel oxide surface that supplied good adhesion to the cathode material. The cathode coated on the foam substrate via dip-coating was further analysed via electron microscopy and XRD analysis. A confirmation of the obtained $LiMn_2O_4$ spinel was found when examining the $LiMn_2O_4$ powder alone, a confirmation could not be made with the $LiMn_2O_4$ coated on the nickel foam as the nickel substrate was too dominating for the XRD analysis. Cross section analysis in SEM and TEM verified the excellent adhesion between the applied NiO-layer and the coated $LiMn_2O_4$ cathode. However, an unexpected porous transition between the nickel bulk and the nickel oxide was observed. Several methods were investigated to avoid the presence of this porous transition, although it proved to be difficult. Ultimately, the observed pores were explained with the Kirkendall effect and originated from a slow self-diffusion of the components.

Electrochemical measurements were performed with the $LiMn_2O_4$ coated nickel foams, and the cyclic voltammogram confirmed the expected step-wise insertion of lithium. Galvanostatic measurements gave an initial specific capacity of 80 mAh/g, although the theoretical capacity of $LiMn_2O_4$ is 148 mAh/g. It was known that NiO could contribute as an anode material, thus a confirmation was needed to verify any unwanted side reactions of the intermediate layer of NiO in the cyclic voltammogram. However, in the cathode potential range, no side reactions of the NiO were found. To further characterise the synthesised $LiMn_2O_4$ cathode, it was additionally coated on a standard current collector, an aluminum foil. For the $LiMn_2O_4$ coated on aluminum, a specific capacity of 145 mAh/g was observed and the cathode had a higher cycle retention, obtaining a coulombic efficiency of 99.5 % after several cycles. The results of $LiMn_2O_4$ on Al-foil confirmed the excellent properties of the synthesised material with a substantial improvement in comparison with the commercially used cathode $LiCoO_2$. The disagreement with $LiMn_2O_4$ on the two current collectors was discussed, and other coating methods were also examined to investigate potential improvements. However, the most possible reason was found to be the unwanted porous

transition between the nickel bulk and the nickel oxide layer. The pores contributed to an increased internal resistance and a reduced electrical contact, thus reducing the cyclability of the material.

Graphite has long been a commercialised anode material providing first and foremost stable and safe electrodes. However, with the discovery of alloying anodes, the possibilities of improving the anode properties have been presented. This thesis shows that using Sn-containing anodes could double the theoretical capacity, however, several challenges using Sn-alloys have to be overcome in order to obtain an acceptable stability. Upon lithium insertion the tin material will expand by up to 300 %, thus several approaches have been made to suppress or to control this large structural change upon cycling.
Several Sn-containing anodes were synthesised and the initial characterisation was performed on CVD-deposited SnO_2 nanowire samples. Electron microscopy illustrated very fine wires with an inhomogeneous nanowire growth. The following electrochemical measurements displayed the collapse of this fine structure due to the large volume expansion that takes place with Sn upon lithiation. Via cyclic voltammetry, the transition from SnO_2 to Sn was observed with an irreversible peak, and the galvanostatic measurements showed a very unstable system. Three new concepts were developed to overcome the stability issue. A double CVD step produced a brush-like nanowire structure, meant to increase the surface area of the sample and thus, increasing the overall capacity. Other samples underwent a surface reduction with Ar^+-plasma, resulting in an inhomogeneous surface with both Sn, SnO and SnO_2 that were also meant to increase the capacity. Nonetheless, a better concept was shown with a core-shell structure of a carbon coated SnO_2 that improved the materials stability and the electric conductivity. Common for all the SnO_2 samples was the initial capacity loss, where usually only 30 % of the initial capacity remained after the first ten cycles, and the large disagreement with the theoretical capacity. The improved carbon-coated SnO_2 samples obtained only 60 mAh/g after the initial loss, which indicated a complete material collapse upon cycling. Ex-situ electron microscope analysis was performed to better understand the volume changes upon lithiation of Sn, and a complete structure change was observed within one cycle. The 3-dimensional network of fine nanowires transformed into a 2-dimensional surface where the nanowires had expanded and grown together, thus resulting in longer

diffusion paths and separation from the foil current collector. Depositing the SnO_2 on porous nickel foam (as used for the $LiMn_2O_4$ cathode) increased the specific capacity to about 300 mAh/g due to the better adhesion to the Ni/NiO foam and the contribution from NiO as an anode active material.

A new concept of a Sn-composite via the electrospinning method was developed to further improve the anode. A matrix of carbon nanofibers (CNF) was integrated to support the massive volume change upon cycling. The carbon nanofibers were decorated with particles of pure Sn. This composite structure proved the most successful. The cyclic voltammogram showed fewer irreversible redox processes, as the reduction of SnO_2 to Sn no longer took place, and a specific capacity of 380 mAh/g was obtained with an optimised Sn content of 60 wt%. Through parameter tuning, both loading, morphology and Sn content could be varied. Several improvements were characterised and ultimately reproducible, stable Sn-CNF samples with a high rate capability were obtained. It should also be noted that the specific capacities displayed in the chapter of the Sn-containing anodes are not directly comparable to those found in literature. The specific capacity was based on the mass of the entire electrode including the supporting matrix nanofibers consisting of a mixed carbon phase. A separate study was done to find the contribution of the CNF alone, and it was decided that the contribution was substantial enough to not be excluded from the specific capacity calculations.

The third main topic in this thesis covered the electrochemical characterisation of a novel anode group, lithium chalcogenidometalate networks. In the scope of the KoLiWIn project these new materials were quickly recognised as promising anode materials. With their large lithium insertion capability, stability upon cycling and capacities outperforming that of graphite, the materials needed to be further examined. Lithium inserting substances such as $Li_4MnSn_2Se_7$ and $Li_4MnGe_2S_7$ were synthesised and electrochemical measurements were performed and compared with simulations of the lithium insertion. From the cyclic voltammogram a step-wise lithium insertion of both $Li_4MnSn_2Se_7$ and $Li_4MnGe_2S_7$ was shown and later simulations suggested that 10-24 Li^+ were inserted upon charging. The $Li_4MnSn_2Se_7$ material obtained a very stable capacity of over 400 mAh/g, and an excellent rate capability was observed. Due to toxic aspects of the selenium in $Li_4MnSn_2Se_7$, a related material,

$Li_4MnGe_2S_7$, was produced. Having a lighter unit cell mass, it should theoretically obtain even higher capacities, although an improvement to $Li_4MnSn_2Se_7$ was not seen. The disagreement was explained with a higher structure change upon cycling as observed with the lithium insertion simulation. Both materials proved to be very interesting anode alternatives and in this chapter the specific capacities are calculated on the basis of the entire electrode, as substantial amounts of carbon black was added. Subtracting the carbon black would increase the specific capacities of both materials to over 600 mAh/g, and the obtained values would be very advantageous in comparison with the state-of-art anode material, graphite.

7.2 Outlook

One of the challenges with the $LiMn_2O_4$ cathode was the combination with the porous foam substrate. The material itself proved excellent qualities, but in combination with the nickel foam a large disagreement with the theoretical capacity was observed. It would be interesting to examine the use of other foams, although initial work with an aluminum foam proved an inferior adhesion to the cathode material. Other options include the utilisation of a nickel foam, although without the nickel oxide formed by thermal oxidation. It was proven that the NiO layer increased the adhesion to the cathode material, however, if such an adhesion could be obtained by a mechanical or chemical treatment of the pure nickel foam, the NiO could be excluded and the problem with the porous transition would be avoided. Some possibilities include chemical etching of a surface modification treatment with air plasma. The Ni/NiO foam was seen to perform better with the SnO_2 anode material, both due to improved adhesion and the double anode effect.

The use of nickel foam as a current collector should be further characterised on the anode side. A thorough electron microscope analysis of the cross section of the three phases (Ni-NiO-SnO_2) was planned, although delay with some apparatus and the limited time frame left this topic unexamined. However, such an analysis could examine the adhesion between NiO and SnO_2, as well as the porous transition between nickel and nickel oxide. Other concepts of Sn-composite anodes would also be interesting for further work. For an even better support of the volume expansion, it is suggested that the tin particles lie within the fibers, to fully utilise the stabilising

effect of the carbon matrix. Other possibilities include the combination of both silicon and tin as insertion anode materials, with a robust framework structure to support the large expansions. The use of Si would significantly increase the theoretical capacity, as long as the stability issue is resolved.

To further understand the novel lithium chalcogenidometalate networks, several investigations are necessary. An analysis of the individual peaks seen in the cyclic voltammogram could determine the reactions taking place. This was partially done via ex-situ XRD, although the material transforms from crystalline to amorphous within one cycle, and the following XRD analysis proved difficult. Other methods, such as in-situ methods, to investigate the redox processes would be interesting. Also, new combinations of the chalcogenidometalate networks are to be synthesised, where other elements will substitute the germanium, tin, sulphur or selenium. The characterisation of these new materials might investigate the possibilities and limits of this novel anode group.

List of Figures

List of Tables

List of abbreviations and symbols

at%	atomic percent
BMBF	Bundesministerium für Bildung und Forschung
CE	Coulombic efficiency / %
CNF	Carbon nanofiber
C-rate	Theoretical amount of charge which can be extracted from a given material within one hour
CSP	Cross section polisher
CV	Cyclic voltammogram
CVD	Chemical vapour deposition
DC	Direct current
DEC	Diethyl carbonate
DMC	Dimethyl carbonate
DTA	Differential thermal analysis
EC	Ethylene carbonate
EDS	Energy dispersive X-ray spectroscopy
EMC	Ethylen methyl carbonate
EPD	Electrophoretic deposition
F	Faraday constant
FIB	Focused-ion beam
ICP-OES	Inductively coupled plasma optical emission spectroscopy
IR	Ohmic loss
KoLiWIn	Konzeptstudien für neuartige Lithium-Ionen Zellen auf Basis von Werkstoff-Innovationen
LIB	Lithium-ion battery
$LiMO_2$	Lithium metal oxide
LTO	Lithium titanate, $Li_4Ti_5O_{12}$
m	Mass / g
M	Molar mass / g/mol
MCMB	Mesocarbon microbeads
ν	Potential sweep rate
NMP	N-methyl-2-pyrrolidone
OCV	Open circuit voltage

PC	Propylene carbonate
PE	Polyethylene
PP	Polypropylene
PVDF	Polyvinylidene fluoride
Q	Electric charge / C
rpm	Rate per minute
SE	Secondary electrons
SEI	Solid electrolyte interphase
SEM	Scanning electron microscopy
STEM	Scanning transmission microscopy
TEM	Transmission electron microscopy
TG	Thermal gravimetric analysis
wt%	weight percent
XRD	X-ray diffraction
z	Valency number of ions

Appendix A

Chemicals

Table A describes the chemicals and other substances (listed alphabetical) used in this thesis with batch number (or product number) and manufacturer.

Name	Material	Product/Batch no.	Manufacturer
2-(2-Methoxyethoxy)acetic acid	$C_5H_{10}O_4$	407011	Sigma-Aldrich
Aluminum foil	Al	LS377076 SDS	Goodfellow
Celgard 2325	PP/PE/PP	700068	Celgard
Copper foil	Cu	E-Cu-LTA HM72	Schlenk
Nickel foam	Ni	7440-02-0	Inco
EC	Ethylene carbonate	E26258	Sigma-Aldrich
EMC	Ethyl methyl carbonate	K4050422-012	Merck
Iodine	I_2	57659	Fluka
Lithium acetylacetonate	$C_5H_7LiO_2$	413046	Sigma-Aldrich
Lithium perchlorate	$LiClO_4$	44226	Alfa Aesar
Manganese(II) acetate tetrahydrate	$C_4H_6MnO_4{\cdot}4H_2O$	S42177-237	Sigma-Aldrich
NMP	N-methyl pyrrolidone	L03595	Alfa Aesar
PVDF	polyvinylidene fluoride	182702	Sigma-Aldrich
Super P	Carbon black	3877	Timcal

Appendix B

Hardware and software

The following tables list the apparatus and the belonging software (listed alphabetically) used in this thesis. Standard parameters or conditions are stated.

Battery Tester	
Name	Maccor 4000
Manufacturer	Maccor
Software	MimsClient
Parameters	100 mA/g as 1 C when not other stated

Doctor blade	
Name	Erichsen Coatmaster 510
Manufacturer	Erichsen
Parameters	Wet thickness: 100 μm coating speed: 25 cm/min Substrate size: 10 x 30 cm^2

Gauge Sensor	
Name	Keyence CMOS gauge sensor
Manufacturer	Keyence

Glove box	
Name	MBraun MB 20
Manufacturer	MBraun
Parameters	O_2 and H_2O < 1 ppm, Ar atmosphere

Glove box vacuum oven

Name	Eurotherm 2408
Manufacturer	Carbolite
Parameters	Heating rate: 5 K/min
	Standard heating program for electrodes: 5 h, 80 °C

ICP-OES

Name	Vista-PRO Simultaneous ICP-OES
Manufacturer	Vista
Parameters	Ar plasma source, temperature: 6000-10 000 °C
	Samples diluted with water and hydrochloric acid

Planetary Micro Mill

Name	Fritsch Pulverisette
Manufacturer	Fritsch
Parameters	300 rpm, 4x15 minutes

Potentiostat

Name	multi-channel Solartron 1400
Manufacturer	Solartron
Software	CView, ZView
Parameters	Potential window dependent of material
	sweep rate :0.1 mV/s when not other stated

Power supply for electrophoretic deposition

Name	Heinzinger TG
Manufacturer	Heinzinger
Parameters	100 V, 15 minutes

Rotating evaporator with vacuum system

Manufacturer	Büchi ROTAVAPOR R-134V
Parameters	60 minutes at 400-300 mbar
	60 minutes at 40-30 mbar

Scanning electron microscope	
Name	Supra Zeiss 25
Manufacturer	Zeiss
Parameters	InLens and SE2-detector used
	Vacuum 10^{-4}

TG/DTA	
Name	Netzsch STA 409 C Jupiter
Manufacturer	Netzsch
Parameters	R.T. to 1000 °C
	Heating rate: 10 K/min

Transmission electron microscope	
Name	JEOL JEM 2011
Manufacturer	JEOL
Parameters	200 kV
	Equipped with STEM and EDS

X-ray diffractometer	
Name	Philips PW 1710
Manufacturer	Philips
Parameters	Cu-ray
	10-80° with scan rate 0.02°/min

Appendix C

Extended results

Some results described in the main chapters (chapters 5 and 6) are based on other outcomes that are not discussed thoroughly in the result chapters. They are displayed and discussed in the appendix, and the result chapters refer to the graphs and figures shown in this section.

Tin-containing anodes

In chapter 5.1.2, the anode properties of pure NiO are described. NiO is electrochemically active and can supply a capacity between 700-400 mAh/g. Figure 5.11(b) shows a cyclovoltammogram of the SnO_2 coated on Ni/NiO foam, and it is said that the CV characteristics resemble pure NiO. Figure C.1 displays a cyclic voltammogram of a thermally treated nickel foam (with obtained NiO layer) without the SnO_2 deposition.

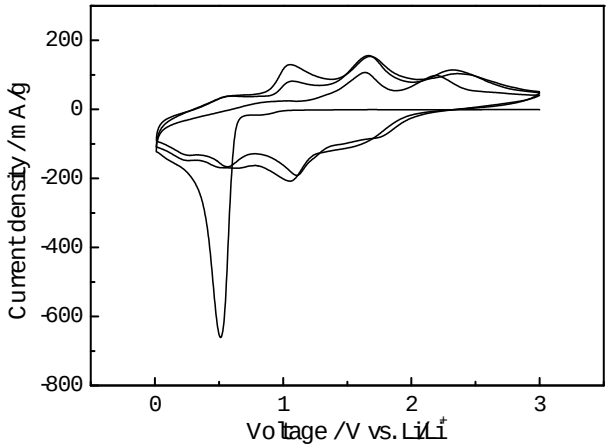

Figure C.1: Cyclic voltammetry of a thermally treated nickel foam that obtained a NiO-layer.

A reduction peak is seen in the first cycle at 0.5 V which can be attributed to the formation of the SEI-layer. The remaining peaks correspond with literature

reviews[49, 82, 83] and represent the lithiation of nickel oxide as described with equation 5.1 in chapter 5.1.2. Compared to the CV in figure 5.11(b), little difference is observed, thus the electrochemical activity seen in figure 5.11(b) originates mainly from the NiO layer. This is also explained with the ratio of the active masses. As the NiO:SnO_2 ratio is close to 2:1, a higher contribution of NiO is expected in the cyclic voltammetry.

The improved Sn-containing anodes, with the carbon nanofiber matrix, were described in chapter 5.2. As the electrospinning method produces self-supporting electrode fibers, an additional current collector is needed. Two methods of attaching a copper current collector were described. One option was to use a sputtering technique to apply a layer of Cu on one side of the electrode. Figure C.2 illustrates the Sn-CNF sample with Cu-deposition as a current collector. The coating can be seen to completely cover the carbon nanofibers and the electrochemical outcome of this current collector is seen in figure 5.16(b).

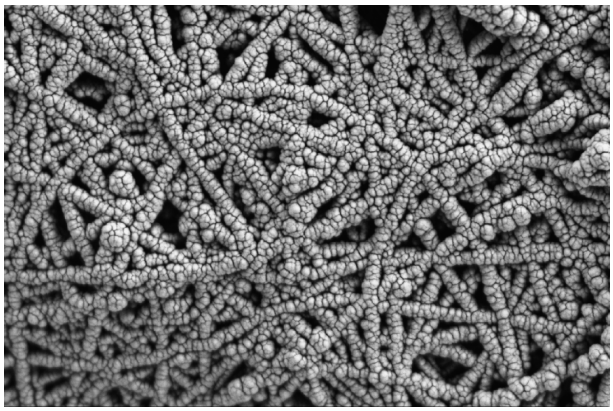

Figure C.2: Scanning electron microscope image of Sn-CNF with copper sputtering.

An optimised Sn-CNF sample consisted of 60 % Sn and 40 % of the carbon nanofibers. In order to quantify the contribution of the relatively significant amount of CNF, pure carbon nanofibers were synthesised and characterised (figure 5.20) A capacity of about 80 mAh/g after stabilisation is observed, which amounts to about 25 % of the overall capacity from Sn-CNF. A cyclovoltammogram of the pure CNF was briefly described in chapter 5.2 and can be seen in figure C.3.

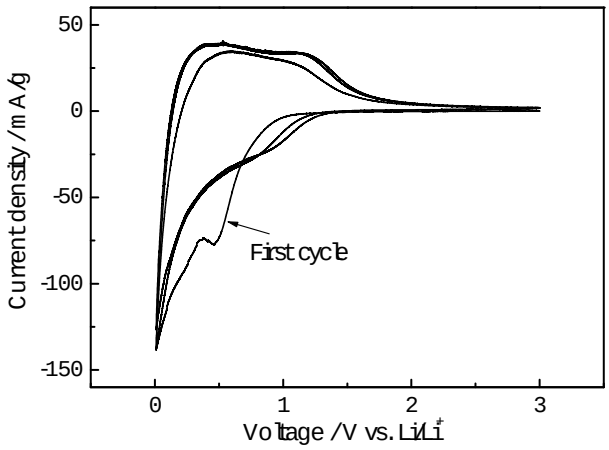

Figure C.3: Cyclic voltammetry of a pure carbon nanofibers without tin particles.

The cyclic voltammogram display a typical carbon-containing anode, with an irreversible peak at 0.5 V due to SEI-formation in the first cycle. The more important measurement is the quantification of the capacity of the pure carbon nanofibers as seen in figure 5.20.

Lithium chalcogenidometalates

Chapter 6 displayed the characterisation of the novel anode group, lithium chalcogenidometalates. Powder-form of the two materials, $Li_4MnSn_2Se_7$ and $Li_4MnGe_2S_7$ were mixed with carbon black, binder and a solvent as described in chapter 3.1. Due to material shortage, only small amounts of $Li_4MnSn_2Se_7$ or $Li_4MnGe_2S_7$ were mixed with a relatively large amount of carbon black. In order to understand the significance and contribution of carbon black alone, the cyclic voltammogram of $Li_4MnSn_2Se_7$ was compared with one of pure carbon black (figure 6.5). It could be seen that some peaks in the cyclic voltammogram originate from the carbon black in the electrode mixture. To further quantify the contribution of pure carbon black, galvanostatic measurements of the material were performed and the cyclic behaviour of pure carbon black can be seen in figure C.4.

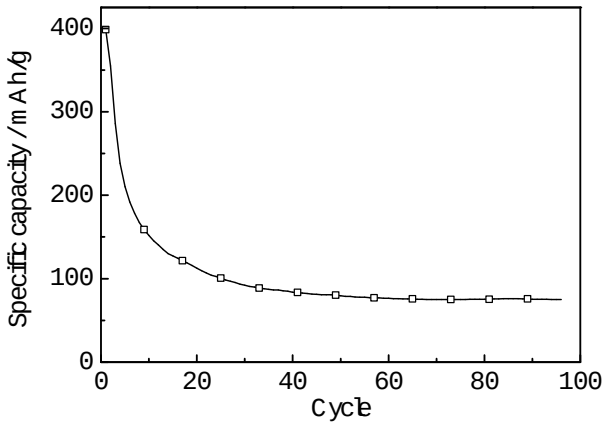

Figure C.4: Cyclic behaviour of pure carbon black.

The pure carbon black sample obtains an initial capacity of 400 mAh/g, however, after about 20 cycles the value has dropped to about 75 mAh/g. This quantification displays the relatively small contribution of pure carbon black and can be compared with the cyclic behaviour of $Li_4MnSn_2Se_7$ in figure 6.6. With $Li_4MnSn_2Se_7$ obtaining a capacity of 400 mAh/g, carbon black contributes approximately 20 % of the overall capacity. The capacity of $Li_4MnSn_2Se_7$ and $Li_4MnGe_2S_7$ calculated without the mass of carbon black can be seen in figure C.5.

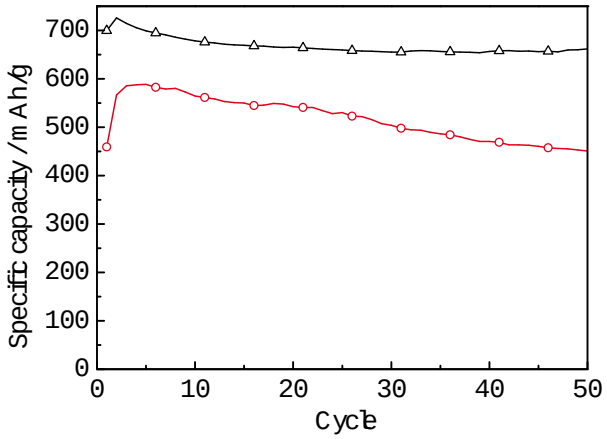

Figure C.5: Cyclic behaviour of $Li_4MnSn_2Se_7$ and $Li_4MnGe_2S_7$ when the active mass of carbon black is subtracted.

As mentioned in chapter 6, official publications of such anode materials would calculate the specific capacity based only on the one active material, not depending on the amount of carbon black in the mixture. Figure C.5 illustrates the great improvement of the specific capacities of $Li_4MnSn_2Se_7$ and $Li_4MnGe_2S_7$ compared with figure 6.12.

Curriculum Vitae

Personal information

Name	Hanne Flåten Andersen
Born	23. february 1984
Place of birth	Tønsberg, Norway
Nationality	Norwegian
Email	hannefa@gmail.com

Education

2009-2012	Fraunhofer-Institut für Silicatforschung, Würzburg PhD-thesis: New Materials for Lithium-Ion Batteries
2004-2009	Norges teknisk-naturvitenskapelige universitet (NTNU), Trondheim, Chemical Engineering Specialization: Materials chemistry and energy technology
2007-2008	University of Auckland (UoA), New Zealand Chemical and Materials Engineering Exchange studies 7.-8. semester
2000-2003	Horten College, general studies

Work experience

2012-	Fraunhofer-Institut für Silicatforschung, Würzburg: Research associate
2009-2012	Fraunhofer-Institut für Silicatforschung, Würzburg: PhD-student Project work/PhD-thesis: Konzeptstudien für neuartige Lithium-Ionen-Zellen auf Basis von Werkstoff-Innovationen
2005-2009	NTNU, Trondheim: Student assistant in Chemistry 1, Process engineering and Basic IT
2008	DNV, Høvik: Summer Internship 2008. Project work: The Green Cruise Experience
2007/2008	NTNU, Trondheim: Research assistant, institute for material technology, optimizing fuel cells

Publications and Posters

06.2013	Paper Advanced Functional Material, 2013 Synthesis and Characterization of New Li-Intercalating Quaternary Chalcogenidotetrelate Networks
01.2013	Kompetenznetwerk Lithium Ionen Batterien (KLIB), Berlin Lithium-Chalkogenidometallat als ein neuartiges Anodenmaterial für Lithium-Ionen-Batterien
06.2012	International Meeting on Lithium Batteries (IMLB), 2012, Jeju Island, South Korea Nanostructured Sn-Anodes for High Capacity Lithium-Ion Batteries
05.2011	European Materials Research Society (EMRS), Nice, France Quaternary lithium metallate as a new class of anode materials for lithium-ion batteries

Bibliography

[1] Fraunhofer-ISC. *Vorhabensbeschreibung Konzeptstudien für neuartige Lithium-Ionen-Zellen auf der Basis von Werkstoff-Innovationen (KoLi-WIn) für die Bekanntmachung Lithium-Ionen-Batterie LIB2015 vom 05.11. 2007*. (2008).

[2] Yoshio, M., Brodd, R. J., and Kozawa, A. *Lithium-Ion Batteries*. Springer, 1 edition, (2009).

[3] Tarascon, J. M. and Armand, M. *Nature* **414**(6861), 359–367 (2001).

[4] Ohzuku, T. and Brodd, R. J. *Journal of Power Sources* **174**(2), 449–456 (2007).

[5] Scrosati, B. and Garche, J. *Journal of Power Sources* **195**(9), 2419–2430 (2010).

[6] Daniel, C. and Besenhard, J. O. *Handbook of Battery Materials*. Wiley-VCH, 2 edition, (2011).

[7] Winter, M. and Brodd, R. J. *Chemical Reviews* **104**(3) (2004).

[8] Linden, D. and Reddy, T. B. *Handbook of Batteries*. McGraw Hill, 3 edition, (1995).

[9] Dillon, S. J. and Sun, K. *Current Opinion in Solid State and Materials Science* **16**(4) (2012).

[10] Li, H., Wang, Z., Chen, L., and Huang, X. *Advanced Materials* **21**(45), 4593–4607 (2009).

[11] Zhang, W. J. *Journal of Power Sources* **196**(1), 13–24 (2011).

[12] Ji, L., Lin, Z., Alcoutlabi, M., and Zhang, X. *Energy and Environmental Science* **4**(8), 2682–2689 (2011).

[13] Patterson, M. *Anode materials for lithium-ion batteries*. Presentation at Indiana University Battery Workshop, (2009).

[14] Sheng Dai, Xiao-Guang Sun, B. G. *Hard Carbon Materials for High-Capacity Li-ion Battery Anodes*. Presentation from Oak Ridge national Laboratory, (2011).

[15] Guo, P., Song, H., and Chen, X. *Electrochemistry Communications* **11**, 1320–1324 (2009).

[16] Deng, D., Kim, M. G., Lee, J. Y., and Cho, J. *Energy and Environmental Science* **2**(8), 818–837 (2009).

[17] Möller, K.-C. *Seminar: Batterien; Grundlagen, Funktionsweise und Anwendungen*. (2011).

[18] Winter, M. and Besenhard, J. O. *Electrochimica Acta* **45**(1), 31–50 (1999).

[19] Wang, Q., Li, H., Chen, L., and Huang, X. *Solid State Ionics* **152-153**, 43–50 (2002).

[20] Park, M., Wang, G., Kang, Y., Wexler, D., Dou, S., and Liu, H. *Angewandte Chemie International Edition* **46**(5), 750–753 (2007).

[21] Shi, S. L., Liu, Y. G., Zhang, J. Y., and Wang, T. H. *Chinese Physics B* **18**(10), 4564–4570 (2009).

[22] Kamali, A. R. and Fray, D. J. *Reviews on Advanced Materials Science* **27**(1), 14–24 (2011).

[23] Sangster, J. and Bale, C. W. *Journal of Phase Equilibria* **19**(1), 70–75 (1998).

[24] Yoshio, M., Tsumura, T., and Dimov, N. *Journal of Power Sources* **146**(1-2), 10–14 (2005).

[25] Ellis, B. L., Lee, K. T., and Nazar, L. F. *Chemistry of Materials* **22**(3), 691–714 (2010).

[26] Whittingham, M. S. *Chemical Reviews* **104**(10), 4271–4301 (2004).

[27] Wang, Y. and Cao, G. *Advanced Materials* **20**, 2251–2269 (2008).

[28] Needham, S. A., Wang, G. X., Liu, H. K., Drozd, V., and Liu, R. *Journal of Power Sources* **174**, 828–831 (2007).

[29] Liu, H., Wu, Y. P., Rahm, E., Holze, R., and Wu, H. Q. *Journal of Solid State Electrochemistry* **8**, 450–466 (2004).

[30] Fergus, J. W. *Journal of Power Sources* **195**(4), 939–954 (2010).

[31] Park, S., Okada, S., and Yamaki, J. *Journal of Novel Carbon Resource Science* **3**, 27–31 (2011).

[32] Bao, S. J., Liang, Y. Y., and Li, H. L. *Materials Letters* **59**(28), 3761–3765 (2005).

[33] Wu, Y. P., Rahm, E., and Holze, R. *Electrochimica Acta* **47**(21), 3491–3507 (2002).

[34] Yi, T. F., Zhu, Y. R., Zhu, X. D., Shu, J., Yue, C. B., and Zhou, A. N. *Ionics* **15**(6), 779–784 (2009).

[35] Martha, S., Sclar, H., Framowitz, Z., Kovacheva, D., Saliyski, N., Gofer, Y., Sharon, P., Golik, E., Markovsky, B., and Aurbach, D. *Journal of Power Sources* **189**, 248–255 (2009).

[36] Yabuuchi, N. and Ohzuk, T. *Journal of Power Sources* **119-121**(24), 171–174 (2003).

[37] Sclar, H., Kovacheva, D., Zhecheva, E., Stoyanova, R., Lavi, R., Kimmel, G., Grinblat, J., Girshevitz, O., Amalraj, F., Haik, O., Zinigrad, E., Markovsky, B., and Aurbach, D. *Journal of the Electrochemical Society* **156**(11), A938–A948 (2009).

[38] Zaghib, K., Mauger, A., Groult, H., Goodenough, J. B., and Julien, C. M. *Materials* **6**, 1028–1049 (2013).

[39] Fischer, A. *BASF - Innovative Materials for today's and future generations of batteries*. Presentation at DPG Herbstsitzung, (2011).

[40] Goodenough, J. B. and Kim, Y. *Chemistry of Materials* **22**(3), 587–603 (2010).

[41] Zhang, S. S. *Journal of Power Sources* **162**(2), 1379–1394 (2006).

[42] Röder, M. *Dünnschichtelektroden zur Charakterisierung der Grenzflächen in Lithium-Ionen-Batterien. Not published*. PhD thesis, Fraunhofer ISC - Julius-Maximilians-Universität Würzburg, (2014).

[43] Arora, P. and Zhang, Z. M. *Chemical Reviews* **104**(10), 4419–4462 (2004).

[44] Zhang, S. S. *Journal of Power Sources* **164**(1), 351–364 (2007).

[45] Myung, S. T., Hitoshi, Y., and Sun, Y. K. *Journal of Materials Chemistry* **21**(27), 9891–9911 (2011).

[46] Nam, D. H., Kim, R. H., Han, D. W., and Kwon, H. S. *Electrochimica Acta* **66**, 126–132 (2012).

[47] Li, X. F., Dhanabalan, A., Bechtold, K., and Wang, C. L. *Electrochemistry Communications* **12**(9), 1222–1225 (2010).

[48] Yang, C., Zhang, D., Zhao, Y., Lu, Y., Wang, L., and Goodenough, J. B. *Journal of Power Sources* **196**(24), 10673–10678 (2011).

[49] Yao, M., Okuno, K., Iwaki, T., Kato, M., Tanase, S., Emura, K., and Sakai, T. *Journal of Power Sources* **173**(1), 545–549 (2007).

[50] Hamann, C. H., Hamnett, A., and Vielstich, W. *Electrochemistry*. Wiley-VCH, 2 edition, (2007).

[51] Möller, K.-C. *Seminar: Grundlagen der Cyclovoltammetrie*. (2012).

[52] Bard, A. J., Inzelt, G., and Scholz, F. *Electrochemical Dictionary*. Springer Verlag, 1 edition, (2008).

[53] Bard, A. J. and Faulkner, L. R. *Electrochemical Methods - Fundamentals and Applications*. John Wiley & Sons, 1 edition, (1980).

[54] Krebs, F. C. *Solar Energy Materials and Solar Cells* **93**(4), 394–412 (2009).

[55] Besra, L. and Liu, M. *Progress in Materials Science* **52**(1), 1–61 (2007).

[56] Sarkar, P. and Nicholson, P. S. *Journal of the American Ceramic Society* **79**(8), 1987–2002 (1996).

[57] Hamagami, J., Goto, A., Kanamura, K., and Umegaki, T. *Key Engineering Materials* **181-1**, 151–154 (2000).

[58] Kanamura, K., Goto, A., Hamagami, J., and Umegaki, T. *Electrochemical and Solid-State Letters* **3**(6), 259–262 (2000).

[59] Fiz, R. *Not published*. PhD thesis, University of Cologne, (2013).

[60] von Hagen, R. *Keramik und Kompositnanofasern für die Energieanwendung: Erzeugung mittels Elektrospinnen und Anwendung als Elektrodenmaterialien in Lithium Ionen Batterien. Not published*. PhD thesis, University of Cologne, (2013).

[61] Goodhew, P. J. and Humphreys, F. J. *Elektronenmikroskopie. Grundlagen und Anwendung*. McGraw-Hill Book Company, 2 edition, (1998).

[62] Simmen, F. *Dissertation Nr. 19092*. PhD thesis, ETH Zürich, (2010).

[63] Williams, D. B. and Carter, C. B. *Transmission Electron Micropscopy, Part 1: Basics*. Springer, 2 edition, (2009).

[64] Klug, H. P. and Alexander, L. E. *X-ray diffraction procedures*. Wiley-VCH, (1954).

[65] Hemminger, W. F. and Cammenga, H. K. *Methoden der Thermischen Analyse*. Springer, 1 edition, (1989).

[66] West, A. R. *Grundlagen der Festkörperchemie*. Wiley-VCH, 1 edition, (1992).

[67] Nölte, J. *ICP Emissionsspektrometrie für Praktiker*. Wiley-VCH, 1 edition, (2002).

[68] Ul-Hamid, A. *Anti-Corrosion Methods and Materials* **51**(3), 216–222 (2004).

[69] Ul-Hamid, A. *Corrosion Science* **46**(1), 27–36 (2004).

[70] Yi, T.-F., Hao, C.-L., Yue, C.-B., Zhu, R.-S., and Shu, J. *Synthetic Metals* **159**(13), 1255–1260 (2009).

[71] Amaral, F. A., Bocchi, N., Brocenschi, R. F., Biaggio, S. R., and Rocha-Filho, R. C. *Journal of Power Sources* **195**(10), 3293–3299 (2010).

[72] Iqbal, M. J. and Zahoor, S. *Journal of Power Sources* **165**(1), 393–397 (2007).

[73] Czerwinski, F. and Szpunar, J. A. *Journal of Materials Science* **32**(22), 5463–5472 (1998).

[74] Kumari, S. V., Natarajan, M., Vaidyan, V. K., and Koshy, P. *Journal of Materials Science Letters* **11**(11), 761–762 (1992).

[75] Paritskaya, L. N., Gusak, A., Mehrer, H., Beke, D., and Philibert, J. *Defect and Diffusion Forum* **249**, 73–80 (2006).

[76] Railsback, J. G., Johnston-Peck, A. C., Wang, J., and Tracy, J. B. *ACS Nano* **4**(4), 1913–1920 (2010).

[77] Nakamura, R. and Nakajima, H. *www.intechopen.com* , DOI: 10.5772/16931 (2011).

[78] Xiong, L., Xu, Y., Tao, T., and Goodenough, J. B. *Journal of Power Sources* **199**, 214–2192 (2012).

[79] Li, X., Xu, Y., and Wang, C. *Applied Surface Science* **255**(11), 5651–5655 (2009).

[80] Fu, Z. W., Ma, J., and Qin, Q. Z. *Solid State Ionics* **176**(17-18), 1635–1640 (2005).

[81] Eftekhari, A. *Electrochimica Acta* **47**(27), 4347–4350 (2002).

[82] Li, X., Dhanabalan, A., and Wang, C. *Journal of Power Sources* **196**(22), 9625–9630 (2011).

[83] Huang, X. H., Tu, J. P., Zhang, B., Zhang, C. Q., Li, Y., Yuan, Y. F., and Wu, H. M. *Journal of Power Sources* **161**(1), 541–544 (2006).

[84] Needham, S. A., Wang, G. X., and Liu, H. K. *Journal of Power Sources* **159**(1), 254–257 (2006).

[85] Liu, H., Wang, G., Liu, J., Qiao, S., and Ahn, H. *Journal of Materials Chemistry* **21**(9), 3046–3052 (2011).

[86] Patoux, S., Daniel, L., Bourbon, C., Lignier, H., Pagano, C., Le Cras, F., Jouanneau, S., and Martinet, S. *Journal of Power Sources* **189**(1), 344–352 (2009).

[87] Arbizzani, C., Balducci, A., Mastragostino, M., Rossi, M., and Soavi, F. *Journal of Power Sources* **119**, 695–700 (2003).

[88] Singh, P., Sil, A., Nath, M., and Ray, S. *Physica B-Condensed Matter* **405**(2), 649–654 (2010).

[89] Park, B. G., Kim, S., Kim, I. D., and Park, Y. J. *Journal of Materials Science* **45**(14), 3947–3953 (2010).

[90] Thirunakaran, R., Sivashanmugam, A., Gopukumar, S., and Rajalakshmi, R. *Journal of Power Sources* **187**(2), 565–574 (2009).

[91] Ariyoshi, K. and Ohzuku, T. *Journal of Power Sources* **174**(2), 1258–1262 (2007).

[92] Wu, H. C., Lee, E., Wu, N. L., and Jow, T. R. *Journal of Power Sources* **197**, 301–304 (2012).

[93] Wu, H. C., Wu, H. C., Lee, E., and Wu, N. L. *Electrochemistry Communications* **12**(3), 488–491 (2010).

[94] Yi, T. F., Hu, X. G., Dai, C. S., and Gao, K. *Journal of Materials Science* **42**(11), 3825–3830 (2007).

[95] Kim, K. W., Kim, M. R., Lee, S. W., Han, K. S., and Woo, S. I. *Chemical Vapor Deposition* **9**(4), 187–192 (2003).

[96] Shu, D., Chung, K. Y., Cho, W. I., and Kim, K. B. *Journal of Power Sources* **114**(2), 253–263 (2003).

[97] Lee, K. L., Jung, J. Y., Lee, S. W., Moon, H. S., and Park, J. W. *Journal of Power Sources* **130**(1-2), 241–246 (2004).

[98] Raja, M. W., Mahanty, S., and Basu, R. N. *Journal of Materials Chemistry* **19**(34), 6161–6166 (2009).

[99] Gogotsi, Y. and Simon, P. *Science* **334**(6058), 917–918 (2011).

[100] Szczech, J. R. and Jin, S. *Energy and Environmental Science* **4**(1), 56–72 (2010).

[101] Choi, N. S., Yao, Y., Cui, Y., and Cho, J. *Journal of Materials Chemistry* **21**(27), 9825–9840 (2010).

[102] Mohamedi, M., Lee, S. J., Takahashi, D., Nishizawa, M., Itoh, T., and Uchida, I. *Electrochimica Acta* **46**, 1161–1168 (2001).

[103] Yang, S., Song, H., Yi, H., Liu, W., Zhang, H., and Chen, X. *Electrochimica Acta* **55**, 521–527 (2009).

[104] Ko, Y. D., Kang, J. G., Park, J. G., Lee, S., and Kim, D. W. *Nanotechnology* **20**(45) (2009).

[105] Brousse, T., Retoux, R., Herterich, U., and Schleich, D. M. *Journal of the Electrochemical Society* **145**(1), 1–4 (1998).

[106] Yao, J., Shen, X., Wang, B., Liu, H., and Wang, G. *Electrochemistry Communications* **11**(10), 1849–1852 (2009).

[107] KoLiWIn-results. *Presentations from quartely KoLiWIn project meetings*. (2011).

[108] Zhao, N. H., Wang, G. J., Huang, Y., Wang, B., Yao, B. D., and Wu, Y. P. *Chemistry of Materials* **20**(8), 2612–2614 (2008).

[109] Zhao, N. H., Yang, L. C., Zhang, P., Wang, G. J., Wang, B., Yao, B. D., and Wu, Y. P. *Materials Letters* **64**(8), 972–975 (2010).

[110] Pan, J., Ganesan, R., Shen, H., and Mathur, S. *The Journal of Physical Chemistry C* **114**(18), 8245–8250 (2010).

[111] Müller, R. *Not published*. PhD thesis, University of Cologne, (2013).

[112] von Hagen, R., Lorrmann, H., Möller, K.-C., and Mathur, S. *Advanced Energy Materials* **2**(5), 553–559 (2012).

[113] Zou, L., Gan, L., Kang, F., Wang, M., Shen, W., and Huang, Z. *Journal of Power Sources* **195**(4), 1216–1220 (2010).

[114] Yu, Y., Gu, L., Wang, C., Dhanabalan, A., and Maier, J. *Angewandte Chemie* **121**, 6607–6611 (2009).

[115] Grigoriants, I., Sominski, L., Li, H. L., Ifargan, I., Aurbach, D., and Gedanken, A. *Chemical Communications* **7**, 921–923 (2005).

[116] Wang, Y., Wu, M., Jiao, Z., and Lee, J. Y. *Chemistry of Materials* **21**(14), 3210–3215 (2009).

[117] Kaib, T. *not published*. PhD thesis, Philipps-Universität Marburg, (2013).

[118] Andersen, H. F., Möller, K.-C., Kaib, T., Kaib-Haddadpour, S., and Dehnen, S. *Patent no. 1020121061100.9*. (2012).

[119] Noel, M. and Suryanarayanan, V. *Journal of Power Sources* **111**(2), 193–209 (2002).

[120] Kasavajjula, U., Wang, C., and Appleby, A. J. *Journal of Power Sources* **163**(2), 1003–1039 (2007).

[121] Kaib, T., Haddadpour, S., Andersen, H. F., Mayrhofer, L., Järvi, T., Möller, K.-C., and Dehnen, S. *doi: 10.1002/adfm.201301025*. Advanced Functional Materials, (2013).